

Stress and damage analyses of thermal barrier coatings under cyclic thermal loading conditions

By

Jinrong Yan, B.Eng.

A thesis submitted to
the Faculty of Graduate Studies and Research
in partial fulfillment of the requirements for
the degree of Master of Applied Science

Ottawa-Carleton Institute for Mechanical and Aerospace Engineering

Department of Mechanical and Aerospace Engineering

Carleton University

Ottawa, ON, Canada

August 2022

Abstract

The premature failure of the thermal barrier coatings (TBCs) system is a preliminary phenomenon that can significantly limit their applications in gas turbine engines. The delamination of TBCs occurs typically at interfaces between the top coat and bond coat due to thermal mismatch stress via both crack nucleation and propagation and decohesion. In this thesis, this phenomenon was studied using a multi-physics approach. Under a high-temperature adverse environment, multiple factors are coupled to lead to the failure through creep, sintering of top coat, oxide growth and interface imperfection. Heat transfer was implemented into the TBC model in a cyclic manner to simulate the in-service operation of hot section components. The periodic cross-sectional model of the TBCs was modelled with the phase field damage model addressing the stress evolution and fracture-damage evolution of top coat. Results demonstrate that the model well couples the above factors, and the top coat cracks at off-peak of interfacial rumpling propagate rapidly during an early stage and stop growing as the TGO is thickened. The crack propagation results are correlative to the stress evolution during the thermal cycles, which partially proves the quality of crack propagation simulation results.

Acknowledgements

I would like to express my deepest appreciation to my thesis supervisor, Professor Xin Wang, for his guidance and support in thesis throughout the research program. Without his persistent help this thesis would not have been possible.

I would also like to express my sincerer gratitude to my co-supervisor, Dr. Kuiying Chen from National Research Council for providing the research direction, instructing the FEM simulation theories, and thesis instruction during the research program.

I am grateful for the financial support from the Natural Science and Engineering Research Council of Canada (NSERC), National Research Council (NRC) and Teaching Assistant opportunities from Carleton University.

Finally, I would like to thank my family and friends for their warm encouragement and support.

Table of Contents

Abstract	II
Acknowledgements	III
List of Tables	VII
List of Figures	VIII
List of Abbreviations	XIII
Nomenclature	XIV
1. Introduction.....	1
2. Background and Literature Review	4
2.1. Constituents of TBC system	4
2.1.1. Top-Coat (TC).....	5
2.1.2. Bond coat (BC).....	6
2.1.3. Thermally growth oxide (TGO)	7
2.2. Manufacturing methods of TBCs	7
2.2.1. Atmospheric Plasma Spray (APS)	7
2.2.2. Electron-beam physical vapor deposition (EB-PVD)	8
2.2.3. Suspension plasma spray (SPS)	9
2.3. Failure mechanisms and lifetime prediction.....	10
2.3.1. Thermal mismatch failures.....	10
2.3.2. Material degradation	13
2.3.3. Life prediction	22
2.4. Damage Model	24
2.5. Phase field damage model for brittle fracture	26
3. Stress analysis at the TC/TGO interface with multiple effects.....	45
3.1. FEM model setup, geometry, and boundary conditions.....	45

3.2.	Heat transfer model setup	46
3.3.	Material properties.....	49
3.4.	Mesh design.....	50
3.5.	Parametric study plans.....	51
3.6.	Results	51
3.6.1.	Convergence test	51
3.6.2.	Reference case.....	52
3.6.3.	Parametric study results of TGO growth rate.....	54
3.6.4.	Parametric study result of the roughness geometry aspect ratio	56
3.6.5.	Parametric study results of TC sintering.....	58
3.6.6.	Parametric study of isothermal model.....	59
3.7.	Summary.....	63
4.	Crack propagation study with Phase field damage model	91
4.1.	Verification Example.....	92
4.2.	FEM model setup, geometry, and boundary condition	92
4.3.	Material properties and mesh designs	93
4.4.	Parametric study plan	93
4.5.	Results	94
4.5.1.	Convergence test	94
4.5.2.	Crack propagation at the crack near TC off-peak	95
4.5.3.	Parametric study of roughness ratio	96
4.5.4.	Parametric study on initial crack position	97
4.6.	Summary.....	99
5.	Conclusions and Future works.....	112
5.1.	Conclusions	112

5.2. Future work.....	113
References:.....	115

List of Tables

Table 3-1. Thermal properties of Substrate, BC, TGO, and TC[8], [91]–[97].....	64
Table 3-2. Aero engine operating environment [95], [98].....	64
Table 3-3. Temperature-dependent material properties for all layers of the TBC system.	65
Table 3-4. Creep data for TC, BC, and TGO [29], [63]	66
Table 3-5. TGO growth equation inputs [58]	66
Table 3-6. Parametric study configurations and case number	66
Table 4-1. Phase field damage model properties [60]	100
Table 4-2. Parametric study configurations and case number	100

List of Figures

Figure 2-1. A schematic diagram of a TBC system on an aero-engine turbine blade made with an EB-PVD top coat [4].....	32
Figure 2-2. The cross-sectional image of APS TBC with (a) normal scale and (b) zoomed scale [80].....	32
Figure 2-3. (a) A schematic of the APS deposition process; (b) a detail view of the particle deposition to the substrate [81].....	33
Figure 2-4. The cross-sectional SEM image of the microstructure of the TBC system was deposited by the EB-PVD method[24].	33
Figure 2-5. Schematic of EB-PVD deposition process; (a): Device illustrations; (b): Deposition process [82].	34
Figure 2-6. The (a) cross-sectional and (b) top view microstructure image of SPS deposited TBC coating[83].....	34
Figure 2-7. (a) The demonstration of the compressive stress at TGO, induced by the CTE difference between TGO and BC; (b) the interface will be deformed with the compression – relaxation cycle also called the “Ratchet Effect” [5].....	35
Figure 2-8. Cross-sectional SEM images at the interface of APS TBCs denote the interfacial roughness (red dotted box) and horizontal cracks (yellow arrows) [31], [32].	35
Figure 2-9. A simplified mechanical model near the TC/TGO/BC interface is represented by a group of springs and the stress distribution. The darker color spring denotes a higher spring constant, positive and negative signs denote tensile and compressive stress, and the length of the arrow marks denotes the contraction amount; (a) the spring model without TGO (b) stress distribution at cool-down period (c) the spring model with thin TGO; (d,e) stress distribution at cool-down period with the effect of TGO [29].....	36
Figure 2-10. The spallation process of the thermal barrier coating. (I) Starting by undulating the bond-coat (BC); (II) then nucleate and propagate the cracks near the interface; (III) cracks coalesce and lead to the eventual spallation[34].....	37
Figure 2-11. (a) Schematic diagram of Domain (1): inter-splat pores, demonstrated in perspective, elevation, and plan view; (b) Schematic diagram of Domain (2): intra-splat	

microcracks, demonstrated in perspective, elevation, and plan view. The dotted line is the shape of the model when it is fully sintered [41].....	38
Figure 2-12. The thermal elasto-viscoplastic constitutive model for the sintering process [55].....	38
Figure 2-13. the sintering behavior of a periodic unit of grain in the coating. To reduce free energy, the neck's radius will grow until it reaches the edge. The microcracks around the neck will be cured.	38
Figure 2-14. Periodic finite element for SPS -TBC with a long vertical crack. [54].....	39
Figure 2-15. Comparison of FEA and experimental (TMA) results with the contribution of vertical crack (VC) [54].....	40
Figure 2-16. The macroscopic in-plane elastic modulus evolution for APS YSZ at the temperature of 1340K was simulated by the sintering model.....	41
Figure 2-17. time and temperature-dependent elastic modulus surface plot for YSZ YC sintering at 1340 K.....	42
Figure 2-18. TGO growth strain over oxidation time in the first 10 cycles. Growth pauses when it is cooled down and continues when it is fully heated.....	43
Figure 2-19. Crack topology of a bar that has a crack at $x = 0$; a) sharp crack at $x = 0$; b) diffusive crack at $x = 0$ with length scale l [77].....	43
Figure 2-20. Crack topology embedded in a solid B with a) sharp crack surface Γ and b) diffusive crack surface $\Gamma_l(d)$. The ∂B denotes the edge of the solid. [77]	44
Figure 3-1. (a) The periodic unit of a TBC system applies in FEM simulation and structural mechanics boundary conditions (b) the thermal boundary conditions.	67
Figure 3-2. The schematic of a common turbine blade with cooling functions. The internal ducts are built with ribs to improve the heat transfer coefficient [3].....	68
Figure 3-3. thermal cycle applied in the simulation (red: with heat transfer input; blue: with isothermal input).....	69
Figure 3-4. Thermal gradient along the TBC and substrate at elevated temperature	69
Figure 3-5. Interface mesh design and the zoom-in at TGO for the FEM model.....	70
Figure 3-6. Mesh element for (a) displacement field; (b) temperature field.	70
Figure 3-7. The positions of the simulation results.....	71

Figure 3-8. Convergence of maximum radial stress and first principal stress (σ_1) at TGO after the cool-down of the first cycle.	72
Figure 3-9. First principal stress (σ_1) for 30 thermal cycles at the off-peak and off-valley positions.	72
Figure 3-10. The radial stress (σ_{22}) for 30 cycles at the off-peak and off-valley positions for reference case I.	73
Figure 3-11. The in-plane stress (σ_{11}) for 30 thermal cycles at the off-peak and off-valley positions for reference case I.	73
Figure 3-12. The radial stress distribution (σ_{22}) for the reference case I at the interface at the end of cycles denotes the maximum stress at TC.	74
Figure 3-13. The first principal stress (σ_1) distribution for the reference case I at the interface at the end of cycles denotes the maximum stress at TC.	75
Figure 3-14. The first principal stress (σ_1) at off-peak position with different TGO growth rates (case I,II,III)	75
Figure 3-15. The first principal stress (σ_1) at off-valley position with different TGO growth rates (case I,II,III)	76
Figure 3-16. The radial stress (σ_{22}) at off-peak with different TGO growth rates (case I,II,III)	76
Figure 3-17. The radial stress (σ_{22}) at off-valley with different TGO growth rates (case I,II,III)	77
Figure 3-18. The radial stress distribution (σ_{22}) for the case (II): 0.5 times TGO growth, at the interface at the end of cycles denotes the maximum stress at TC.	78
Figure 3-19. The first principal stress (σ_1) for case (II): 0.5 times TGO growth, at the interface at the end of cycles denotes the maximum stress at TC.	79
Figure 3-20. The radial stress distribution (σ_{22}) for the case (III): 1.5 times TGO growth, at the interface at the end of cycles denotes the maximum stress at TC.	80
Figure 3-21. The first principal stress (σ_1) for the case (III): 1.5 times TGO growth, at the interface at the end of cycles denotes the maximum stress at TC.	81
Figure 3-22. Max of first principal stress (σ_1 -max) at TC with different TGO growth rates for case I, II, III	82

Figure 3-23. Max radial stress (σ_{22} -max) at TC with different TGO growth rates for case I, II, III.....	82
Figure 3-24. The radial stress (σ_{22}) at off-peak with different roughness aspect ratios for parametric study for case I, IV, V, VI.....	83
Figure 3-25. The first principal stress (σ_1) at off-peak with different roughness aspect ratios for parametric study of case I, IV, V, VI.	84
Figure 3-26. The radial stress (σ_{22})at off-valley with different roughness aspect ratios for parametric study of case I, IV, V, VI.....	84
Figure 3-27. The first principal stress (σ_1) at off-valley with different roughness aspect ratios for parametric study of case I, IV, V, VI.	85
Figure 3-28. The max of first principal stress (σ_1 -max) at the TC with different roughness aspect ratios for parametric study of case I, IV, V, VI.	85
Figure 3-29. The max radial stress (σ_{22} -max) at the TC with different roughness aspect ratios for parametric study of case I, IV, V, VI.	86
Figure 3-30. The radial stress (σ_{22}) at off-peak and off-valley for parametric study sintering model of case I, VII	86
Figure 3-31. The first principal stress (σ_1) at off-peak and off-valley for parametric study of case I, VII	87
Figure 3-32. The maximum radial stress (σ_{22} -max) at TC for parametric study of case I and VII.	87
Figure 3-33. The maximum of first principal stress (σ_1 -max) at TC for parametric study of case I and VII.....	88
Figure 3-34. The radial stress (σ_{22}) at off-peak and off-valley for parametric study sintering model of case I, VIII	89
Figure 3-35. The first principal stress (σ_1) at off-peak and off-valley positions for parametric study sintering model of case I, VIII	90
Figure 4-1. (a) The fractured notched plate with a hole specimen tested in [99] and (b) the crack path calculated with phase field damage model with displacement input of 2mm.	101
Figure 4-2. The load vs displacement of during the simulation of crack propagation. ..	102

Figure 4-3. SEM image of oxidized APS-TBC specimen with denotes of microcracks near the interface [101].	103
Figure 4-4. The geometry model used in the FEM analysis with implemented crack located at the off-peak of the roughness.	104
Figure 4-5. The mesh refinement near the crack with two orientations (a) follow the crack growth; (b) follows the initial crack direction. Both meshes have the maximum element size of 0.03 μ m at the crack propagation zone.	105
Figure 4-6. The phase field damage zone at 3600s (almost the end of cycle 1) for mesh (a) and (b)	106
Figure 4-7. Surface plots of the crack phase field from cycle#1 with initial crack, to cycle#7 for reference case IX	107
Figure 4-8. Surface plots of the damaged first principal stress distribution from cycle#1 with initial crack, to cycle#7 for reference case IX.	108
Figure 4-9. Surface plots of the crack phase field from cycle#1 to cycle#30 for case X with AR=15/24.	109
Figure 4-10. Surface plots of the damaged first principal stress distribution from cycle#1 to cycle#30 for case X with AR=15/24.	109
Figure 4-11. Surface plots of the crack phase field from cycle#1 to cycle#30 for case XI with AR=5/24.	110
Figure 4-12. Surface plots of the damaged first principal stress distribution from cycle#1 to cycle#30 for case XI with AR=5/24.	110
Figure 4-13. Surface plots of the crack phase field and the damaged first principal stress distribution from cycle#1 to cycle#30 for case XII with cracks at mid-level.....	111

List of Abbreviations

Abbreviation	Description
α	Alpha phase
APS	Atmospheric plasma spray
β	Beta phase
BC	Bond-coat
DC	Direct current
EI	Elastic
EB-PVD	Electron-beam physical vapor deposition
FEM	Finite element method
FOD	Foreign object damage
NDE	Non-destructive Evaluation
NDOF	Number of degree of freedom
RE	Rare-earth elements
REO	Rare-earth oxides
RF	Radio frequency
sint	Sintering
SEM	Scanning electron microscope
SPS	Suspension plasma spray
t'	Tetragonal-prime phase
TBC	Thermal barrier coating
TC	Top-coat
TGO	Thermally-growth oxide
Vp	viscoplastic
γ	Gamma phase
Γ	Crack surface
YSZ/7YSZ	Yttria-stabilized zirconia

Nomenclature

Symbol	Description
A_0	Proportional constant
A_{nor}	Norton power law proportional constant
a	Roughness height
AR	Roughness aspect ratio = a/w
b	Coating thickness
C	Compliance matrix
CTE	Coefficient of thermal expansion
C_p	Air heat capacity
d_b	Critical length of unbonded area length
d	Phase field variable
\tilde{D}	Phase field crack driving state function
δ	Prescribed displacement
E	Young's modulus
E_0	Densified YSZ Young's modulus
ε	strain
\dot{G}	Free energy of sintering model
h	Heat transfer coefficient
h_{elem}	Max element size
H	Total thickness of coating
H_{TGO}	TGO thickness
H_0	Initial thickness
j	Flux
k	Thermal conductivity
l_{int}	Phase field length scale
m	TGO growth exponent
n	Norton power law stress exponent
Λ	Viscous matrix
Pr	Prantl's number
Π	Difference between free energy and energy dissipation
Ψ	Energy dissipation of sintering model
ψ	Elastic strain energy in phase field model
Q_0	Activation energy
q	Heat flux density
R	Gas constant
Re	Reynolds' number
S	Surface
σ	Stress
T	Temperature
t	time
v	Migration velocity
w	Roughness wavelength
wt%	Weight percentage

1. Introduction

For the latest aero and industrial gas turbine engines, the demand for better efficiency requires a higher inlet gas temperature in the hot section components of gas turbines. However, the current single-crystal superalloys reached their limit of temperature capabilities after development for the past several decades. Researchers are devoting to two alternate solutions: thermal barrier coatings (TBC) to reduce the temperature of metals and air cooling systems by ventilating within the internal duct and bleeding the air to generate an air film on the blade surface [1]–[3]. Herein, the research is focused on TBCs. The TBC system is a two-layer coating system with top coat (TC) for thermal barrier performance and bond coat (BC) to bond the ceramic TC with the metallic superalloy substrate. During the thermal cycles, a thermally grown oxide layer (TGO) is formed between TC and BC. Due to the harsh operating environment, the materials of the TBC system require a) phase stability at high temperature; b) phase compatibility between the layers to ensure the adhesion; c) similar CTE between layers to reduce the thermal stress, and d) low thermal conductivity [4].

The thin layer of TBCs show outstanding performance that allows the inlet gas temperature to increase by 100 - 150°C consequently reduce the substrate temperature significantly to extend the lifespan of hot section components by minimizing the creep and oxidation damage. However, the prime-reliant TBCs have not been fully realized. Premature failures were found in the early stage of the lifespan, thus limiting its application under a high-temperature environment. A number of factors are causing the TBCs failures, including the manufacturing quality control, severe bond coat oxidation, thermal mismatch of coating layers, top coat sintering, component phase transformation,

etc. [4], [5]. It is of value to better understand TBC failure mechanisms to improve its performance. Therefore, the present thesis will use numerical modelling techniques to simulate the thermal cycle behaviour of TBC systems, conducting a number of parametric studies and evaluating failure mechanisms of TBCs.

The failure of TBC commonly occurs by the delamination near the TC/TGO interface, where the stress accumulated due to the thermal mismatch. Since the atmospheric plasma spray (APS) TBC with porous structure consists of thousands of horizontal microcracks, the large-scale delamination may initiate with the propagation of these microcracks [6]. With the trending phase field damage model, the crack propagation direction and length can be determined based on the energy release rate and critical stresses.

The objectives of the thesis are to study the stress distribution evolution and simulate the crack propagation by the phase field damage model near the TC/TGO interface. The stress distribution and time evolution at TC are firstly simulated with conventional FEM with multiple time-temperature-dependent features: creep relaxation, oxidation growth, and the densification of TC with sintering. A series of parametric studies of these time-dependent material features is performed to validate the results. Based on the FEM model, the initial microcracks are implemented at the TC interface, the phase field damage model is working as an overlay on the displacement field to determine the crack propagation direction and length. The crack study results can better discover how the coating fails than the conventional stress analysis.

The thesis consists of the following parts. Chapter 2 will have the background review of TBC materials, its manufacturing method, the material model, common failure

mechanism, the life prediction methods, and the review of the damage models. Chapter 3 will simulate the stress distribution near the TC/TGO/BC interface, with a series of parametric studies including different TGO growth rates, the roughness aspect ratio, the sintering model and conventional isothermal temperature field. The results can inspire the potential reasons of coating failures. Chapter 4 will simulate the cracks near the off-peak of the interfacial roughness. The stress distribution comparison with previous analysis will be discussed to validate the results. A series of parametric studies like different roughness aspect ratio and different crack location are presented to validate the estimation of how geometry change affects the coating failures. A conclusion and future work recommendation are provided in Chapter 5.

The up-to-date list of published papers for the current research is shown as follows:

1. J. Yan, X. Wang, K. Chen, and K. N. Lee, "Sintering modeling of thermal barrier coatings at elevated temperatures: A review of recent advances," *Coatings*, vol. 11, no. 10, p. 1214, 2021.
2. J. Yan, X. Wang, and K. Chen, "Materials Science & Technology 2022," in *Failure Behavior Analysis of Thermal Barrier Coatings under Adverse Environment: Analytical and Numerical Modeling* .

2. Background and Literature Review

In this chapter, the constituents and manufacturing methods of TBC systems are outlined in a high-level summary in 2.1 and 2.2, giving an overview of failure factors in the scope of materials and manufacturing quality. A following section 2.3 discusses the failure mechanism near the interface of each layer. The material degradation models applied in this thesis are outlined in this section. The following sections 2.4 and 2.5 present the trending damage models applied in the FEM solvers and the iteration of phase field damage model that applied in this thesis.

2.1. Constituents of TBC system

Commercial TBC systems commonly consist of two layers: the top-coat (TC) with extremely low thermal conductivity and the bond-coat (BC) with phase compatibility with both TC and superalloy substrate. A thin layer of thermally-growth oxide (TGO) will be generated progressively between BC and TC during the thermal cycles, and such process normally generates the main source of stresses that typically causes the TBCs failure. The cross-sectional microstructures of the electron-beam physical vapor deposition (EB-PVD) TBC system on an aeroengine turbine blade is demonstrated in Figure 2-1 [4].

The ceramic TC plays a significant role as a heat shield in the TBC system, because of an extremely low thermal conductivity targeting to reduce the conduction of heat. The selection of TC material must meet the following criteria: (1) low thermal conductivity (k); (2) Closely match thermal expansion coefficient (CTE) with BC and substrate; (3) Phase stability during the thermal cycles; (4) Sintering resistance at

elevated temperature and (5) low Young's modulus E for strain compliance [5]. The following introduction of the TBC systems will base on its layers of material.

2.1.1. Top-Coat (TC)

The material for commercial TC is zirconia ZrO_2 partially stabilized by 7-8 wt% yttrium oxide Y_2O_3 , and normally this combination is referred to as YSZ or 7YSZ from literature. The thermal conductivity of the YSZ is varied depending on deposition methods: for EB-PVD method, its typical conductivity value $k = 1.5 - 1.9 Wm^{-1}K^{-1}$; while for atmospheric plasma spray (APS) deposition, the thermal conductivity is even lower ($k = 0.8 - 1.1 Wm^{-1}K^{-1}$) [5], [7]–[10]. The thermal conductivity of YSZ increases up to $k = 2 Wm^{-1}K^{-1}$ during the heating period in thermal cycles, as the sintering process will heal its porous structure [11]. Recent research focuses on further reducing thermal conductivity by increasing the sintering resistance through co-doping rare-earth (lanthanide) oxides (REO) into YSZ or adding larger lanthanide elements into ZrO_2 to produce zirconate pyrochlore oxide (RE_2ZrO_7). An addition of rare-earth elements changes the crystal structure to reduce the phonon absorption coefficient and sintering diffusion rate [12]–[14].

Phase stability is another key factor to prolong the life time of TC. During the cool-down period, the phase diagram indicates that the phase of pure ZrO_2 will transform from the tetragonal crystal structure (t) to monoclinic (m) and cubic (c) structure. The phase transition causes failures by initiating cracks and volume change, also incompatibility phase of ZrO_2 with TGO causes decohesion. The addition of 7-8 wt% yttrium oxide (Y_2O_3) in ZrO_2 , makes the coating deposited as a tetragonal-prime structure (t'-YSZ), which is a metastable phase from 1473 K to ambient temperature. To keep the

phase stable, the addition of pyrochlore oxides was found to stabilize ZrO_2 at the temperature of 1823 to 2473 K, showing the potential to be an alternative material as TC [5], [12], [15].

As a multi-layer coating system used at a wide temperature range, the CTE of each layer should be close to eliminate the lateral residual stress and radial stress at the interface, caused by the thermal mismatch. The materials used for commercial TBC systems are closely matched in CTE. The CTE of IN737 superalloy substrate ($16 \times 10^{-6} K^{-1}$) is close to the CTE of NiCoCrAlY (BC) ($17.5 \times 10^{-6} K^{-1}$) [2]. However, the CTE of 7YSZ ($10.7 \times 10^{-6} K^{-1}$) and Al_2O_3 ($9.6 \times 10^{-6} K^{-1}$) [2] are much lower than the substrate materials, which induce tensile stress during the heating period and compressive stress at the cooling period in a thermal cycle. The radial stress near the interface roughness can go up to 400 MPa due to the thermal mismatch. In this case strain compliance is a significant role to the stress level. The coating manufacturer always prefer a lower E material to reduce the stress level to avoid failures. The elastic modulus E of densified YSZ is ~ 170 GPa at room temperature. In the unaligned splats in APS TBC and columnar structures in EB-PVD TBC, the as-deposited YSZ coating has a porous microstructure, that strongly reduces its macroscopic elastic modulus (~ 60 GPa) at room temperature and decreases the in-plane stress level in TC.

2.1.2. Bond coat (BC)

An intermetallic bond-coat (BC) is a layer of metal applied to the superalloy substrate, providing bonding capabilities with both superalloy blade and YSZ top coat. Uncoated nickel-based superalloys normally form complex and a multi-layer oxide scales, which is not stable with YSZ top coat [4]. There are two types of materials being

developed, e.g., platinum-modified nickel aluminide (Pt- β -NiAl) deposited by pack cementation method and MCrAlY alloy (M represents one or more of Co, Ni, and Fe) applied with plasma sprayed method. Both types of bond coats are the source of aluminum to form the α -phase aluminum oxide (α -Al₂O₃), which is a phase compatible (with TC), thermodynamically stable, slow growing, and adherent oxide scale. [4], [5]

2.1.3. Thermally grown oxide (TGO)

The intermediate layer TGO is progressively grown by the oxidation of BC, in the form of α -Al₂O₃ at elevated temperature. When the TC is deposited, the TGO has an initial thickness $H_{TGO} = 1\mu\text{m}$ [16], [17]. It grows rapidly at the early stage of thermal cycles, then the growth rate is slowed down logarithmically with the protection of the underlying oxide. The laboratory test finds that TBCs typically fails when the H_{TGO} reaches 6 to 12 μm [18]–[20]. Therefore, the thickness of TGO is one of the indicators for life prediction. The growth of TGO with a numerical equation is discussed below.

2.2. Manufacturing methods of TBCs

2.2.1. Atmospheric Plasma Spray (APS)

APS deposited TBCs are typically applied in components like combustion chamber and nozzle guide in an aero-engine [10], [21]. Within the plasma gun, neutral gases like Ar are injected into the plasma torch. Under the high voltage, the direct current (DC) arc or radio frequency (RF) will discharge and generate the plasma, at the temperature of 8000 K or more, which is capable of melting almost anything including the YSZ powders. The YSZ powder particles are injected into the plasma flow, melted, and accelerated within the chamber, then hit the substrate (BC) to form the top coat. When hitting the substrate, the melted or semi-melted particles are flattened into tablets

(or splats) and solidify in a short time [22]. The cross-sectional area of APS deposited TBC is shown in Figure 2-2 and the layered splats with interlamellar cracks are demonstrated. Even though the particles have close sizes, the conditions for the solidification process are varied, making the splats in varied shapes. Large pores and microcracks commonly exist within the coating. The detailed demonstration of the whole spraying process and condition of particles after deposition is shown in Figure 2-3. These properties are considered beneficial to the coating as it allows greater strain tolerance, and decreases the thermal conductivity by scattering the phonons to improve its performance. [10], [21], [22]

2.2.2. Electron-beam physical vapor deposition (EB-PVD)

EB-PVD deposition technology was first applied in the 1980s, a method developed later than APS deposition [23]. Peters et al. [9] stated it is favorable in the parts applied in a harsher environment, like the rotating blades at high-pressure turbines, enduring both high temperature and high mechanical load. Click or tap here to enter text. The typical EB-PVD TBCs have a columnar structure, and an SEM image is shown in Figure 2-4. To be clear, the columns are not free-standing but bonded with asperities at the side of the columns. The columnar gaps contribute to the in-plane strain compliance making it favorable to the parts working under heavy mechanical load. But the through-thickness gaps are unable to block the external gas and contaminants, making it easy to be infiltrated by oxygen, sand particles, and debris during the operation to shorten the life time [24]. Also, the heat resistance performance is relatively lower than the APS deposited TBCs [10].

Figure 2-5 shows the schematic of a typical EB-PVD deposition facility and the process. Under the vacuum environment, the electron beam will heat the target materials in the crucible and then melt them into vapor. The vaporized YSZ will rise and deposit onto the substrate. Upon the vapor phase condensation, the YSZ TC is formed [25]. The vaporizing process transforms the particles into extra fine particles and therefore they are deposited as columnar grains with a radius of about 15 μm .

2.2.3. Suspension plasma spray (SPS)

The coarse APS splats with low compliance are sometimes hard to fulfill the requirement for working under heavy mechanical load and EB-PVD coatings with a very fine structure are expensive and require a strict manufacturing environment. Therefore, the suspension plasma spraying (SPS) method was developed, as an alternative to the conventional methods to deposit coating with finer grain than the APS method and lower cost than the EB-PVD method.

The suspension plasma spraying (SPS) process approximates the same as the APS deposition (refer to Figure 2-3) by applying the suspension or solution feedstock instead of powder feedstock [26], [27]. Once the suspension is injected into the plasma flow, the solvent is vaporized at a high temperature and only the YSZ particles will be accelerated and deposited onto the substrate. The suspension droplets are much smaller than the finest powder, with a diameter of less than 5 μm while the powders are in the size range of 10 to 100 μm [10], [26].

Figure 2-6 demonstrates the morphography of SPS TBC coating. It shows columnar grains in the cross-sectional image, with a similar shape to the EB-PVD coating but in a much greater grain diameter. The top view shows a cauliflower pattern that is

similar to EB-PVD coating. Bernard's report [10] shows that the SPS columnar structure can be modified with different manufacturing inputs. With lower plasma enthalpy and higher suspension feed rate, the columns will be more compact, and fewer interlaminar gaps are found, showing a similar performance to APS deposit and vice versa.

2.3. Failure mechanisms and lifetime prediction

To better predict the life of TBC coatings, it is significant to understand the major failure mechanisms. In a multi-layer composite system operating at elevated temperatures, the failure can raise by multiple factors including the thermal mismatch between layers, sintering of top coat, material degradations, irregular geometry at the interface, etc. These are known as intrinsic failure mechanisms summarized by Gleeson [4]. The extrinsic failure mechanisms including the foreign object damage (FOD) are not discussed in this research.

2.3.1. Thermal mismatch failures

The failure of the TBC system is commonly initiated by propagating the pre-existing cracks near the interfacial area. For an ideally flat interface, all the stress is in the tangential direction, but it is not realistic in the microscopic level. At deposition, the initial roughness height (a) is in a range from 7 to 12 μm depending on the manufacturing inputs like powder size, plasma flow rate, etc. [28]. During the thermal cycles, the material data showed that TGO has a relatively low CTE than substrate superalloy and BC [29], it is stretched at heating. With creep relaxation, the stress level is relaxed at an elevated temperature at all the layers. When it is cooled down, the TGO with small CTE is compressed and the interface will be roughened as an undulating shape progressively at every thermal cycle. It is irreversible and commonly named as "ratchet

effect” at the interface[5], [30]. Detailed demonstration of the ratchet effect is in Figure 2-7. The undulating interface can be formed after several thermal cycles. Regarding the plasma spray process discussed in Section 2.2, the semi-melted particles are unable to fit the shape onto the interface roughness, leaving the gap between TC and TGO that reduces the contact area and lose adhesive performance. Figure 2-8 shows the cross-sectional SEM images of the interface area of APS TBCs. The SEM images displayed that the roughness continuously or individually existed at the TC/BC interface and their sizes are varied. The height ranges from a few microns to 50 μm . It is not feasible to identify which roughness is initially formed and which is formed during thermal cycles, but a clue is the size of the roughness grows continuously during the thermal cycles [31], [32] The yellow arrows in the figure indicate that horizontal cracks are nucleated near the interfacial roughness. The evolution of these cracks will be simulated in Chapter 4.

With the interfacial microstructure, residual stress is accumulated at the peak and valley of the roughness due to the thermal mismatch between TC and BC. A simple mechanic model in Figure 2-9 sketched by Rosler et al. explains the radial stress near the roughness as TGO grows [29]. Through the thickness, the TBC system is considered as a series of springs, the different elastic modulus of TC and BC has different spring rates, and their initial length depends on the position they are located: peak, off-peak, or valley. Figure 2-9 (a) demonstrates that at the peak location the model has an extra segment of stiffer spring and at the valley the model consists of a softer spring representing TC. The springs are parallel in the horizontal direction. When the coating is heated and held for some time, the creep deformation relaxes the residual stresses. When the system is cooled down, Figure 2-9 (b) shows that the high *CTE* BC shrinks more than the TC does,

causing tensile stress at the BC peak and compression stress at the TC valley. When the TGO grows (see Figure 2-9 (c,d)), which has the lowest *CTE* and highest *E*, the low shrink rate upon cool-down constrains the shrinkage of BC and TC. Thus, in theory, tensile stress is accumulated at the BC peak and TC valley. However due to the thin TGO, the TGO deformation is constrained by both BC and TC, while the TC valley is still in the state of compression. When the TGO continues growing shown in Figure 2-9 (e), the TGO layer dominates the load at the interfacial area, the TGO with the least contraction at cool-down induces tensile stress at both BC peaks and TC valleys. The simulation result of Aktaa et al. [33] reads that the maximum residual stress at the concentration zone is up to 500 MPa. The interlamellar cracks residing near the interfacial area can propagate rapidly to relax the stress. In Chapter 3 a stress analysis simulation at the interface will be performed to validate the prediction by the sinusoidal interface model, and in Chapter 4, the initial cracks will be implemented in the solid and crack propagation will be simulated by phase field method.

Buckling is a greater scale of failure mechanism introduced by Mumm and Evans [34]. With rumpling, the thermal mismatch loads propagate the microcracks near the interface and merge with cracks at other areas. It finally becomes a long crack up to a few millimeters. A large gap is formed between the layers, and once the TBC system is cooled down, the strong compressive stress at TC will lead to the buckling. The spallation of the coatings will eventually lose the heat-resistant performance from TC. Clarke and Levi [5] stated that the TC buckling is governed by the standard Euler buckling condition of a column:

$$\frac{\sigma}{E} = 4.8 \left(\frac{H}{d_b} \right)^2 \quad (2.1)$$

where H is the coating thickness, and d_b is the critical length of unbonded area length. Normally the thickness of TC is thicker than $100\mu\text{m}$, and the critical length of buckling will be a few millimeters.

2.3.2. Material degradation

At such high operating temperatures up to 1500 K, elements are highly activated, and the material properties of the coatings change with temperature and time evolution. The material model applied in the simulation should be time-temperature dependent to accurately describe material behaviours. For TC, the porous 7YSZ ceramic sinters at high temperatures. Some microcracks and small-scale interlamellar cracks will be healed. Two effects will contribute to the healing: i) the material will densify and reduce the strain compliance. Numerically, Young's modulus increases with sintering; ii) the volume of coating decreases then the thermal conductivity increases which degrades the thermal barrier performance. Therefore, sintering is one major reason for failures. The densified TC can accelerate the crack propagation mentioned in section 2.3.1 and lead to premature failures [35]–[42]. Therefore, it is significant to consider the sintering effect in the failure mechanism FEM simulations.

Oxides are grown in thermal cycles because the porous structure of TC is unable to seal the atmospheric oxygen away from the interface. The growth of TGO has advantages and disadvantages to the lifespan of the TBC system, making the trade-off significant. The $\alpha\text{-Al}_2\text{O}_3$ TGO is ceramic and phase compatible with TC making it adhesive with TC. Also, the densified Al_2O_3 is protective to the underlayer BC to reduce

further oxidation, which extends the life of metallic BC at elevated temperatures. However, Sohn et al. [43] indicated that as the TGO thickness increases, the depletion of β -NiAl transformed into γ -phase in the MCrAlY bond coat loses its phase stability with α -Al₂O₃, and decohesion with TGO happens. Darolia [30] and Rabiei [44] observed that localized spinel oxide (Co, Ni, Cr) is formed at the voids between the TC and TGO, which are contaminants and unable to provide adhesion and nucleate TC cracks. Also, the rumpling of TGO increases the radial stress near the interface making the TC spalls and this is the main concern in our research. According to Wu et al. [18], the average thickness of TGO at failures of TBCs is about 10 μ m, therefore our research considers the TGO growth before its decohesion happens. A TGO growth model is introduced in section 2.3.2.2. The model only considers the stress pattern with TGO growth, while the phase transition lead failure is not coupled in our model. This is because of the difficulties of correlating the phase transition with the adhesion at the TC/TGO and TGO/BC interface.

2.3.2.1. TC sintering model

Sintering model is gradually coupled in the past two decades for the FEM simulation on TBC systems. At the early stage, the effect of YSZ aging was ignored in FEM stress analysis on TC/TGO interface. For example, Ranjbar-far et al. [31], Rosler et al. [29], [45], and Song et al. [17] used temperature-dependent YSZ material properties to study the interfacial roughness effects on the stress distribution. The stress state could be highly underestimated due to the negligence of material degradation. Kyaw et al. [46] used an Arrhenius-type rate equation to fit the experimental data of the YSZ TC to describe elastic modulus evolution, then establishing temperature-dependent and time-

dependent material model. The coefficients of the fitting equation change with time, thus making it highly dependent on the test data quality. In their model, the elastic moduli data are used when test samples are sintered at 1, 11, and 120 hours, respectively. It is hard to evaluate the evolution of elastic moduli between these sintering periods without extra tests. Lv et al. [47] applied the time history curve of relative density of the coating to evaluate the corresponding elastic modulus curve during the sintering process, but this approach doesn't include the variation of sintering temperatures.

Herein, applying a constitutive sintering model developed via variational principle would be a more comprehensive option for FEM simulations. As mentioned in section 2.1.1, the deposition process makes the TC full of microcracks, interlamellar pores, and sphere voids. At elevated temperatures, the atoms in the porous ceramics are highly mobilized to diffuse along the lattice, grain boundaries, and pore surface to minimize the free energy of the surface. Cipitria et al. [41], [48], [49] developed a disk-like periodic unit of the YSZ splat with an inter-splat bridge to connect other splats and a brick model to represent the intra-splat microcracks. The schematic diagram is shown in Figure 2-11. Surface diffusion and grain-boundary diffusion will then decrease the height of the bridge and increase its radius to heal the inter-splat pores. The diffusion consumes the free energy of the system, and the free energy will dissipate to the environment due to energy conservation.

Based on the variational principle, the balance between free energy reduction rate \dot{G} (also known as sintering force) and energy dissipation Ψ (or material viscosity) can be established as [48]:

$$\Pi = \dot{G} + \Psi \quad (2.2)$$

To keep the system stable, the difference between dissipation of energy and consumption of free energy is minimized when the time step is infinitesimal:

$$\delta\Pi = \delta(\dot{G} + \Psi) = 0 \quad (2.3)$$

In the geometry in Figure 2-11, the free energy is defined as:

$$G = \frac{1}{V} \left[\int_{A_S} \gamma_S dA_S + \int_{A_{gb}} \gamma_{gb} dA_{gb} \right] \quad (2.4)$$

where V is the volume of the domain, A is the area of the surface or grain boundary, γ stands for the specific energy. The subscript S and gb are surface and grain boundaries.

Energy dissipation is defined as:

$$\Psi = \frac{1}{V} \left[\int_{A_{gb}} \frac{1}{2M_{gb}\Omega\delta_{gb}} (j_{gb}^2) dA_{gb} + \int_{A_S} \frac{1}{2M_S\Omega\delta_S} (j_S^2) dA_S + \int_{A_{gb}} \frac{1}{2m_m} (v_m^2) dA_{gb} \right] \quad (2.5)$$

where M is the atomic mobility, Ω is the atomic volume, j is the volumetric flux per unit length, δ is the thickness of the layer of diffusion, v_m is the grain boundary migration mobility, and m_m is the intrinsic grain boundary mobility. The mobility M and m_m are derived from the diffusivity of the materials. The three components in Eq. (2.5) are grain boundary diffusion, surface diffusion, and grain boundary migration.

In the case of mass conservation, and no addition or subtraction of material q , the flux j equals the migration velocity v :

$$\nabla j + v = q = 0 \quad (2.6)$$

With Eq. (2.6), the surface and grain boundary flux can be related to the velocity of geometry deformation in terms of disk radius \dot{r} , height \dot{h} , bridge height \dot{z}_s , number of grains \dot{N}_s , microcrack opening \dot{a} , and splat width \dot{y}_c . The dots on the dimension are the rate of its change. Eq. (2.3) is then expressed as:

$$\Pi(\dot{h}, \dot{z}_s, \dot{r}_s, \dot{N}_s, \dot{a}_s, \dot{y}_c) = \frac{\partial G}{\partial t}(\dot{h}, \dot{z}_s, \dot{r}_s, \dot{N}_s, \dot{a}_s, \dot{y}_c) + \Psi(\dot{h}, \dot{z}_s, \dot{r}_s, \dot{N}_s, \dot{a}_s, \dot{y}_c) \quad (2.7)$$

The simulation result of this model has been validated with the test result, which shows it has a close fitting to the trend of contraction in radial and tangential direction, porosity, and specific surface. And a parametric study of different splat geometry is conducted to prove its consistency. The model is specifically developed for APS deposited coating, similar models developed by Hutchinson et al. [50] and Kumar and Cocks [51], [52] have simulated the microstructure evolution of EB-PVD coating by curing of asperities connecting the columns.

In Cipitria's sintering model [41], [49], Young's modulus is held fixed during the sintering process, which is impractical for the actual scenario and makes the life prediction model overestimated. Cocks and Fleck [53] attempted to add an empirical knock-down factor to estimate the effective Young's modulus as a fraction of densified YSZ Young's modulus E_0 based on the asperity spacing at the penny-shape cracks that distributed in the densified YSZ. The results showed that the effective modulus increased from $\sim 0.5E_0$ to E_0 during the designated sintering characteristic time. The free constrained case spends about half time to reach the fully sintered status compared to the case with superalloy substrate constraint. Later, Lv et al. [54] developed a more practical

method to simulate the elastic modulus development of the YSZ TC with the consideration of elastic, viscoplastic, and sintering stress. To reflect all these factors, Lv et al. [47], [54] used a constitutive model made by Gasik and Zhang [55] to determine the stress-strain relationship for a thermal elasto-viscoplastic model as shown in a schematic block diagram in Figure 2-12. The equation describing the constitutive relation is:

$$d\varepsilon = \{d\varepsilon^{El}\} + \{d\varepsilon^{Vp}\} + \{d\varepsilon^{sint}\} \quad (2.8)$$

where El is elastic, Vp is viscoplastic and sint is sintering. The sintering model used is close to Cipitria et al.'s model, but with the modification of geometry. Figure 2-13 demonstrated the sintering behavior of the periodic unit used in our model. As sintering proceeds, the microcracks will be healed and densified as a dense solid. Thermal expansion in the Figure 2-12 is neglected in the model of Lv et al [54] for the purpose of simplicity. The Eq. (2.8) can be further expanded as:

$$\dot{\varepsilon} = [C]\{\dot{\sigma}\} + [A]^{-1}\{\sigma\} - [A]^{-1}\{\sigma^{sint}\} \quad (2.9)$$

where $[C]$ is the compliance matrix, $[A]$ is the viscous matrix and σ is the residual stress at coating and σ^{sint} is the sintering stress caused by diffusivity at the surface and grain boundary. The stress can be converted by strain with the compliance matrix, but in this case, the compliance matrix $[C^*]$ is in a modified form including the term of viscosity.

$$\{\Delta\sigma\} = [C^*]^{-1} \langle \{\Delta\varepsilon\} - [A]^{-1}\{\bar{\sigma}\}\Delta t + [A]^{-1}\{\sigma^{sint}\}\Delta t \rangle \quad (2.10)$$

where

$$[C^*] = [C] + [A]^{-1}\Delta t/2 \quad (2.11)$$

The microscopic modulus can be determined by the modified compliance matrix $[C^*]$. According to Lv et al.'s simulation, the elastic modulus grows from 110 to 170 GPa, where 170 GPa is the elastic modulus of bulk YSZ [56].

In practice, the elastic modulus of TC is much lower, to 60 – 80 GPa. It is mainly caused by the strain relaxation of vertical crack and the modulus is named as macroscopic modulus. To determine the macroscopic modulus, a finite element periodic model with a vertical crack is built, shown in Figure 2-14. A tensile load is applied to the side edges of the periodic FEM model, and the read the displacement result of the edges. Apply the relation that $E = \sigma/\varepsilon$, the macroscopic modulus is evaluated. In Lv et al. model [54], the macroscopic modulus grows from 24 to 32 GPa at elevated temperature, which is closely fitted to the thermal-mechanical analysis (TMA) result obtained by the test. The result comparison shows in Figure 2-15.

In our model, the sintering-induced macroscopic modulus increases as sintering time and temperature decrease, is a time-temperature-dependent model, to best describe the material properties evolution. Also, the sintering rate at different temperatures is varied, the elastic modulus contours are generated for different sintering temperatures. Figure 2-16 demonstrated the evolution of macroscopic in-plane elastic modulus evolution of APS-TBC using the model of Lv et al.[54] at elevated temperature. The modulus increases in an almost linear way at the first stage, then slow down when the side bridges are fully sintered. It takes about 6×10^5 s or ~ 170 h to reach fully sintered and the macroscopic modulus grows from 23 to 32.5 GPa. The time-dependent elastic modulus of YSZ was determined by in-situ measurement since it needs to be conducted

at elevated temperature [57] and the result is listed in Table 3-3 in the Chapter 3. With interpolation, a surface contour plot is generated for the time and temperature-dependent elastic modulus of YSZ TC in Figure 2-17 and this is the model applied in thesis simulation.

2.3.2.2. TGO growth model

An empirical model fitted with a phenomenological oxide growth process is introduced by Busso et al. [58]. The total thickness H_{TGO} of the oxide layer with temperature T and time t expresses as

$$H_{TGO} = A_0 t^m \exp\left(-\frac{Q_0}{R}\left(\frac{1}{T} - \frac{1}{T_{ref}}\right)\right) \quad (2.12)$$

where A_0 is a proportional constant, m is the growth exponent, Q_0 is the activation energy, T_{ref} is the reference temperature at 2424 K, and T is the input temperature at the TGO. The NiAl alloy in BC is easily oxidized and therefore an average of 1 μ m BC is oxidized before TC is deposited [16], [17]. With this model, the TGO spends around 1000 hours growing to 6 μ m and around 5000 hours growing to 10 μ m at 1293 K, which matches the expected lifespan of YSZ TBC coatings [58]. The parameter values of the equation are given in the Chapter 3. Figure 2-18 illustrates the TGO growth over oxidation in the first 10 thermal cycles of the model. It starts growing when the coating reaches the service temperature and pauses when the heating period ends. The TGO growth model is achieved by material switching from BC to TGO during the heating period. The stress induced by the material switch is eliminated by the creep model at elevated temperatures. Considering the time cost of simulation, and the significance of the TGO growth to the stress distribution, the growth rate is accelerated to make it grow

to 6 μ m in the first 30 hours at 1343 K. Parametric studies will be discussed in Chapter 3 and 4.

Recently, an advanced approach for phase transformation was developed with the phase field method. Sait et al. [59] and Zhou et al. [60] have developed a chemo-diffusion phase field model, simulating the oxidation process of bond coat at the top surface. Material progressively undergoes a phase-change to TGO shows a similar trend to the experimental result and the transition from layer to layer is smoother and more realistic since it uses a phase field variable to control the material switch. Additionally, with the wide compatibility of the phase field model, it is well coupled with the structural model with phase field damage. However, due to the lack of understanding, the phase field diffusion model is not coupled in our research.

2.3.2.3. Creep model

Elastic-viscoplastic creep behavior of the TBC system layers is considered in the simulations except for the superalloy substrate features with creep-resistant. Under the thermal load at a temperature higher than 873 K, dislocation within the TC, TGO, and BC can constantly reshape its microstructure and relax the residual stress [61]. An experiment has demonstrated that the creep behavior is fitted with the Norton power law. This model has been widely applied in multiple TBC system failure studies with FEM analysis [17], [29], [46], [62]–[64]. The governing equation expresses as Eq. (2.13) in COMSOL Multiphysics [65].

$$\dot{\epsilon}_{cr} = \frac{\partial \epsilon}{\partial t} = A_{nor} \sigma^n \quad (2.13)$$

where $\dot{\epsilon}_{cr}$ is the creep strain rate, A_{nor} is the creep rate coefficient, σ is the residual stress, and n is the stress exponent. Since the creep effect only happens at high temperature, the creep rate coefficient will activate when the temperature is over 1123 K. The creep data of TC, BC, and TGO are given in the Chapter 3.

2.3.3. Life prediction

Life prediction is the prevailing trend for TBC systems research because a reliable prediction method can detect potential early failures, maximize performance, or extend the gap between overhauls.

Clarke and Levi [5] introduced several non-destructive evaluation (NDE) methods to detect the microstructure without destroying the coating. Infrared imaging method can visualize the large-scale separation of TC to prevent the buckling spallation. Piezospectroscopy method can illuminate the aluminum oxide to detect the TGO thickness to determine its remaining life. Thakare et al. [66] used X-ray diffraction and neutron diffraction to detect the residual stress within the coating by measuring the crystal lattice spacing and making a comparison to the unstressed specimen.

Physics- and/or mechanics-based numerical method is another powerful approach to predict the lifespan of TBCs. The TGO growth model mentioned in section 2.3.2.2 is a commonly used numerical method, combined with FEM, for life time prediction. Since the coating tends to fail at a specific TGO thickness, such as 12 μ m, and the oxidation rate of the metallic bond coat is relatively stable, users can estimate the remaining life referred to the TGO growth model. Zhang et al. [38], [39] used existing coating's life

data, in the combination of the stress model combined with a temperature-dependent crack growth rate formulae, to predict the lifetime of both APS and EB-PVD TBCs.

Finite element method (FEM) is also a powerful tool for predicting stress concentration and small-scale failures. The first step of FEM is to select a proper geometry model to describe coating interfacial features. The sinusoidal [6], [29], [45], [67]–[70] or two semi-circle unit cells [31], [64] are commonly applied to describing the roughness since they are typically analogous to the microstructural SEM images. To make the model more realistic, Abdegawad and Al-Athel [62] used the image processing tool to generate a porous and irregular geometry based on the SEM images. Gupta et al. [71] used 3D scanning techniques to scan the bond coat interface before the TC is applied and then generate a 3D mesh with the scanned data. However, the fine structure requires a heavy computation power due to the complexity of stress patterns and discontinuities, and the result is only valid in the specific case. Therefore, the sinusoidal model with various aspect ratio is applied in our research to simulate the stress state for different size of rumpling. When the geometry is set up, selecting a proper material is essential. As mentioned in section 2.3.2, TBC materials are highly dependent on temperature and time evolution, so the sintering in TC and oxidation growth will be included in the model. Afterward, applying the thermal load with proper structural constraints, the stress magnitude and concentration position can be evaluated. Then the crack propagation model can be implemented to predict the TBCs failure in multiple criteria. The detailed process for this failure simulation will be expanded in the next chapters.

2.4. Damage Model

The failure behaviour of TBCs is affected by complex conditions. In conventional FEM, the simulation results only read the stress states and the corresponding energy density near the interface area. However, the failure behaviour is a dynamic process, which is incomprehensive in conventional FEM studies with static geometry. Damage model is developed as an extension to FEM studies, to compute the crack propagations during the thermal cycles. The stress state is also updated dynamically as the crack propagates.

Wang et al. [72] summarized that there are three significant methods of crack propagation simulation developed in the past decades: The Virtual Crack Closed Technique (VCCT), Cohesive Zone Model (CZM), and eXtended Finite Element Method (XFEM). The VCCT and CZM methods are only applicable on predefined crack, so they are widely applied in the interfacial delamination problems. The XFEM method is predicting the cracks independent to the mesh, which allows it to simulate the undefined crack problem within a solid.

Fan et al. [73] investigated the interfacial delamination of double-layer TBC system with the VCCT method. In his study, the crack at the interface propagates when the sum of strain energy release rate, G , for Mode I and II reaches the critical energy release rate G_c . The crack growth is defined by the length between the node at crack tip and the next node on the path, which means the crack growth rate is dependent on the element size. A series of studies were conducted that examined how different operating temperatures and thickness ratio of two layers of TC and their effect on the final crack length.

The CZM method commonly uses the bi-linear traction separation law as the decohesion criterion. In the as-deposited coating, the traction is linearly proportional to the opening displacement. When reaches the peak cohesive traction, the cohesive performance will be degraded until the opening displacement reaches the failure displacement. The energy required to the failure is called critical energy release rate G_C . Al-Athel et al. [74] uses the CZM model to simulate the decohesion of the TC from the TGO in a TBC system. The crack propagates when the simple mixed-mode criterion of normal and shear critical energy release rate meets. The results showed that the TC near the valley tends to spall away but it stops at the mid-level. The creep relaxation is reduced the length of the crack by relaxing the residual stress. Also, with a shorter interface roughness, the extent of damage is reduced. Song et al. [17] developed a diffusion-coupled cohesive element model to estimate the delamination of TC on TGO. In this study, due to the depletion of Al at the oxidation, the interfacial strength is degraded with thermal cycle time. The results read that the damage is accelerated with the couple of diffusion model, which matches the authors' assumption.

XFEM pushes the crack simulation to another level since this method does not require the definition of initial crack and the crack growth path, makes it possible to simulate the brittle fracture within a solid. The XFEM decouples the cracks or material discontinuities with the background displacement field by using special enrichment functions [75]. The background mesh is formulated with the continuous displacement function, the main body of the discontinuities or crack surfaces are formulated with the Heaviside enrichment function, and the crack tips are formulated with asymptotic crack-tip enrichment function to avoid singularity. The fracture criteria are similarly using the

energy release rate with the quadratic sum of mode I and II stress intensity factors. Jiang et al. [63] uses the XFEM to model the crack propagation within the TC. The results observed that the crack near the TC off-peak propagates during the dwell period and cool-down period in a heat-cycle. The crack grows to the half-way at 1st cool-down cycle and slowly propagates in the remaining cycles. Kyaw et al. [70] uses the XFEM to study the crack propagation of two parallel cracks within the TGO and the TC. The results showed that the crack at TC will completely spall off and the crack at TGO grows from the peak to the mid-level.

In this research, a more recent technique is applied: The phase field damage model. The phase field model has some similar properties to the XFEM: a) it is independent to the mesh; b) crack path is not required to be predefined. The main difference is phase field damage model defines the sharp crack as a diffusive crack, which is controlled by the phase field variable from 0 to 1. When phase field variable equals 1, the material is fully damaged and when equals 0, the material is intact. At the crack topology, the variable equals 1 at the center of crack surface and gradually moves to 0 at the width of diffusive length scale. Zhou et al. [76] indicates that it is the continuous approach, compared to the discrete approach in XFEM and CZM. The discrete approach usually requires more computation power and more complex tracking procedures of the cracks, while the continuous approach can get rid of it. A detail explanation of the steps of phase field model iteration is presented in section 2.5.

2.5. Phase field damage model for brittle fracture

Miehe et al. [77] introduce the phase field diffusive crack propagation method to simulate finite element analysis without modeling discontinuities in the displacement

field. With this built-in feature, it is capable to couple multi-field finite element solvers, e.g. COMSOL Multiphysics.

For a sharp crack surface Γ in the body \mathcal{B} (see Figure 2-20), a crack phase field variable $d(x) \in [0,1]$ is introduced to describe the crack damage condition, where $d = 0$ for undamaged state and $d = 1$ for fully damaged state of the material. It is a scalar to describe the status of material and there is no physical meaning in the simulation. A simple model of a 1-Dimensional bar with a crack at $x = 0$ visualizes the phase field variable at the sharp crack and diffusive crack in Figure 2-19. In this case, the phase field variable is approximated as the exponential function:

$$d(x) = e^{-|x|/l_{int}} \quad (2.14)$$

where l_{int} is the length scale to regularize the sharp crack topology Γ and it has the Dirichlet-type boundary condition: $d(0) = 1$ and $d(\pm\infty) = 0$. It is observed the Eq. (2.15) is the solution of the homogeneous differential equation (Eq. (2.14))

$$d(x) - l^2 d''(x) = 0 \quad in \mathcal{B} \quad (2.15)$$

The Euler equation of Eq. (2.15) denotes

$$d = Arg\{\inf_{d \in W} I(d)\} \quad \text{where } I(d) = \frac{1}{2} \int_{\mathcal{B}} \{d^2 + l^2 d'^2\} dV \quad (2.16)$$

where W is the Dirichlet-type boundary condition above: $W = \{d | d(0) = 1, d(\pm\infty) = 0\}$.

As referred to Figure 2-20, the volume of the diffusive crack is the product of crack surface Γ and length scale $dV = \Gamma dx$, the alternate function of Eq. (2.16) defines as

$$\Gamma_l(d) := \frac{1}{l_{int}} I(d) = \frac{1}{2l_{int}} \int_{\mathcal{B}} \{d^2 + l_{int}^2 d'^2\} dV \quad (2.17)$$

to eliminate the effects of length scale l_{int} . Now the crack surface Γ becomes an equation of phase field variable d .

To extend the functions to multi-dimensional cases, the regularized crack equation (2.17) is defined as

$$\Gamma_l(d) = \int_{\mathcal{B}} \gamma(d, \nabla d) dV \quad (2.18)$$

where ∇d is the spatial gradient, and the crack surface density function per unit volume, $\gamma(d, \nabla d)$, is

$$\gamma(d, \nabla d) = \frac{1}{2l_{int}} d^2 + \frac{l_{int}}{2} |\nabla d|^2 = \frac{d^2}{l_{int}} + \frac{l_{int}}{2} \frac{\partial d}{\partial x_i} \frac{\partial d}{\partial x_i} \quad (2.19)$$

For the multi-dimensional and time-dependent case, the phase field variable d is updated as

$$d(\mathbf{x}, t) = Arg \left\{ \inf_{d \in W_{\Gamma(t)}} \Gamma_l(d) \right\} \quad (2.20)$$

where $W_{\Gamma(t)} = \{d | d(\mathbf{x}, t) = 1 \text{ at } \mathbf{x} \in \Gamma(t)\}$. The Euler equation and the boundary condition are updated as:

$$d - l_{int}^2 \Delta d = 0 \quad \text{in } \mathcal{B} \quad (2.21)$$

$$\nabla d \cdot \mathbf{n} = 0 \quad \text{on } \partial \mathcal{B} \quad (2.22)$$

where Δ is Laplacian, and \mathbf{n} is the outward normal on the solid edge.

The diffusive crack topology on the phase field needs to be adopted with the displacement field to make it effective. The displacement field is defined as Eq. (2.23) in the small-strain assumption.

$$\mathbf{u}: \begin{cases} \mathcal{B} \times \mathcal{T} \rightarrow \mathcal{R}^\delta \\ (\mathbf{x}, t) \rightarrow \mathbf{u}(\mathbf{x}, t) \end{cases} \quad (2.23)$$

coupling with

$$\mathbf{d}: \begin{cases} \mathcal{B} \times \mathcal{T} \rightarrow [0,1] \\ (\mathbf{x}, t) \rightarrow d(\mathbf{x}, t) \end{cases} \quad (2.24)$$

The strain at each element in the FEM model can be calculated by the displacement in each element $\boldsymbol{\varepsilon}(\mathbf{u})$. The global strain energy stored in the solid equals

$$E(\mathbf{u}, d) = \int_{\mathcal{B}} \psi(\boldsymbol{\varepsilon}(\mathbf{u}), d) dV \quad (2.25)$$

where $\psi(\boldsymbol{\varepsilon}(\mathbf{u}), d)$ is the degraded energy storage function per unit volume, is represented as

$$\psi(\boldsymbol{\varepsilon}, d) = [g(d) + k]\psi_0^+(\boldsymbol{\varepsilon}) + \psi_0^-(\boldsymbol{\varepsilon}) \quad (2.26)$$

where ψ_0 denotes the undamaged material, the positive sign denotes the tensile mode and the negative sign is the compressive mode. The undamaged energy function ψ_0 is

$$\psi_0 = (\lambda \operatorname{tr}[\boldsymbol{\varepsilon}]^2)/2 + \mu \operatorname{tr}[\boldsymbol{\varepsilon}]^2 \quad (2.27)$$

where λ and μ are lamé constants.

The $g(d)$ is known as the degradation function,

$$g(d) = (1 - d)^2 \quad (2.28)$$

and it is constrained by these conditions

$$g(0) = 1, \quad g(1) = 0, \quad g'(1) = 0 \quad (2.29)$$

the k in Eq. (2.26) is a small positive number to ensure the tensile part of the equation keeps positive when the material is fully damaged.

The fracture energy required to extend the diffusive crack is governed by

$$W_c(d) := \int_B g_c \gamma(d, \nabla d) dV \quad (2.30)$$

where g_c is the Griffith critical energy release rate, and $\gamma(d, \nabla d)$ is the crack surface density equation defined in Eq. (2.19).

With Eq. (2.25) and (2.30) the body loads, and the external loads, the variational approach of brittle fracture problem can be established in Eq. (2.31)

$$\begin{aligned} \Pi(\mathbf{u}, \mathbf{d}) = & \int_B \psi(\boldsymbol{\varepsilon}, d) dV + \int_B g_c \gamma(d, \nabla d) dV - \int_B \mathbf{b} \cdot \mathbf{u} dV \\ & - \int_{\partial B} \mathbf{f} \cdot \mathbf{u} dS \end{aligned} \quad (2.31)$$

where \mathbf{b} is the body force applied to the solid and \mathbf{f} is the force applied to the solid edges.

With the time derivative of elements in Eq. (2.31), the external force and elastic strain in the body can simultaneously equilibrium with the fracture energy when crack propagates in a time-dependent study. Also, the output of the maximum reference energy ψ_0^+ is stored in the history field, to ensure the process of crack propagation is irreversible. When the condition changes (load changes) and cracks continue to grow during the time-

dependent study, the history field can make sure the cracks are not closed and looks the same as their history [60], [65], [77]–[79]. To determine the transient, the time derivative of Eq. (2.31) is required, but it is not expanded here.

In Miehe’s theory, there is multiple damage criterion available, the one used in our model is the principal stress criterion. The crack propagates when the elastic strain energy reaches the threshold ψ_c . The crack driving state function states

$$\tilde{D} = \left\langle \frac{\tilde{\psi}(\boldsymbol{\varepsilon})}{\psi_c} - 1 \right\rangle \quad (2.32)$$

With the Cauchy stress tensor, the effective strain energy $\tilde{\psi}(\boldsymbol{\varepsilon})$ can be rewritten as

$$\tilde{D} = \left\langle \frac{\tilde{\psi}(\boldsymbol{\sigma})}{\psi_c} - 1 \right\rangle \quad (2.33)$$

Then Eq.(2.33) can expand as:

$$\tilde{D} = \xi \left\langle \sum_{a=1}^3 \left(\frac{\langle \sigma_a \rangle}{\sigma_c} \right)^2 - 1 \right\rangle \quad (2.34)$$

where $\langle \sigma_a \rangle$ is tensile only principal stress and σ_c is the criterion stress. ξ is the post-peak slope parameter.

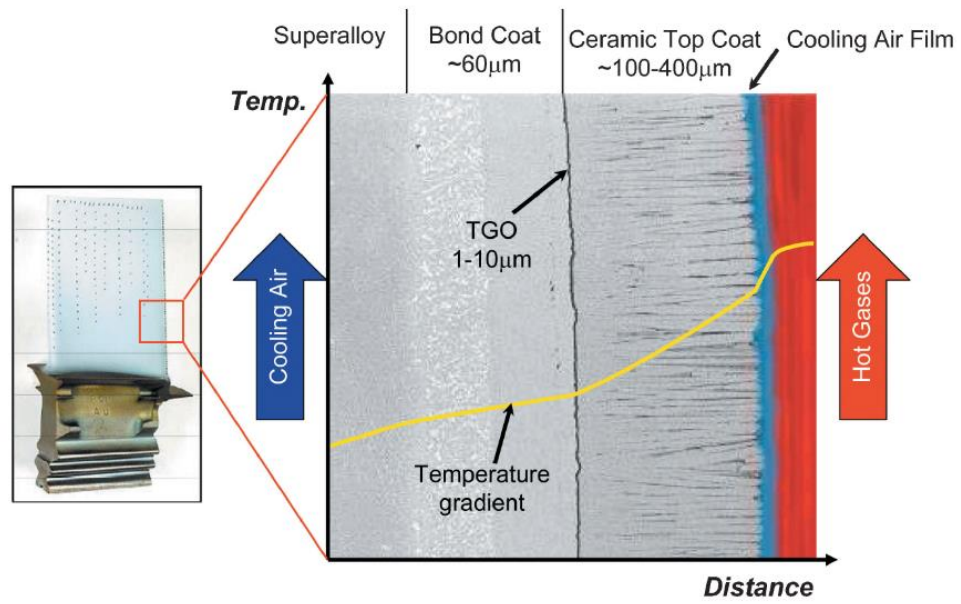


Figure 2-1. A schematic diagram of a TBC system on an aero-engine turbine blade made with an EB-PVD top coat [4]. (Copyright permission, AIAA)

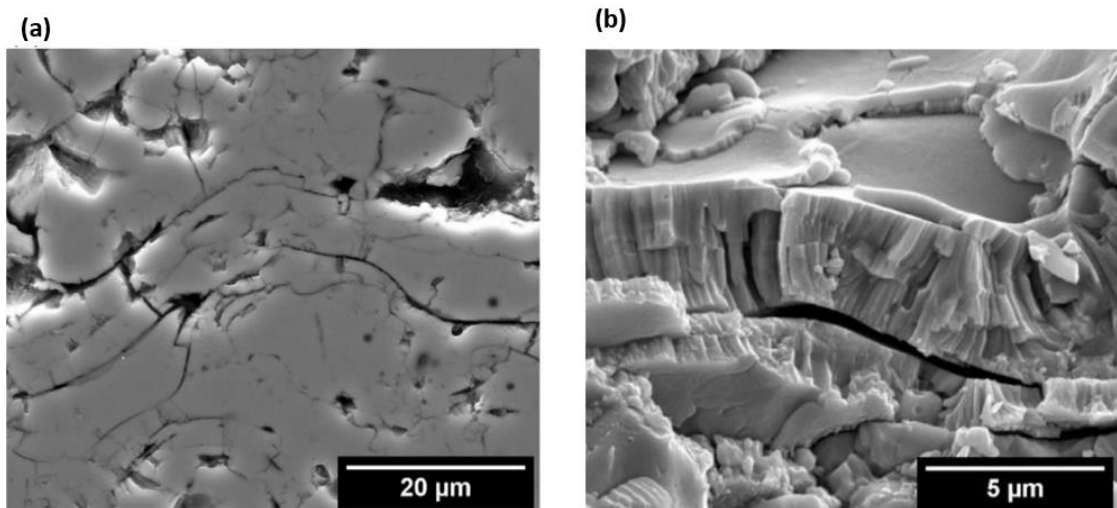


Figure 2-2. The cross-sectional image of APS TBC with (a) normal scale and (b) zoomed scale [80]. (Copyright permission, Elsevier)

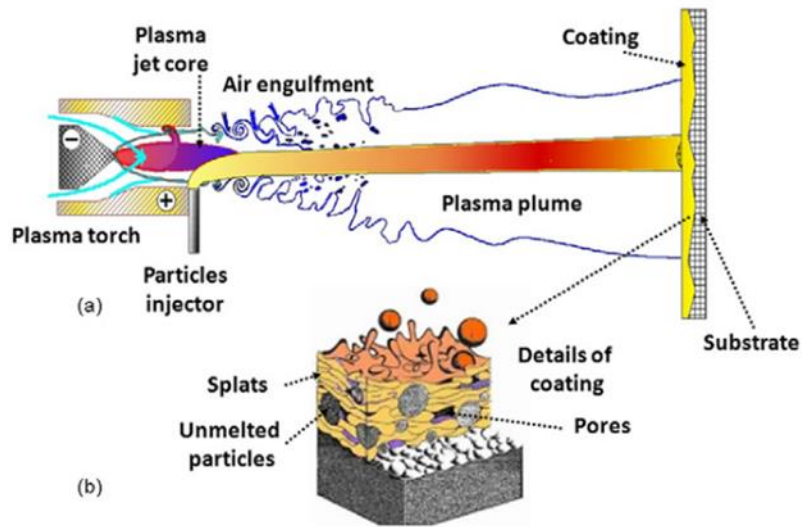


Figure 2-3. (a) A schematic of the APS deposition process; (b) a detail view of the particle deposition to the substrate [81]. (Copyright permission, IOP Publishing, Ltd.)

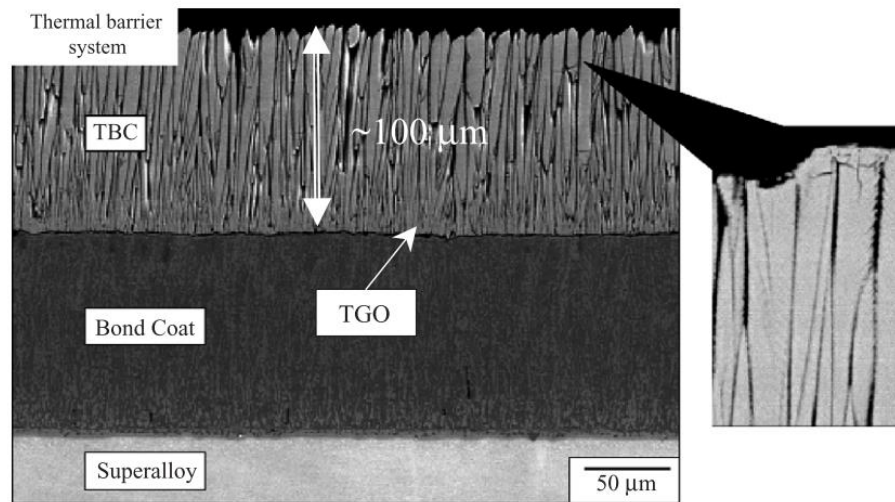


Figure 2-4. The cross-sectional SEM image of the microstructure of the TBC system was deposited by the EB-PVD method[24]. (Open-access)

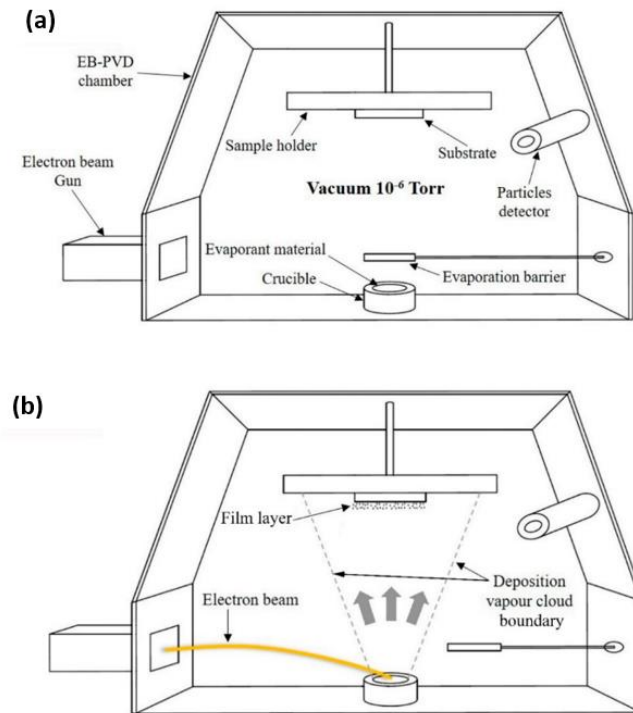


Figure 2-5. Schematic of EB-PVD deposition process; (a): Device illustrations; (b): Deposition process [82]. (Copyright permission, Elsevier)

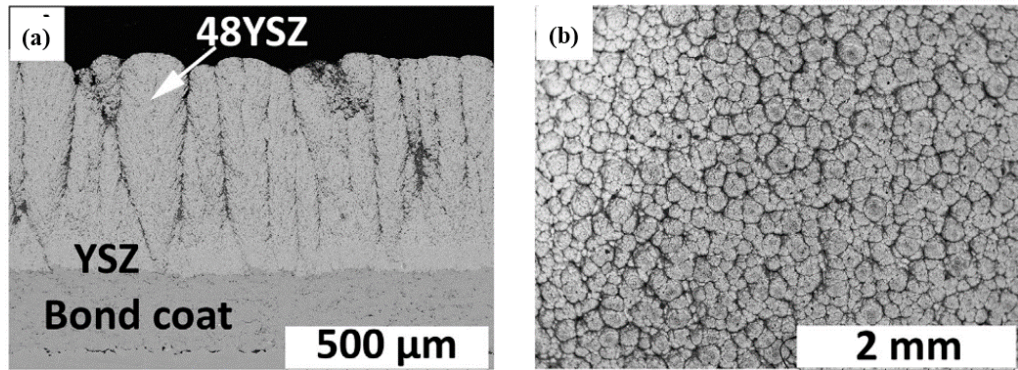


Figure 2-6. The (a) cross-sectional and (b) top view microstructure image of SPS deposited TBC coating[83]. (Copyright permission, Elsevier)

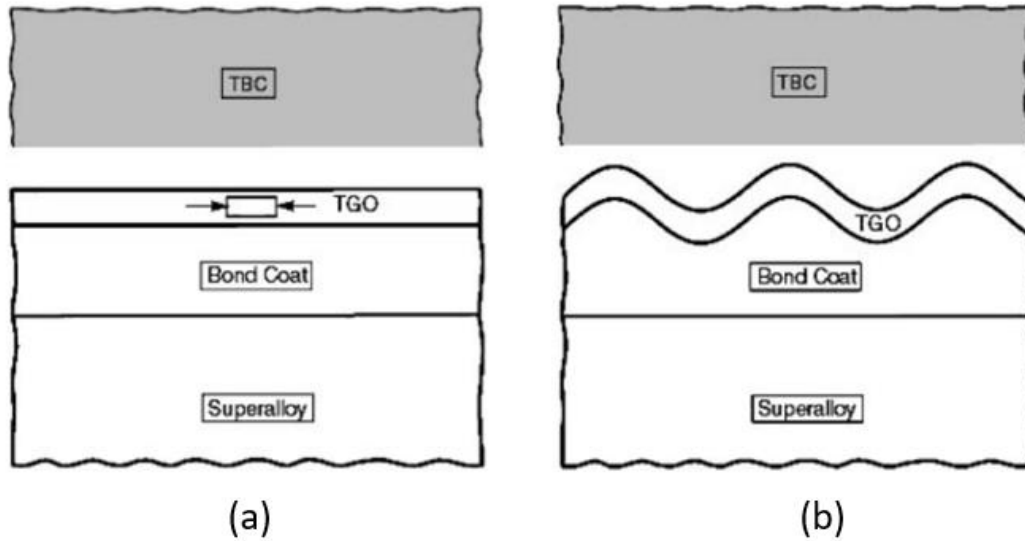


Figure 2-7. (a) The demonstration of the compressive stress at TGO, induced by the CTE difference between TGO and BC; (b) the interface will be deformed with the compression – relaxation cycle also called the “Ratchet Effect” [5] (Copyright permission, Annual Review, Inc.)

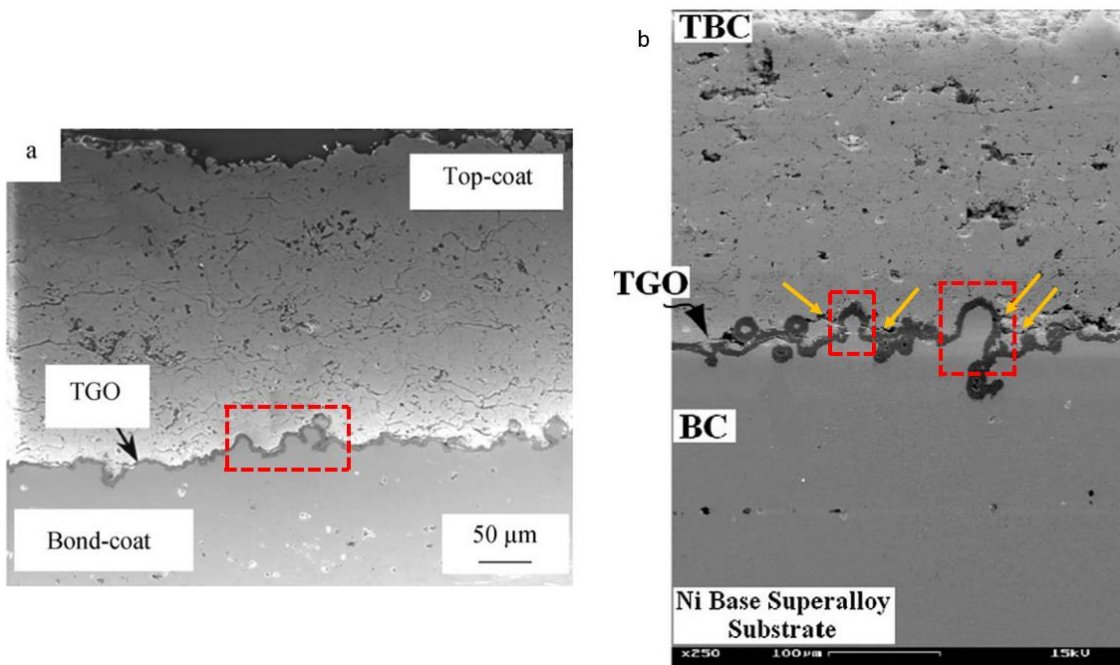


Figure 2-8. Cross-sectional SEM images at the interface of APS TBCs denote the interfacial roughness (red dotted box) and horizontal cracks (yellow arrows) [31], [32]. (Copyright permission, Springer Nature and Elsevier)

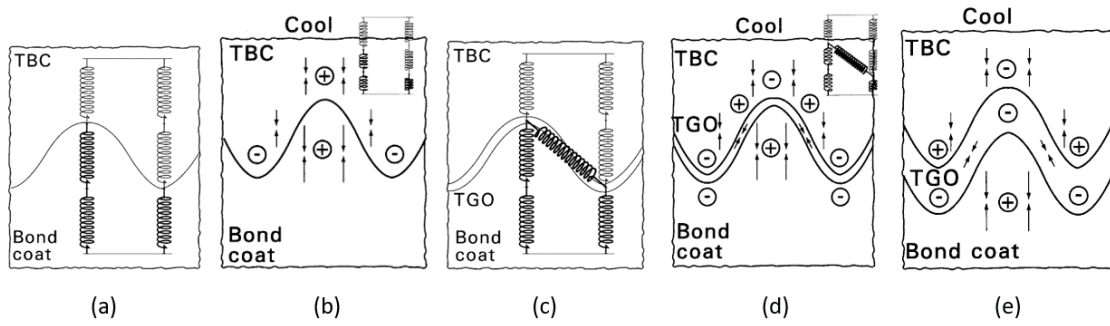


Figure 2-9. A simplified mechanical model near the TC/TGO/BC interface is represented by a group of springs and the stress distribution. The darker color spring denotes a higher spring constant, positive and negative signs denote tensile and compressive stress, and the length of the arrow marks denotes the contraction amount; (a) the spring model without TGO (b) stress distribution at cool-down period (c) the spring model with thin TGO; (d,e) stress distribution at cool-down period with the effect of TGO [29]. (Copyright permission, Elsevier)

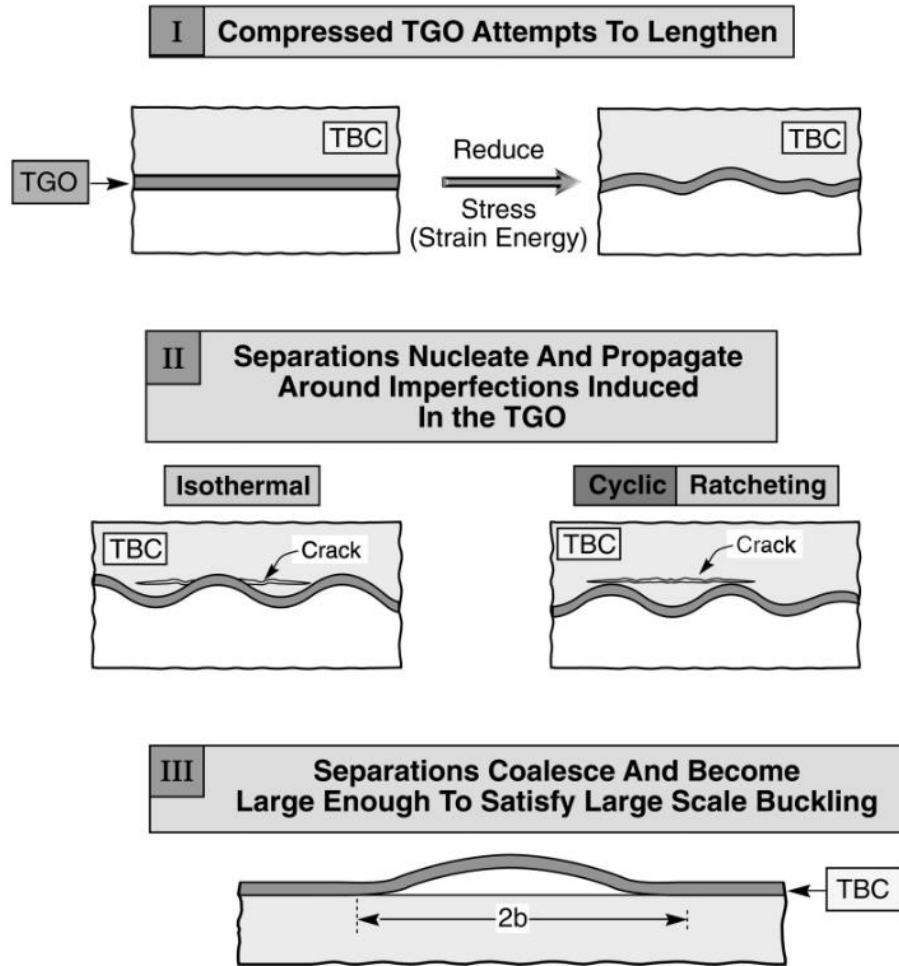


Figure 2-10. The spallation process of the thermal barrier coating. (I) Starting by undulating the bond-coat (BC); (II) then nucleate and propagate the cracks near the interface; (III) cracks coalesce and lead to the eventual spallation[34]. (Copyright permission, Elsevier Science & Technology Journals)

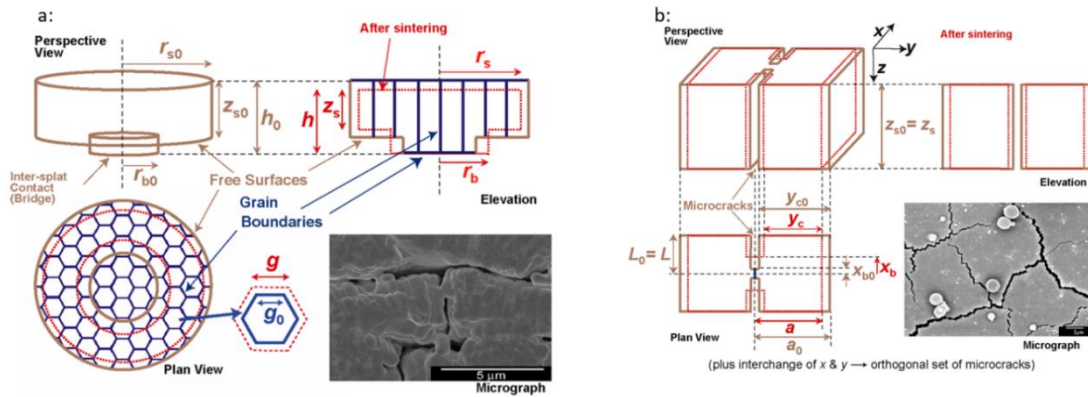


Figure 2-11. (a) Schematic diagram of Domain (1): inter-splat pores, demonstrated in perspective, elevation, and plan view; (b) Schematic diagram of Domain (2): intra-splat microcracks, demonstrated in perspective, elevation, and plan view. The dotted line is the shape of the model when it is fully sintered [41]. (Copyright permission, Elsevier)

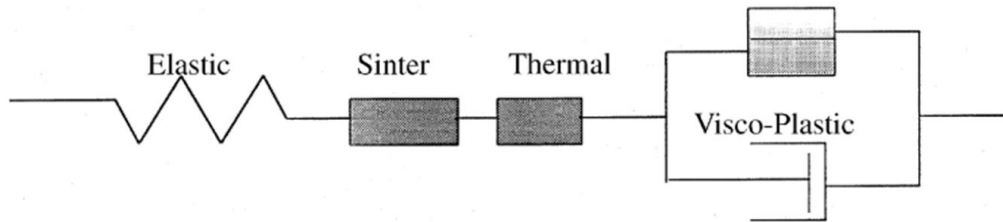


Figure 2-12. The thermal elasto-viscoplastic constitutive model for the sintering process [55]. (Copyright permission, Elsevier)

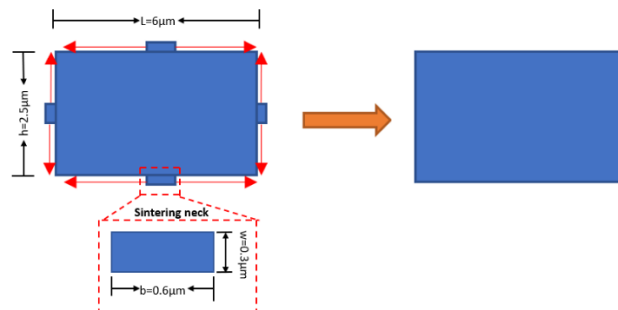


Figure 2-13. the sintering behavior of a periodic unit of grain in the coating. To reduce free energy, the neck's width will grow until it reaches the edge. The microcracks around the neck will be cured.

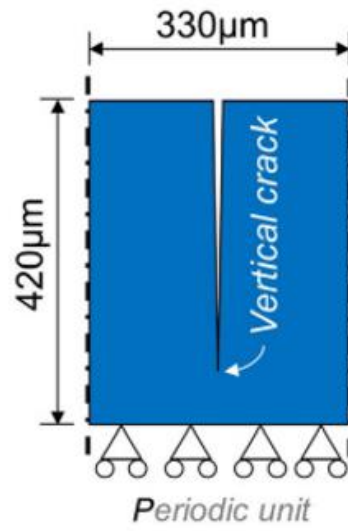


Figure 2-14. Periodic finite element for SPS -TBC with a long vertical crack. [54]. (Copyright permission, John Wiley and Sons)

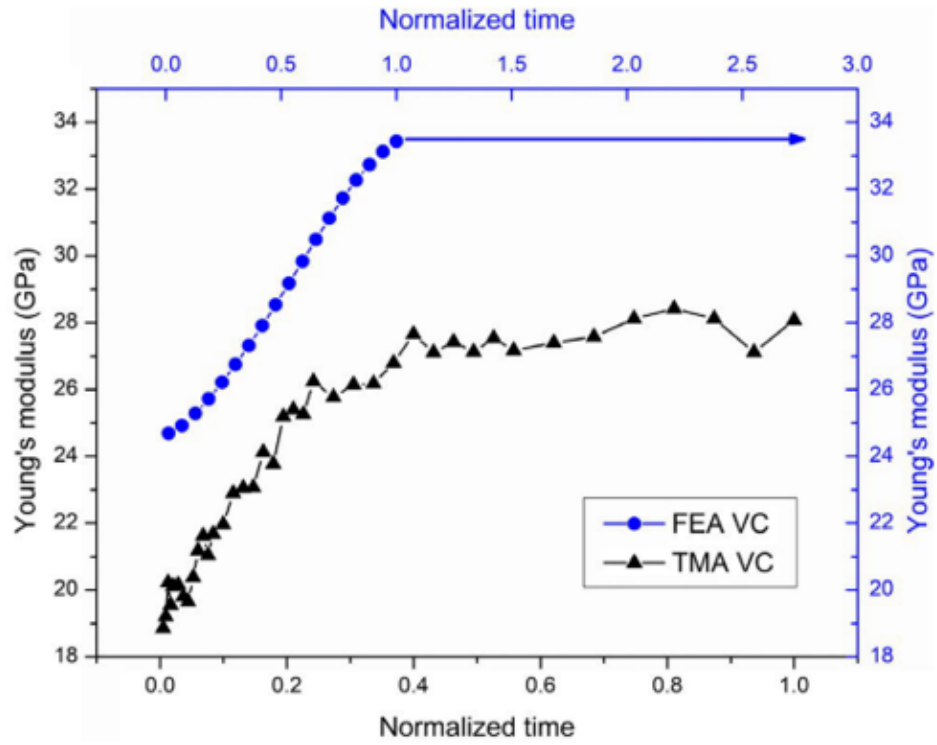


Figure 2-15. Comparison of FEA and experimental (TMA) results with the contribution of vertical crack (VC) [54]. (Copyright permission, John Wiley and Sons)

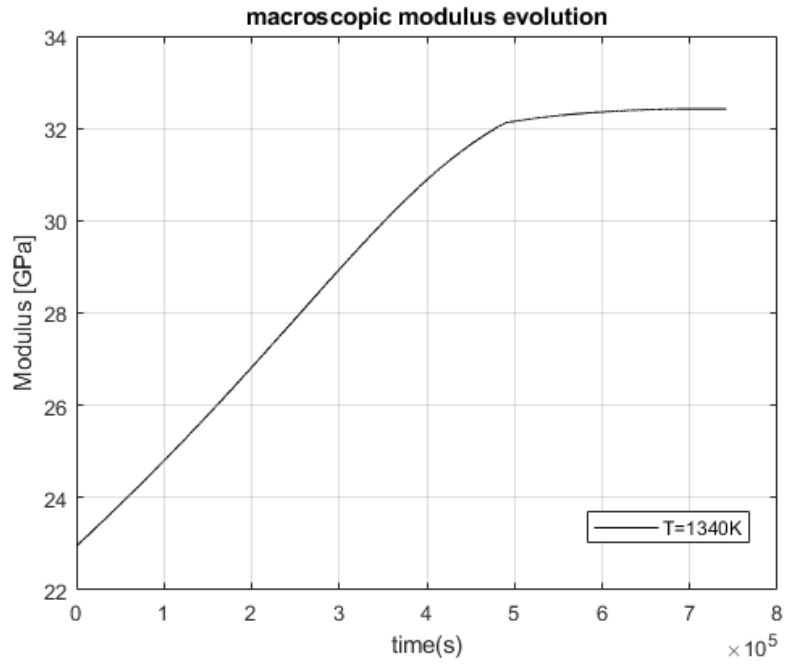


Figure 2-16. The macroscopic in-plane elastic modulus evolution for APS YSZ at the temperature of 1340K was simulated by the sintering model. (Calculated via the research of Lv et al. [54])

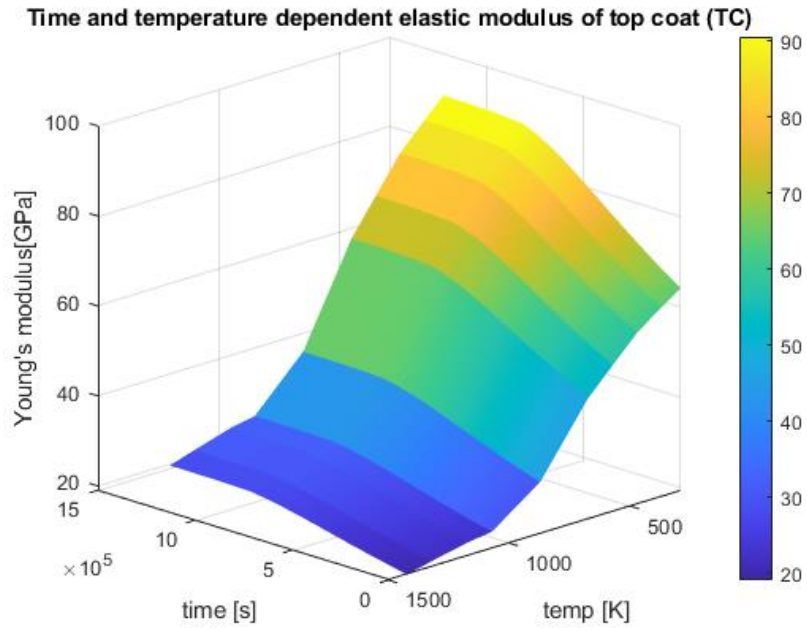


Figure 2-17. time and temperature-dependent elastic modulus surface plot for YSZ YC sintering at 1340 K. (Interpolated with the material data from Qi et al. [57])

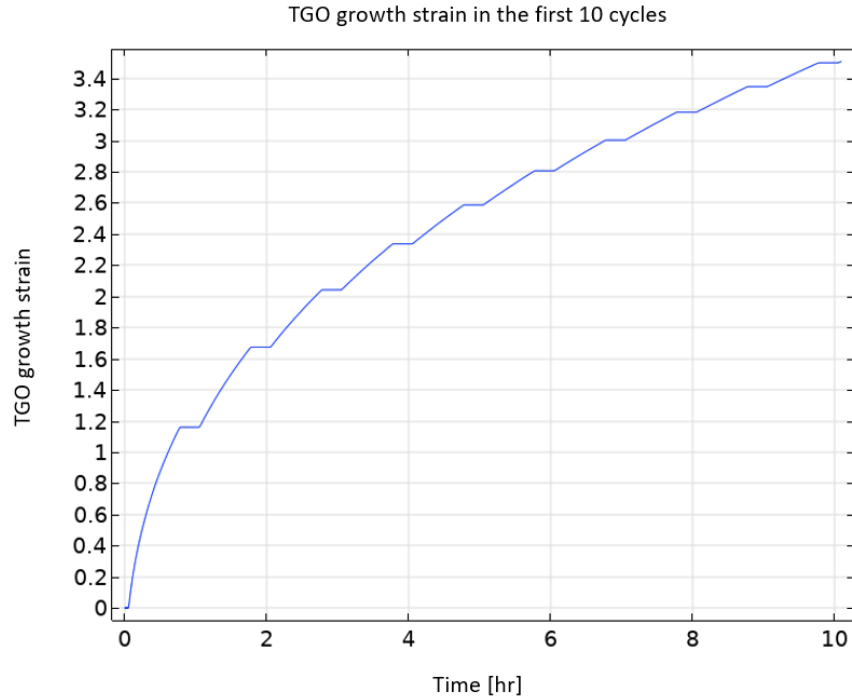


Figure 2-18. TGO growth strain over oxidation time in the first 10 cycles with Busso et al. model [58]. Growth pauses when it is cooled down and continues when it is fully heated.

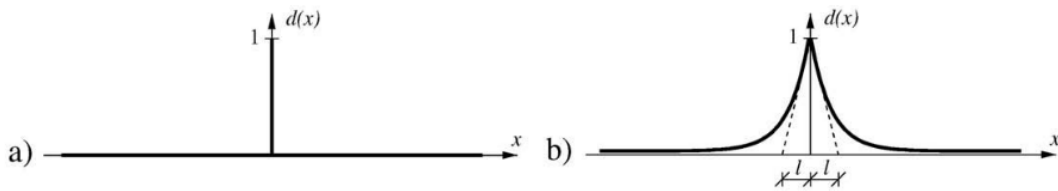


Figure 2-19. Crack topology of a bar that has a crack at $x = 0$; a) sharp crack at $x = 0$; b) diffusive crack at $x = 0$ with length scale l [77]. (Copyright permission, John Wiley and Sons)

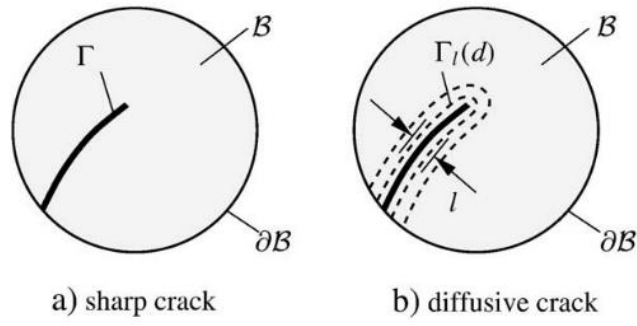


Figure 2-20. Crack topology embedded in a solid \mathcal{B} with a) sharp crack surface Γ and b) diffusive crack surface $\Gamma_l(d)$. The $\partial\mathcal{B}$ denotes the edge of the solid. [77]. (Copyright permission, John Wiley and Sons)

3. Stress analysis at the TC/TGO interface with multiple effects

This chapter studies the stress analysis simulation using the commercial software COMSOL Multiphysics vers.5.6. The simulations aim to determine the stress state on the coating's interface, with different parameters including the roughness shape, and TGO growth rate, thermal gradient, and the TC sintering.

The COMSOL Multiphysics software featuring the Multiphysics coupling is capable of coupling the solid mechanics model with heat transfer formulae. With COMSOL Multiphysics, a thermal gradient can be modeled across the thickness of the TBC – superalloy system, which is commonly set as isothermal in the previous research. Besides, the power-law creep model, sintering model, and the oxide growth model are well integrated within the software without many modifications.

The finite element model geometry, boundary condition, heat transfer model setup, and mesh design are outlined below, followed by the results and discussion of stress states given multiple variables.

3.1. FEM model setup, geometry, and boundary conditions

In our research, the interface is described by a sinusoidal curve with reference configuration: height $a = 10\mu m$ and wavelength $w = 24\mu m$. The geometry is close to the one used by [29]. The initial thickness of TGO $H_{TGO} = 1\mu m$ and it increases at each thermal cycle by switching the BC to TGO. The growth model was introduced in section 2.3.2.2. The initial thickness of a) TC = 250 μm ; b) BC = 130 μm ; c) substrate = 5mm.

Figure 3-1 shows the reference configuration of the FEM geometry with the boundary conditions.

For the boundary conditions, to save the computation power, only half the periodic unit is simulated, and another half uses symmetry boundary. A roller is applied to the bottom of the substrate to avoid stress concentration at the corners. Air pressure is applied to the top surface for realism. A prescribed displacement is applied to the right surface of the model to simulate the lateral thermal expansion in a periodic unit. It is close to the Multi-Point Constraint (MPC) in ABAQUS used in [31], [84]. The prescribed displacement is determined by the weighted CTE of each layer of material, the equation gives

$$\delta = \sum_{i=1}^n CTE_i * 12 [\mu m] * b_i [\mu m] / 5380 [\mu m] \quad (3.1)$$

where 12 μm is the width of the model, 5380 μm is the total thickness of the system, CTE is the coefficient of thermal expansion at each layer, and b_i is the thickness of each layer. The prescribed displacement is constrained by mesh elements and therefore, the thermal gradient can affect the prescribed displacement due to the thermal expansion strains vary through the thickness. In our case, the substrate dominates the thermal expansion in the in-plane direction and thermal stress (σ_{11}) will be induced during heating and cooling at each layer.

3.2. Heat transfer model setup

In the past, the temperature field applied in cyclic thermal loading failure analysis simulation of TBC is commonly isothermal and it is because the failure at the interface is

dominated by radial stress and the thermal gradient is difficult to realize in experimental conditions [6], [29], [46], [85]. But thermal gradient may play an important role in transient states and the CTE mismatch can also cause in-plane stress during heating and cooling periods. With these factors, it is valuable to discuss the thermal gradient case in our study.

Thermal gradient is adopted in our model with the benefit of the built-in Multiphysics feature of COMSOL software. For applications in aero-engine, the blades are not only protected by the TBC system, but also by the air cooling system. Figure 2-1 demonstrated the temperature gradient of the TBC system denoted with a yellow line. Air temperature firstly drops with cooling air film, then the TC will further decrease the temperature due to its low thermal conductivity. The total temperature drop with cooling air and TC is more than 200K. The temperature will slightly decrease at the metallic BC and substrate. The heat will be taken away with internal ducts that cooling air flows constantly. The air-cooling system is demonstrated in Figure 3-2. Cooling air bleeds from the high-pressure compressor, at the temperature of 873 K, then the air will flow through the internal duct, and carry the heat load from the superalloy. Finally, the air in the duct will bleed out by film cooling holes and generate a thin layer of air between hot gas and the coating surface, to maximize the cooling performance [3], [4], [86].

With the given information, the heat transfer model can be built in our geometry model. Figure 3-1 (b) demonstrates that the heat will be transferred from exterior hot gas with inward heat transfer coefficient h_{in} , then conducting through the layers of material, then dissipating with cooling air with cooling heat transfer coefficient h_{cool} . The side

walls of the periodic unit are set as insulated. The heat conduction within the model is governed by Fourier's law [87]:

$$\mathbf{q} = -k\nabla T \quad (3.2)$$

where \mathbf{q} is the local heat flux density in W/m^2 , k is the thermal conductivity in W/mK , and ∇T is the temperature gradient in K/m . The heat transfer from air to solid at the boundary is dominated by Newton's law of cooling:

$$q = -h\Delta T \quad (3.3)$$

where h is the heat transfer coefficient in W/m^2K and $\Delta T = T_1 - T_2$ is the temperature difference between the surrounding fluid and solid surface area. For the scenario of heat transfer by external forced convection, the inward heat transfer coefficient is governed by Eq. (3.4) [87]:

$$h_{in} = \left(\begin{array}{l} 2 \frac{k}{L} \frac{0.3387 Pr^{1/3} Re_L^{1/2}}{\left(1 + \left(\frac{0.0468}{P}\right)^{2/3}\right)^{1/4}} \quad \text{if } Re_L \leq 5 \cdot 10^5 \\ 2 \frac{k}{L} Pr^{1/3} (0.037 Re_L^{4/5} - 871) \quad \text{if } Re_L > 5 \cdot 10^5 \end{array} \right) \quad (3.4)$$

where $Pr = \mu C_p / k$ is Prantl's number and $Re_L = \rho UL / \mu$ is Reynolds' number, k is the air conductivity, L is the blade length, U is the airspeed, P is the external pressure, C_p is the air heat capacity and μ is the viscosity [87]. The governing equation is generally based on the airspeed U , blade length L , and external pressure P . For the h_{cool} at cooling duct, considering the complex internal structure (like ribs, fins), it is hard to express it as an equation. The experimental result read at $Re = 55000$, $h_{cool} = 420 W/m^2K$ [88]. For cooling air bleed from the compression stage, the temperature reads $T_{cool} = 650^\circ C$ [89].

Thermal properties of each layer are listed in Table 3-1 and the environmental inputs includes the airspeed U , blade length L , inlet pressure p , hot gas temperature T_{out} , and cooling air temperature T_{cool} are listed in Table 3-2. The thermal cycle applied in the simulation is shown in Figure 3-3, with both heat transfer input in red line and isothermal input in blue line. The length of each cycle is 3600s or 1 hour, with 3100s of heating and 500s of cooling period to ensure it is fully cooled down. The thermal cycles will repeat 30 times until the oxide grows to a certain thickness. The thermal gradient applied to the FEM model is shown in Figure 3-4. At the surface of TC, the temperature drops from 1323 K to 1313 K with the thin layer of stagnation airflow. Then the temperature rapidly drops to 1270 K at the TC/TGO interface due to the thermal barrier performance. The curve slope is then decreasing along the TGO, BC and substrate layer. At the bottom of substrate, the cooling air will carry out the heat energy with heat convection. For comparison, a parametric study will be conducted using the isothermal temperature field from TC surface to substrate bottom, to discover the difference in stress level.

3.3. Material properties

The material for all layers of the TBC system are defined as homogeneous and isotropic. Elastic modulus (E), Poisson's ratio (ν), and Thermal expansion coefficient (CTE) are temperature-dependent since our model runs at elevated temperature. The mechanical properties are listed in Table 3-3. The YSZ TC sinters during the thermal cycles, thus the elastic modulus of TC in Table 3-3 is only applicable at deposition. The evolution with time is introduced in section 2.3.2.1 and the time-temperature-dependent elastic modulus is shown in Figure 2-17. Table 3-4 defines the creep data obtained in the literature for the creep model please refer to section 2.3.2.3. Table 3-5 defines the inputs

for the TGO growth model obtained in the literature, and the temperature input is referred to the temperature at the TC/TGO interface. For the reference case, the input exterior temperature is 1323 K, and the temperature at the TC/TGO interface is about 1271 K according to the thermal gradient simulation result shown in Figure 3-4.

The material data are provided in multiple publications and comparisons were made to ensure the validity. However, the varying in manufacturing conditions, raw materials, and measurement methods can lead to a different result. Therefore, the simulation results need further validation by a proper test, which is not conducted in this thesis.

3.4. Mesh design

The mesh design for the TBC system is shown in Figure 3-5. In the 2D geometry, the quad element is selected for better precision and the total number of generalized plane strain elements is 5172. The mesh for the TGO layers that will switch from BC to TGO during the thermal cycles is refined with a mapping technique to ensure the resulting quality. The complexity at the stress requires higher order elements to ensure the result quality. Therefore, quadratic quad element (8-nodes) is selected for displacement field and linear quad element (4-nodes) is selected for heat transfer field (See Figure 3-6) and it later proved in the convergence test in 3.6.1. In COMSOL Multiphysics, the displacement field and heat transfer field will be solved separately with the segregated approach. The segregated solver divides the problems into two steps then solve the unknowns individually. These steps are smaller than the fully-coupled approach and requires less memory [65], [87].

3.5. Parametric study plans

The parametric study cases are focused on different TGO growth rates, different roughness aspect ratios, sintering effects, and isothermal effects. The detail study configurations and the case number are listed in Table 3-6.

3.6. Results

The stress states during the 30 thermal cycles were examined in the simulation. This study mainly focuses on the radial stress (σ_{22}), in-plane stress (σ_{11}), and first principal stress (σ_1) represented by Cauchy stress tensors, which are components potentially leads to horizontal and vertical crack propagation. The definition of first principal stress is defined as $\sigma_1 = \frac{\sigma_{11} + \sigma_{22}}{2} + \sqrt{\left(\frac{\sigma_{11} - \sigma_{22}}{2}\right)^2 + \tau_{12}^2}$ [90]. A convergence test is presented below, followed by the parametric study of TGO thickness, interfacial roughness aspect ratio, and sintering. Figure 3-7 shows the positions of the results that will be discussed. All the sampling points are 0.1 μm above the interface, guided by the interface curve.

3.6.1. Convergence test

A convergence analysis was performed at the end of the first thermal cycle. The maximum radial stress and the maximum principal stress at the TGO were selected to study, which is because the stress pattern at the mid-layer has the most complexity. At initial, the mesh is coarse, then the refinement is done by selecting higher order elements and reducing the element size. Figure 3-8 shows the maximum stress values in the coating versus the number of degrees of freedom (NDOF) of the model. The results read

when the NDOF is higher than 2×10^5 , the stress results are stable at a certain magnitude, which means that the mesh is converged.

3.6.2. Reference case

The reference case (I) time-dependent study results are shown in Figure 3-9, Figure 3-10, and Figure 3-11, respectively. The plots demonstrate the first principal stress, radial stress (σ_{22}), and in-plane stress (σ_{11}) along the off-peak and off-valley position during the 30 hours thermal cycles. For a better readability, at every cycle, the stress decreases to a low level when it is heated and held; once it cools down, the thermal mismatch then induces residual stress to the high level, then the process repeats at the next cycle.

The stress pattern at the off-peak and off-valley locations show a different trend. At the off-peak position, the first principal stress is in a always tensile state. The stress level increases in the first two cycles to about 220 MPa then gradually decreases to 140 MPa, then hold steady in the last 10 cycles. For the stress during heating, the stress level decreases from 50 MPa to 0 MPa is mainly the result of creep relaxation. At the off-valley position, the first principal stress is in compressive state in the first 10 cycles, then turn to tensile state and progressively grow in the next 20 cycles, to about 80 MPa. Compared to the stress at the off-peak, the off-valley stress level is always lower, which means the initial cracks located near the peak have a greater threat to propagate. However, it is necessary to determine the component stresses (radial and in-plane stress) to know how cracks propagate.

For the radial stress, the maximum radial stress at the off-peak position happens in the first cycle, at about 140 MPa, then rapidly decrease in the first 15 cycles. It is mostly

affected by the rapid growth of TGO, then secondly relaxed by the creep relaxation. As mentioned above, the most common cracks in APS method coatings are horizontal cracks. The large σ_{22} in the first few cycles is a threat to crack propagation. But the threat is relieved as TGO thickens. At the off-valley, the radial stress shows a negative trend to the off-peak position. The σ_{22} becomes tensile after cycle #14 and goes up to 60 MPa when TGO thickness is 5.4 μm , then becomes the major location for crack nucleation and propagation.

For the in-plane stress in Figure 3-11, the trend for both off-peak and off-valley positions is more homogeneous. As mentioned, the TGO and TC have the lowest CTE in the TBC system, therefore, in the in-plane direction, TC is being stretched during the first thermal cycle, and the maximum in-plane stress is about 80 MPa. With the creep relaxation, the stress level reduces to a much lower level, then when it is cooled down, the substrate and bond coat shrinks more than compressing the TC and TGO. Therefore, the only chance for vertical crack propagation in TC is during the heat-up of the first cycles.

The stress distribution surface plots at the end of the cycle periods are shown in Figure 3-12 and Figure 3-13. There is more information included in these surface plots. In the radial stress (σ_{22}) plots, Figure 3-12 shows that the center of stress concentration moves along the roughness, from the off-peak to the middle of the valley. Figure 3-13 shows that the first principal stress has the same trend of stress concentration move but in the first few cycles the stress center is located at the peak position instead of off-peak. It is notable that the magnitude of σ_{22} is even increase, from 165 to 183 MPa, when the TGO is thickened. However, it could be the result of sintering of TC. The parametric

study case (VII) can answer the question. The in-plane stress (σ_{11}) is not plotted here, since it is compressive at every cycle, did not show any potential of vertical crack propagation.

For the concern of crack propagation, the cracks located at the mid-level are potential to propagate as TGO thickness increases. It is doubted that if TGO continues to grow, the stress concentration will continue moving down and the magnitude increases. This will be discussed in the parametric study of TGO growth rate (see case (II, III)).

3.6.3. Parametric study results of TGO growth rate

In this parametric study for case II and III, the configuration is listed in Table 3-6. The comparison plots of the first principal stress, radial stress (σ_{22}) at off-peak and off-valley position is shown in Figure 3-14 to Figure 3-17. The stress distribution plot at different thermal cycles for each case is shown in Figure 3-18 to Figure 3-21. And the comparison of maximum principal stress and maximum radial stress at the whole TC is shown in Figure 3-22 and Figure 3-23.

As shown in Figure 3-14, the first principal stress at the off-peak shows a similar trend at all TGO growth rates. For case III with the fastest TGO growth, the stress at cycle 2 is only 10 MPa higher than the reference case, and case II is about 20 MPa lower than the reference case at 220 MPa. After cycle 10, all cases have a similar magnitude of first principal stress, at around 150 MPa. But at the off-valley position, the effect from TGO thickness makes the difference, as shown in Figure 3-15. For the reference case the first principal stress is compressive during the cool-down period of the first 10 cycles, then progressively becomes tensile and increases magnitude with oxidation. In case III, as

the TGO thickens, the maximum tensile stress observed at cycle 30, is high as 170 MPa, which has a TGO thickness of almost 10 μ m.

For radial stress σ_{22} , Figure 3-16 and Figure 3-17 show that the TGO thickness is the main factor that affects the stress state. As TGO thickness increases, σ_{22} at off-peak becomes compressive and the stress at the off-valley changes to tensile. The maximum magnitude of σ_{22} at off-peak and off-valley is similar, at about 160 MPa. As a component of the first principal stress, the σ_{22} distribution can illustrate that for horizontal cracks near the peak position, it has a potential to propagate when the TGO thickness is small, or at the early stage of service; for cracks near the valley, it is more potential to propagate at the later stage of service.

For the stress distribution over the TC, in the reference case (I), it shows that the location of maximum stress moves down with the TGO thickness increase. Both σ_{22} and σ_1 has the same trend. Figure 3-20 and Figure 3-21 prove that with further increase of TGO thickness, the stress concentration center will continue to move the valley, and the magnitude is even higher, which matches the results in Figure 3-15 and Figure 3-17. Since the stress center moves with time, it is necessary to compare the maximum stress on the TC, and the results are in Figure 3-22 and Figure 3-23. Notably, Case III with the fastest TGO growth rate has the highest principal at every cycle. The highest stress happened in cycle 1 at 300 – 350 MPa, each case has a trend of decrease in the first 10 cycles which is caused by the creep relaxation. The stress continues to decrease until cycle 10, then gradually increases to 200 MPa, which is governed by the sintering and the stress center. Again, the compare plots for σ_{11} are not included here since it is compressive at every cycle.

3.6.4. Parametric study result of the roughness geometry aspect ratio

In this parametric study, the aspect ratio (AR) of the interfacial roughness is between 5/24 to 20/24. The configurations for cases IV, V, and VI are listed in Table 3-6. The radial stress σ_{22} , first principal stress (σ_1) plots at off-peak and off-valley positions are shown in Figure 3-24 to Figure 3-27. The plots of the maximum of first principal stress (σ_1) and maximum (σ_{22}) over the whole area of TC is in Figure 3-28 and Figure 3-29.

For the radial stress σ_{22} at the off-peak, Figure 3-24 compares the stress trend with different ARs. In the reference case I, the σ_{22} is the highest at the end of cycle 1, at 140 MPa, then gradually drop to negative. For case IV with a flatter roughness, the σ_{22} is tensile in cycle 1, then rapidly turn into compressive, at the highest magnitude in compression stress within these cases. Case V and VI with a steeper interface, show a similar trend to each other, but their stress relaxing is much slower than the reference case I. At cycle 30, case VI still has the σ_{22} at 100 MPa. When looking into Figure 3-26, the trends can explain the behaviors. At off-valley, the case IV with a flatter interface rapidly builds up the tensile stress and finally, it reaches about 150 MPa. Case V and VI with high AR are always compressive in the 30 thermal cycles. In section 3.6.3, it mentions that as the TGO thickness increases, the load is more transferred to the TGO. The low CTE of TGO stretches the TC vertically, and the stress at the valley then becomes tensile state. But in case V and VI, the stress at the valley is still compressive. It proves that at the steeper roughness, the TGO thickness is less affecting the stress state at the TC.

For the first principal stress at the off-peak in Figure 3-25, all cases have similar trends over the cycles. Case IV with the flattest roughness always has the least tensile stress during the thermal cycles, and it is apparently because it has the least thermal mismatch strain in radial direction, but for case V and VI with steeper roughness, the maximum stress is even lower than the reference case. It looks unusual since the steep roughness has the largest thermal mismatch. After reviewing Figure 3-28 and the stress contours, case VI still has the highest first principal stress at about 460 MPa in cycle 1 but it is located at the peak position. This result reads the stress is more concentrated at the peak position as the AR increases. After 15 thermal cycles, the trend is flattened, and the stress level reaches the plateau. For the first principal stress at off-valley in Figure 3-27, the trends are more similar to the σ_{22} in Figure 3-26, where the stress in reference case gradually moves from negative to positive; the cases with lower AR moves faster, and vice versa.

The results of maximum stress in the whole area of TC are given in Figure 3-28 and Figure 3-29. In the last paragraph, the maximum of the first principal stress is discussed that the steeper roughness case always has a higher stress level in the first few cycles. The figure also displays that after 10 to 15 thermal cycles, the maximum stress level is similar for each case. The slight increase from cycle 15 to 30 is caused by the sintering effects of TC. For maximum radial stress in Figure 3-29, results read that the stress in case VI has the highest maximum radial stress at cycle 1, then reaches the plateau at 150 MPa after cycle 10. Case V and reference case I have a similar result. But the case IV with the flattest interface continuously increases the stress level from cycle 1, and finally the σ_{22} can reaches 150 MPa at the valley, like other cases.

Based on the observations in the figures, it concludes that a) the tensile stress center for all cases gradually moves from the peak to the valley; b) for higher AR, the stress pattern is less affected by the TGO thickness; c) for higher AR, the maximum stress is higher, but they become similar after the creep relaxation of initial stress and TGO growth. Concerning the potential of crack propagation in TC, the parametric study can learn that a) with higher AR, the horizontal cracks are much easier to propagate near the roughness peak, but the crack near the valley is barely affected. It is because the stress pattern is less affected by the TGO growth, then the radial stress is always compressive near the valley. c) for cases with lower AR, the crack near the peak is worry-free, since it is radial stress is compressive at almost every cycle. but the crack near the valley has the potential for propagation in the later thermal cycles, since the σ_{22} is increased to the 170 MPa, which is only 35 MPa lower than case VI, and even higher than the σ_{22} in case I at cycle 1.

3.6.5. Parametric study results of TC sintering

In the reference case, the sintering model is coupled with the material model. At ambient temperature, the elastic modulus will stiffen from 60 GPa to about 90GPa. This parametric study will investigate how much it affects the stress level. In Figure 3-30 and Figure 3-31, the radial stress and principal stress comparison plots are shown. Figure 3-32 and Figure 3-33 show the maximum radial stress and first principal stress at the TC.

In Figure 3-30, for the comparisons at off-peak, the results show the stress level gap between the two groups is minor. In cycle 1, the stress difference is about 3% while In cycle 30, the stress in case I is about 25% higher than the stress in case VII, proving that the model works. Compared to the 50% gain for elastic modulus, the modulus

difference at cycle 30 is much less than 50%. It can easily explain that the stiffening of TC will transfer the loads to TGO. For the off-valley results, first principal stress results, the trend is always the same: the reference case is about 25% higher than the case without the sintering model. Also, the sintering model is unable to affect the stress distribution in the model since it is dominated by TGO growth and the shape of the interfacial roughness. But the stress increase at the latter stage is a significant factor causing the failure. For example, in Figure 3-32, the σ_{22} for case I is even higher than the σ_{22} for no sintering case in cycle 1. At cycle 30, the maximum stress is located at the mid-level, so it may be a threat to cracks located at the mid-level.

Therefore, the parametric study can prove that the sintering model is strongly affecting the stress magnitude and it is a significant factor that shortens the lifespan of the coating. Also, it is necessary to apply the sintering model in the failure estimation model, since it is the main factor of stress evolution at late cycles.

3.6.6. Parametric study of isothermal model

The results for case VIII: isothermal and the comparison plots with the reference case I are shown in Figure 3-34 and Figure 3-35. In the literature review, the purpose of coupling the heat transfer model is to simulate how thermal gradient affects the stress states at the interface area.

In Figure 3-34, the σ_{22} results for same position are very close to each other. Zoom-in plots indicate that the gap of stress during the cool-down between case I and case VIII is less than 1% at each cycle. The principal stress results in Figure 3-35 have a similar trend. Also, for the isothermal cases, noise is detected in the line plots. It is because the software is unable to detect the sudden change of temperature when heating

or cooling starts, but the stress result at the steady temperature is the same as in the reference case.

The opinion that the isothermal model unable to correctly reflect the σ_{11} since the CTE is temperature dependent, is unable to be proven here. It is because after the cool-down, the thermal gradient is minimized, and the stress data for comparison are at the cool-down period. Also, the opinion in the literature review is that the process of sintering is different through the thickness: at the surface suffers the highest temperature will sinter faster, and vice versa. The top of TC is stiffer and the σ_{11} pattern may change with it. It is unable to combine in this model since the elastic modulus in the mesh cannot define pointwise. All the elements in the material sinters at the same pace. For future studies, it is expected to have a better way to simulate the sintering effect more precisely. At current, the isothermal model is a more economical option to simulate the temperature field.

3.7. Discussions

In the reference case I, the radial stress σ_{22} at off-peak position shows a trend of decreasing from 140 MPa to about -20 MPa in compression, and the σ_{22} at off-valley is from -100 MPa to 60 MPa (see Figure 3-10). The trend of the stress distribution is mostly caused by the growth of TGO to shift the stress patterns. The stress contour of σ_{22} in Figure 3-12 shows a clearer view about how the stress distribution change as TGO grows. The maximum σ_{22} initially located at the off-peak at cycle#1 then progressively moves to the mid-level at cycle#30. The stress at off-valley initially is compressive at cycle#1 and gradually becomes tensile at the final stage of the thermal cycles. The contour results match the line plots in Figure 3-10. These stress trends when TGO grows progressively

are similar to the research results by Baker et al. and Jiang et al. [16], [63]. Additionally, the maximum σ_{22} in the Figure 3-12 (f) is even higher than the maximum σ_{22} in the Figure 3-12 (a) by ~ 20 MPa. It is mainly caused by the sintering of TC. When comparing the parametric study case VII with no sintering model implemented, Figure 3-32 shows that the maximum σ_{22} is about 140 MPa at cycle#30, which is 20 MPa less than the maximum σ_{22} in cycle #1 and 40 MPa less than the maximum σ_{22} in cycle#30 of case I. This stress behavior increases its potential of crack propagation in the later stage of heat cycles, near the valley position. For the sintering effect, Kyaw et al. [46] compared the radial stress σ_{22} of along the interface with and without the sintering model when the thermal cycles end. The result shows the same stress pattern (compressive at the peak and tensile at the valley) and the stress level increases by 40% with the fully sintered TC. The trend of their study matches our parametric study result in section 3.6.5. Ranjbar-Far et al. [31] coupled the creep, TGO growth model into the TBC model and simulated the stress distribution with different sinusoidal interface AR. Their results only compared the radial stress σ_{22} when $H_{TGO} = 5 \mu m$, which equivalent to the cycle#20 in our model. The maximum tensile σ_{22} is slightly increase from 50 MPa to 70 MPa when AR grows from 5/60 to 30/60. In our simulation, the maximum σ_{22} for all time range is plotted in Figure 3-29. The plots for case I,IV,V,VI (AR 5/24 to 20/24) (see Figure 3-29) showed the maximum σ_{22} for all cases varies at the early stage of thermal cycles and the maximum σ_{22} are similar after 20 hours of thermal cycles. The results match the simulation by Ranjbar-Far et al. [31] and this results demonstrate the roughness AR only affect the stress level at early stage and they become similar in the later stage. In our best knowledge, the heat transfer model is a brand-new feature for TBC stress simulation and

no literature proves its validity. However, the similarity of stress trend and stress level between the isothermal model (less than 1% difference) proves the validity of the heat transfer model (see Figure 3-34 and Figure 3-35).

Most former research has only discussed the σ_{22} in their results (the literatures in the last paragraph) since the σ_{22} is the main driving force of horizontal crack propagation. The first principal stress σ_1 plots in this chapter are aiming to give an estimation of crack propagation, since the principal stresses are the crack propagation criteria used in Chapter 4: Phase field damage model. The principal plane is independent at each node in the FEA model, thus the contour plot and line plot result are unable to estimate the crack propagation direction. But it can estimate the location of crack that will propagate. The crack direction can be estimated collaborating the plots of σ_{22} since it is a component in σ_1 . Based on the contour in Figure 3-13, the cracks near the peak and off-peak are are potential to propagate at the first 5 cycles, since the maximum σ_1 is near the peak position in the first few cycles. In the later stage, the stress level is reduced and the maximum σ_1 is moving to mid-level. The cracks near the mid-level and valley are more potential to propagate at the later stage. Comparing the contour for parametric study case II, III in Figure 3-19 and Figure 3-21, when the H_{TGO} grows faster, the maximum σ_1 moves faster to the valley, shows similar trend to the σ_{22} contours. Also, when TGO is grown to $10 \mu m$ (see Figure 3-21 (f) and Figure 3-22), the maximum σ_1 is increase again, which means the potential of crack propagation is gained again when H_{TGO} is $> 8 \mu m$.

The crack propagation is now only limited in the TC. Caliez et al. [91] observed that the cracks are potential to propagate through the TGO and BC in thermal cycle. In Figure 3-12, the σ_{22} near the peak of TGO and BC is strongly tensile. The tensile stress is

not relaxed with TGO growth, and this is a potential site for TGO-BC delamination. Zhou et al. [60] used phase field damage model to simulate the crack propagation at the TGO-BC interface and the results showed the TGO crack propagate along the interface and the crack stops propagates at the mid-level. In the future, the crack propagation through multiple layers should be discussed.

3.8. Summary

In this set of stress analysis studies at the interface, the stress state with multiple parameters is simulated, including different TGO growth rates, different interface geometry, sintering model, and isothermal model. Briefly, section 3.6.3 determines that the increased TGO growth rate will accelerate the location of maximum tensile stress moving to the valley, in other words, the cracks at the valley will become the potential to grow when TGO is thicker than 6 μm . When the TGO is thin, the main threat to the coating's life is the crack near the peak since stress is intensive in this region. In section 3.6.4, the parametric study determines that the steeper roughness will accumulate more stress than the reference case due to the more thermal mismatch strain at roughness, but the stress distribution is less affected by the TGO growth due to the competition between TGO and geometry effect. It means with steeper roughness, the threat to the cracks located at the peak is stronger. With a flatter interface, the threat to the crack at the valley is stronger. For the join of sintering model, section 3.6.5 determines that the sintering model is strongly affecting the stress level at the latter stage of life, which is a factor that shortens the life of the coatings, but the sintering model is unable to affect the stress pattern since that is dominated by the geometry. In terms of the isothermal model, the results in section 3.6.6 show that it barely affects the result, but the current model

underestimates the effect of different sintering paces with the thermal gradient, which should be further investigated when the sintering model can be better coupled by the simulation. The simulation results help us better estimate the coating failure and it will be used in Chapter 4, to help us determine the crack's locations by observing the stress state and comparing the stress states results with and without the cracks.

Table 3-1. Thermal properties of Substrate, BC, TGO, and TC[8], [92]–[98].

	Substrate	BC	TGO	TC
Conductivity, k [W/mK]	0.9	15.5	15.1	80
Heat capacity, C_p [J/kgK]	650	880	610	460
Density, ρ [kg/m ³]	6000	3970	7500	8700

Table 3-2. Aero engine operating environment [96], [99]

Airspeed, U	488 [m/s]
Blade length, L	0.2 [m]
Inlet pressure, p	35 [bar]
Cooling air temperature, T_{cool}	923 [K]
Hot gas temperature, T_{out}	1273 – 1573 [K]

Table 3-3. Temperature-dependent material properties for all layers of the TBC system.

T [°C]	T [K]	E [GPa]	ν	$\alpha \times 10^{-6}$ [1/K]
Substrate (CMSX-4 superalloy) [64]				
20	293	123	0.359	12.0
220	493	116	0.365	12.1
420	693	108	0.370	12.5
620	893	100	0.374	13.4
820	1093	92	0.378	14.7
1020	1293	85	0.380	15.8
BC (NiCoCrAlY) [64]				
20	293	152	0.319	12.3
220	493	151	0.327	13.0
420	693	145	0.334	13.9
620	893	132	0.341	14.9
820	1093	109	0.346	16.2
1020	1293	72	0.351	17.6
TGO (Al ₂ O ₃) [68]				
28	301	400	0.23	8.2
400	673	390	0.23	8.4
650	923	380	0.24	8.7
850	1123	355	0.25	9.0
980	1253	325	0.25	9.3
1100	1373	320	0.25	9.6
TC (APS YSZ) [57], [64], [68]				
20	293	62.5	-	9.68
28	301	-	0.10	-
100	373	59.6	-	-
200	473	55.7	0.10	-
220	493	-	-	9.67
300	573	50.3	0.10	-
400	673	44.9	0.10	-
420	693	-	-	9.71
600	873	29.8	0.10	-
620	893	-	-	9.81
650	923	-	0.11	-
800	1073	22.2	0.11	-
820	1093	-	-	10.02
900	1173	21.5	-	-
980	1253	-	0.12	-
1020	1293	-	-	10.04
1050	1323	19.8	0.12	-
1150	1423	18.6	0.12	-

Table 3-4. Creep data for TC, BC, and TGO [29], [63]

	BC	TGO	TC
Creep exponent n	3.0	1.0	1.0
Creep rate coefficient (1273 K) (s^{-1}) A_{nor}	1.39×10^{-7}	7.3×10^{-7}	9×10^{-9}
Creep rate coefficient (1423 K) (s^{-1}) A_{nor}	2.35×10^{-6}	-	-

Table 3-5. TGO growth equation inputs [58]

A_0	$1 \mu m/s$
m	0.332
Q_0	$76.7 kJ/mol$
R	$8.314 J/molK$
T_{ref}	2424 K

Table 3-6. Parametric study configurations and case number

Case	#	Thermal gradient	TGO growth	Aspect ratio	Sintering
Reference	I	✓	✓	10/24	✓
0.5x TGO growth	II	✓	0.5x	10/24	✓
1.5x TGO growth	III	✓	1.5x	10/24	✓
Roughness AR 5/24	IV	✓	✓	5/24	✓
Roughness AR 15/24	V	✓	✓	15/24	✓
Roughness AR 20/24	VI	✓	✓	20/24	✓
No sintering	VII	✓	✓	10/24	✗
Isothermal	VIII	✗	✓	10/24	✓

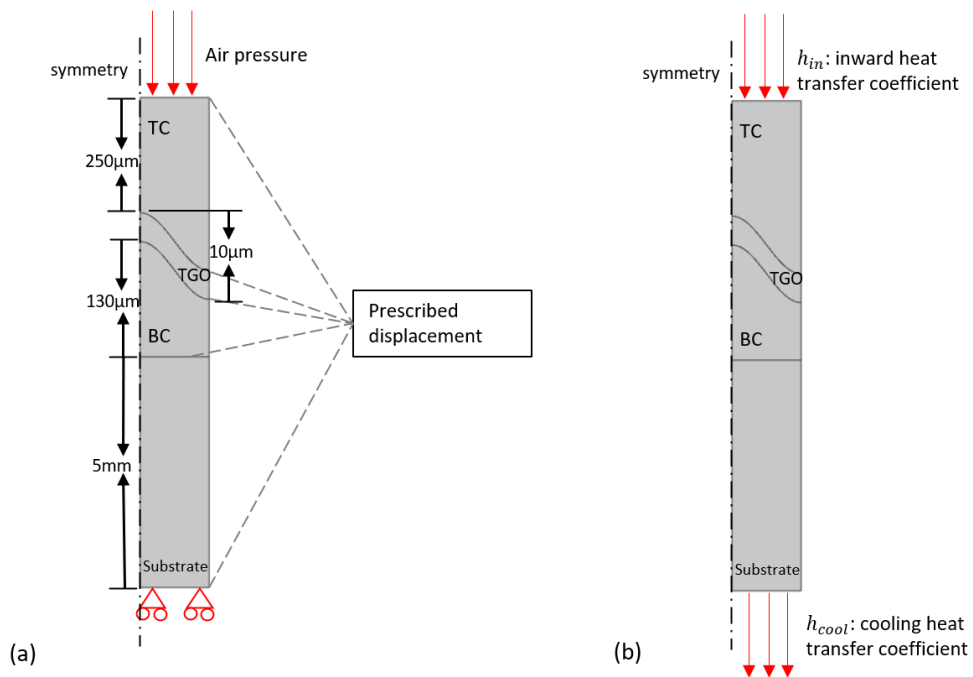


Figure 3-1. (a) The periodic unit of a TBC system applies in FEM simulation and structural mechanics boundary conditions (b) the thermal boundary conditions.

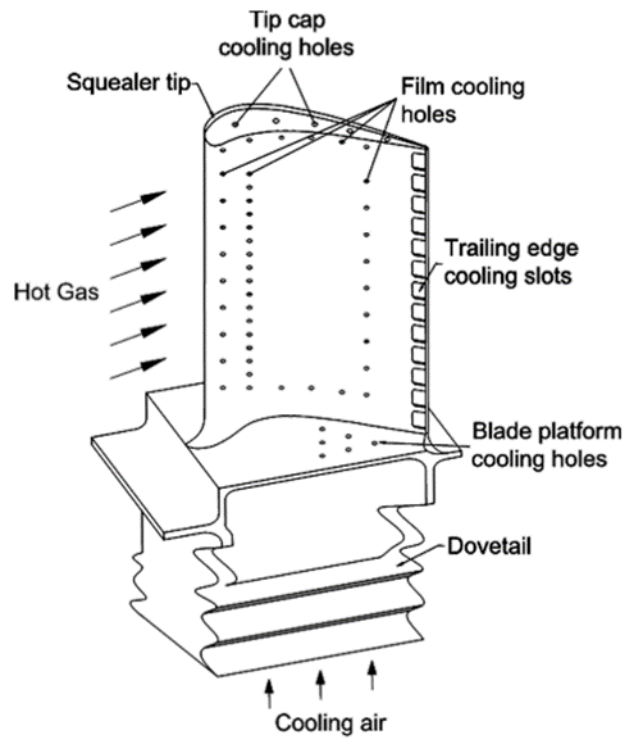


Figure 3-2. The schematic of a common turbine blade with cooling functions. The internal ducts are built with ribs to improve the heat transfer coefficient [3].

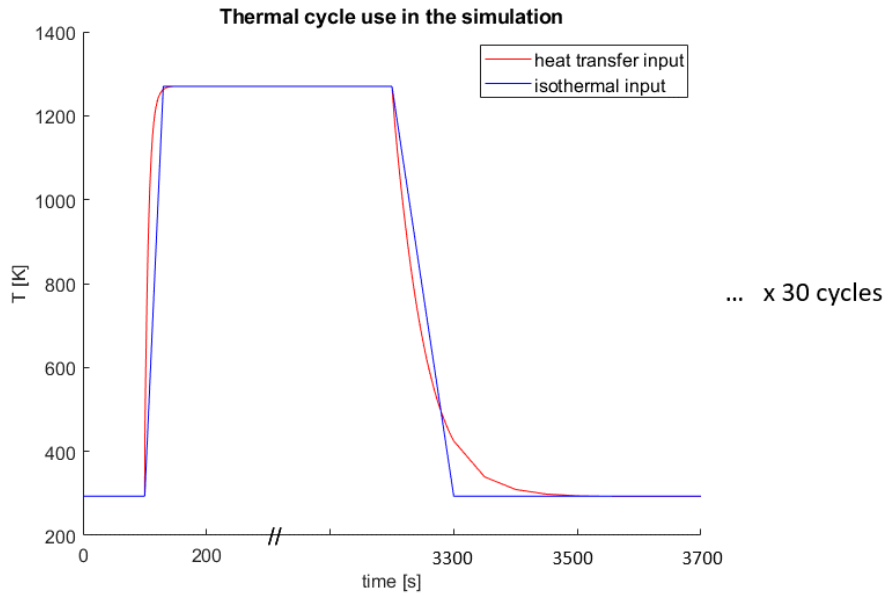


Figure 3-3. thermal cycle applied in the simulation (red: with heat transfer input; blue: with isothermal input)

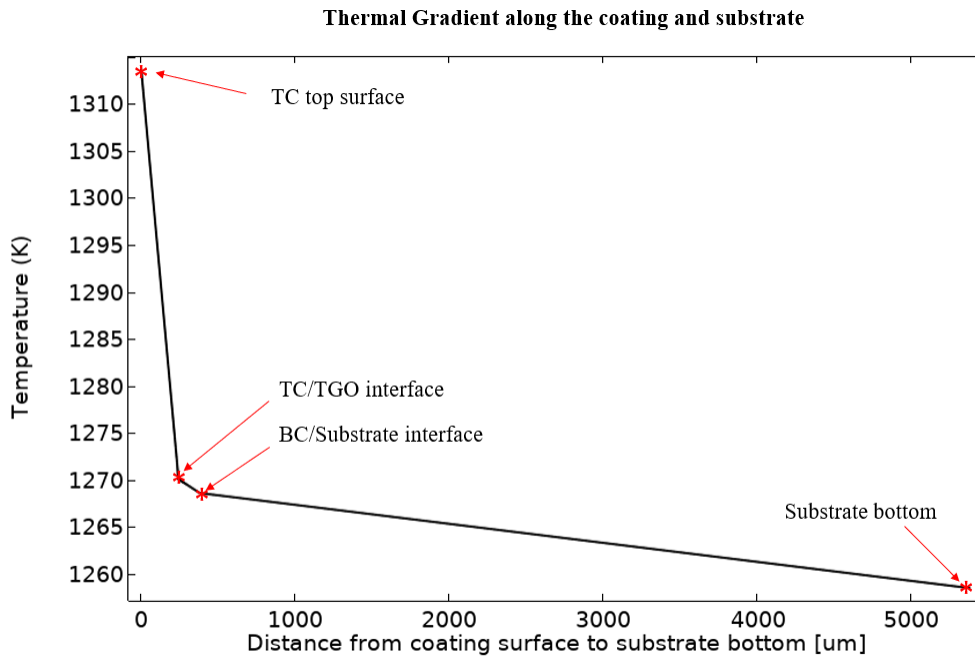


Figure 3-4. Thermal gradient along the TBC and substrate at elevated temperature

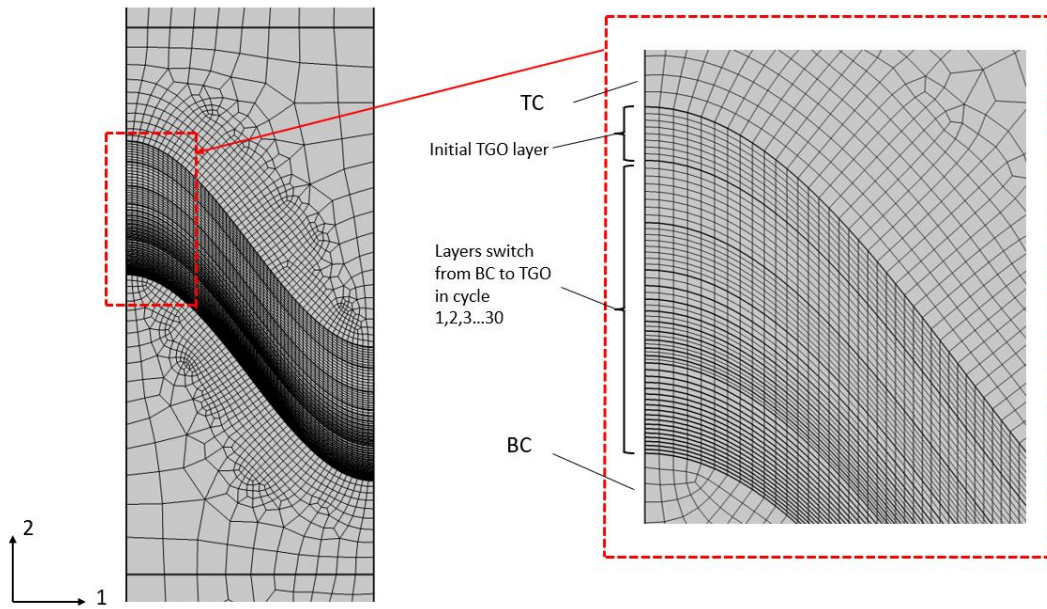


Figure 3-5. Interface mesh design and the zoom-in at TGO for the FEM model.

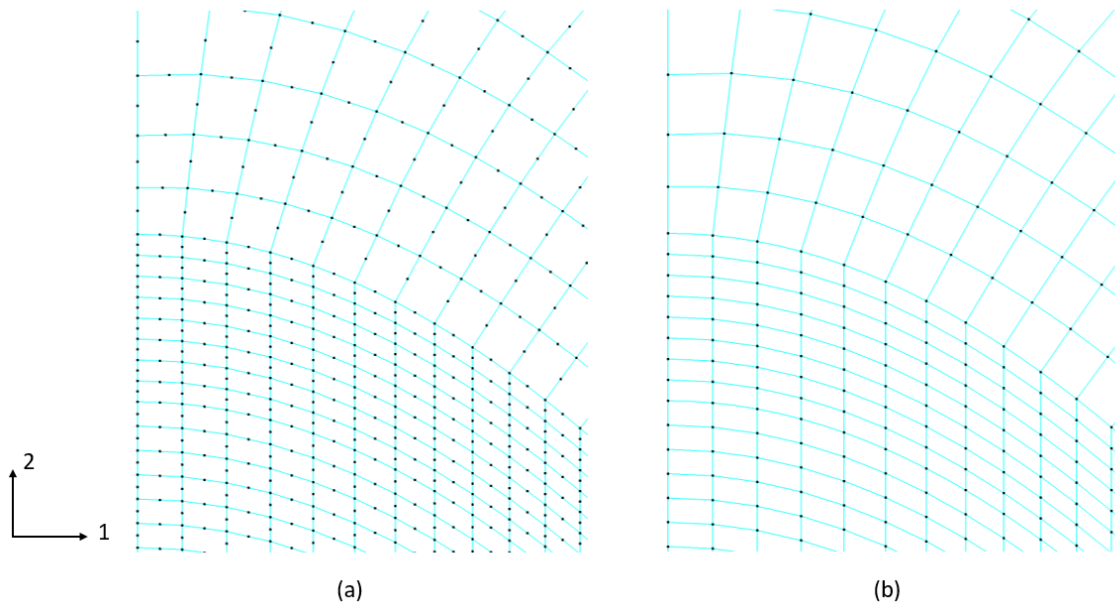


Figure 3-6. Mesh element for (a) displacement field; (b) temperature field.

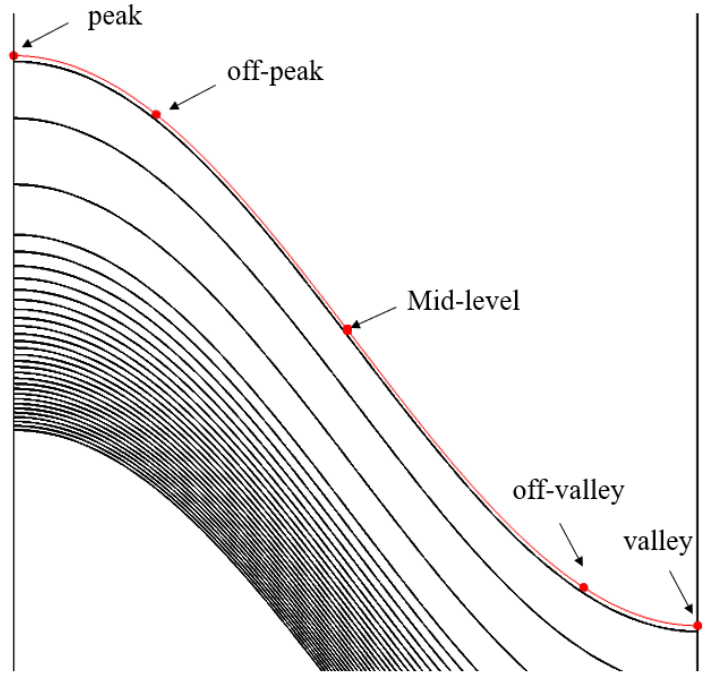


Figure 3-7. The positions of the simulation results

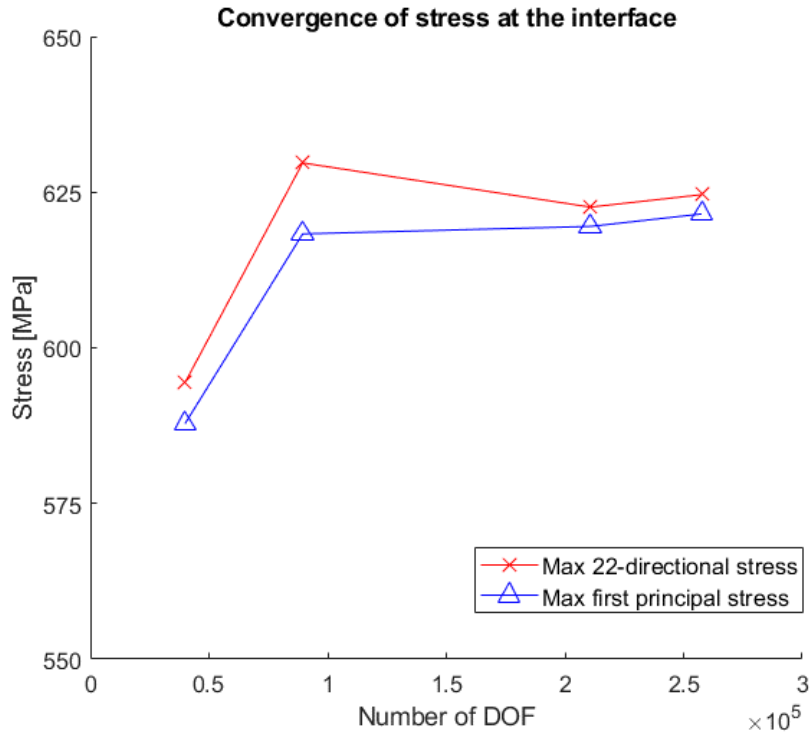


Figure 3-8. Convergence of maximum radial stress and first principal stress (σ_1) at TGO after the cool-down of the first cycle.

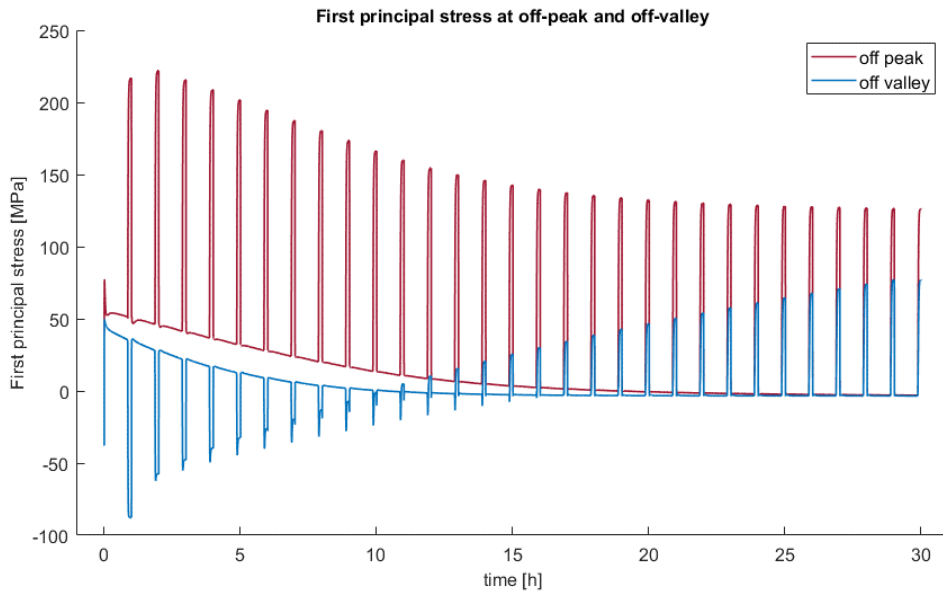


Figure 3-9. First principal stress (σ_1) for 30 thermal cycles at the off-peak and off-valley positions for reference case I.

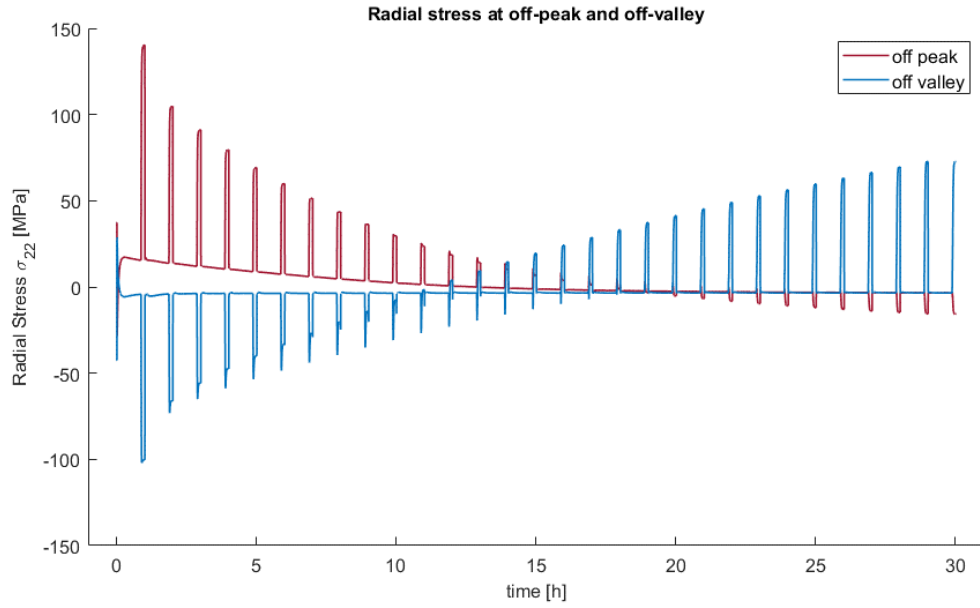


Figure 3-10. The radial stress (σ_{22}) for 30 cycles at the off-peak and off-valley positions for reference case I.

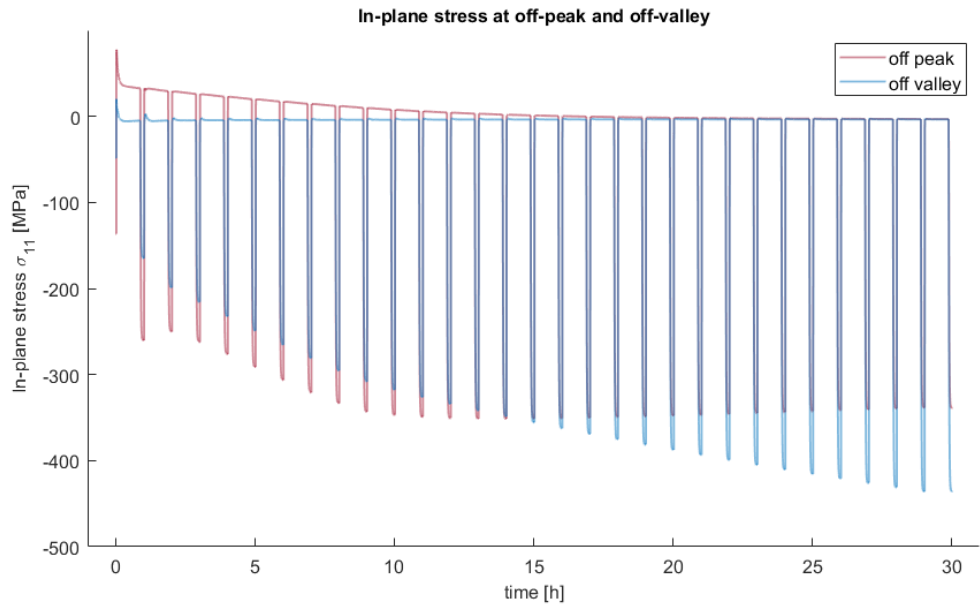


Figure 3-11. The in-plane stress (σ_{11}) for 30 thermal cycles at the off-peak and off-valley positions for reference case I.

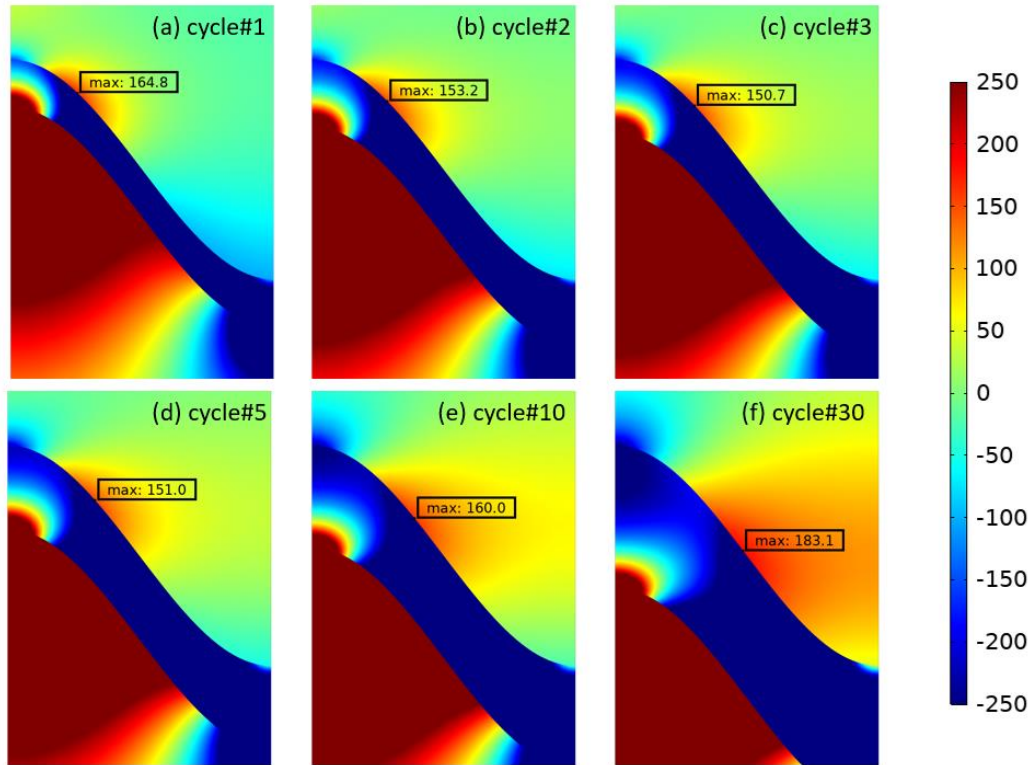


Figure 3-12. The radial stress distribution (σ_{22}) for the reference case I at the interface at the end of cycles denotes the maximum stress at TC.

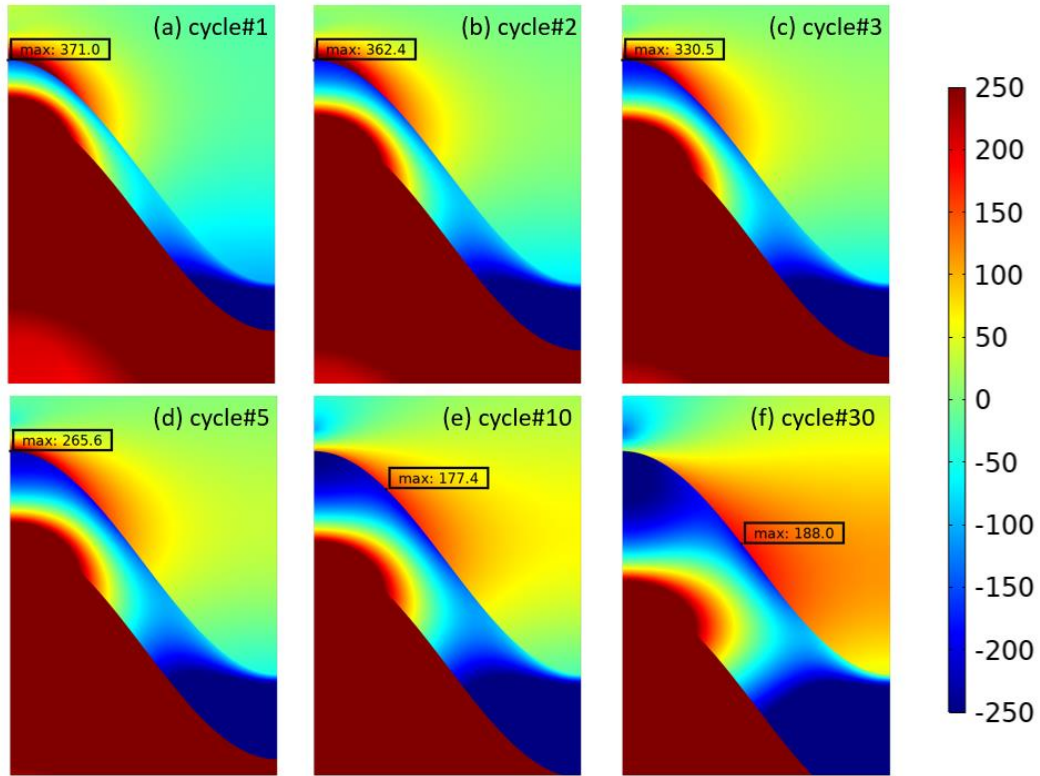


Figure 3-13. The first principal stress (σ_1) distribution for the reference case I at the interface at the end of cycles denotes the maximum stress at TC.

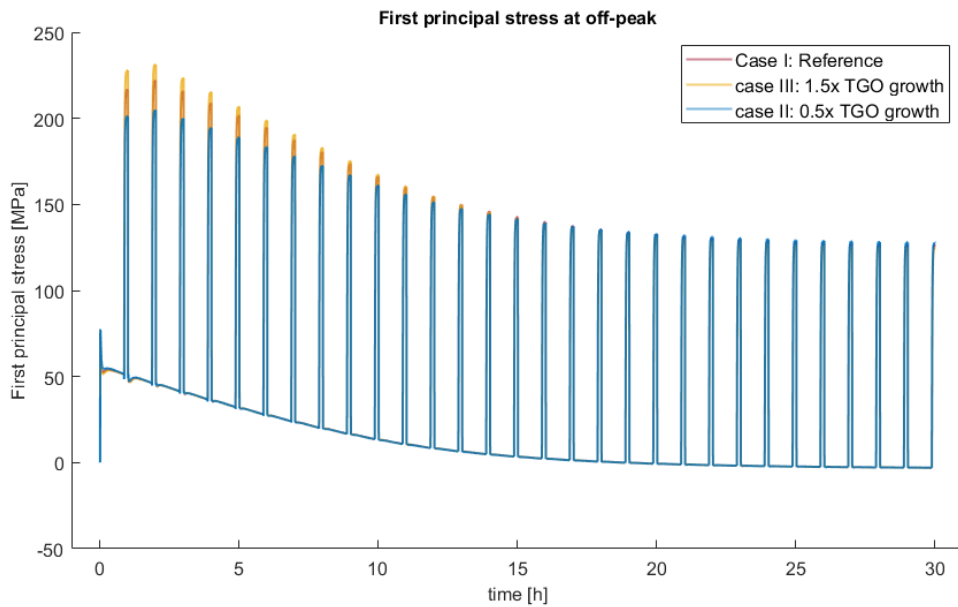


Figure 3-14. The first principal stress (σ_1) at off-peak position with different TGO growth rates (case I,II,III)

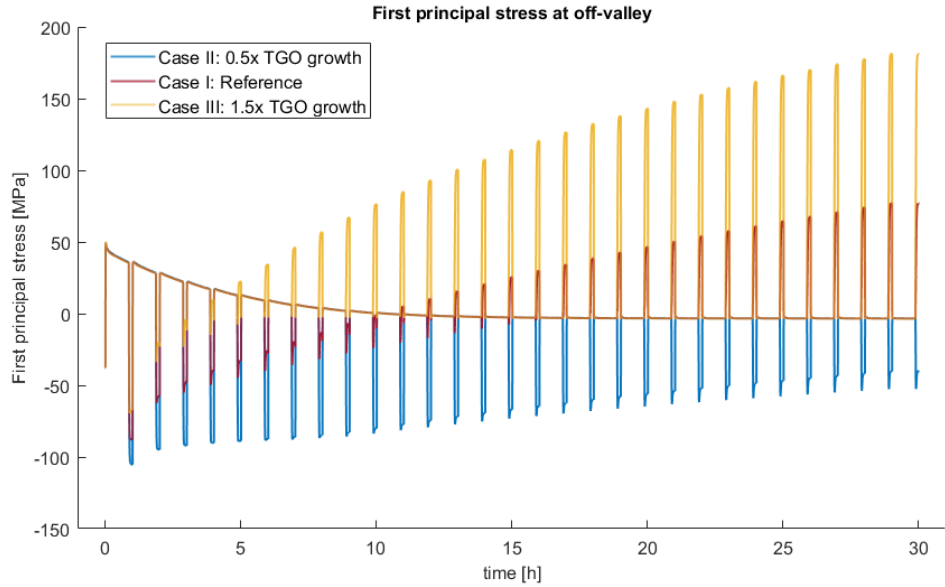


Figure 3-15. The first principal stress (σ_1) at off-valley position with different TGO growth rates (case I,II,III)

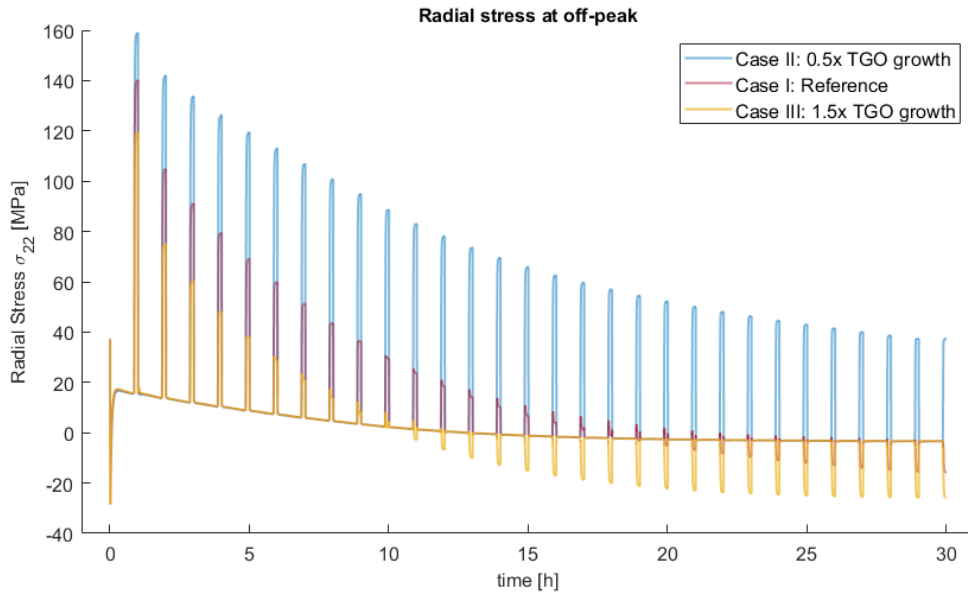


Figure 3-16. The radial stress (σ_{22}) at off-peak with different TGO growth rates (case I,II,III)

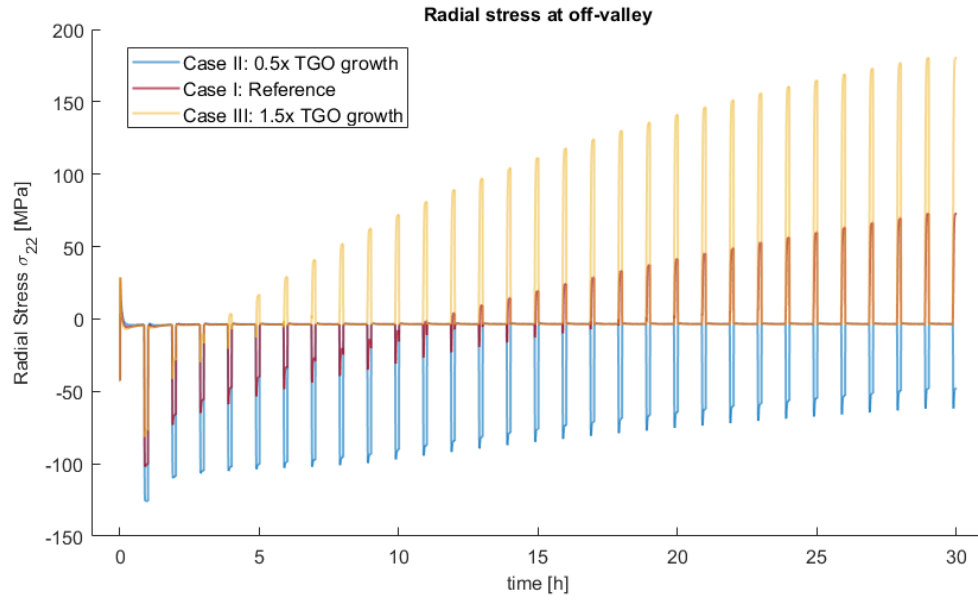


Figure 3-17. The radial stress (σ_{22}) at off-valley with different TGO growth rates (case I,II,III)

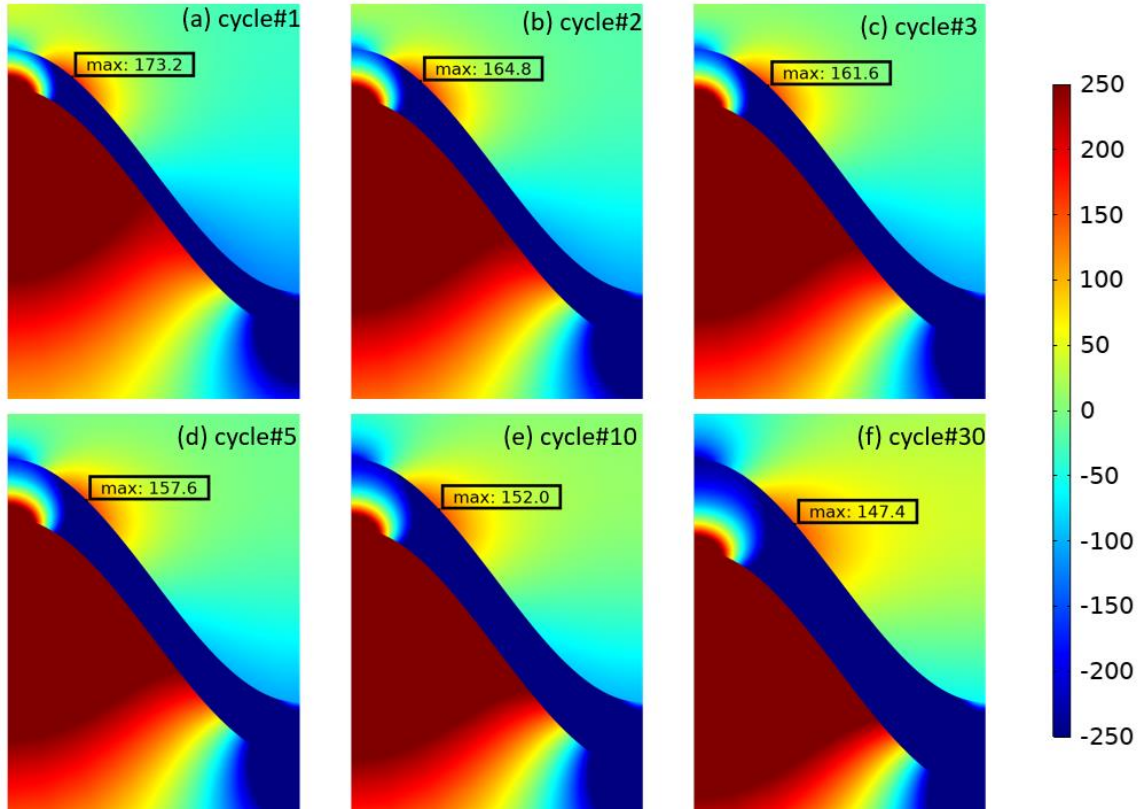


Figure 3-18. The radial stress distribution (σ_{22}) for the case (II): 0.5 times TGO growth, at the interface at the end of cycles denotes the maximum stress at TC.

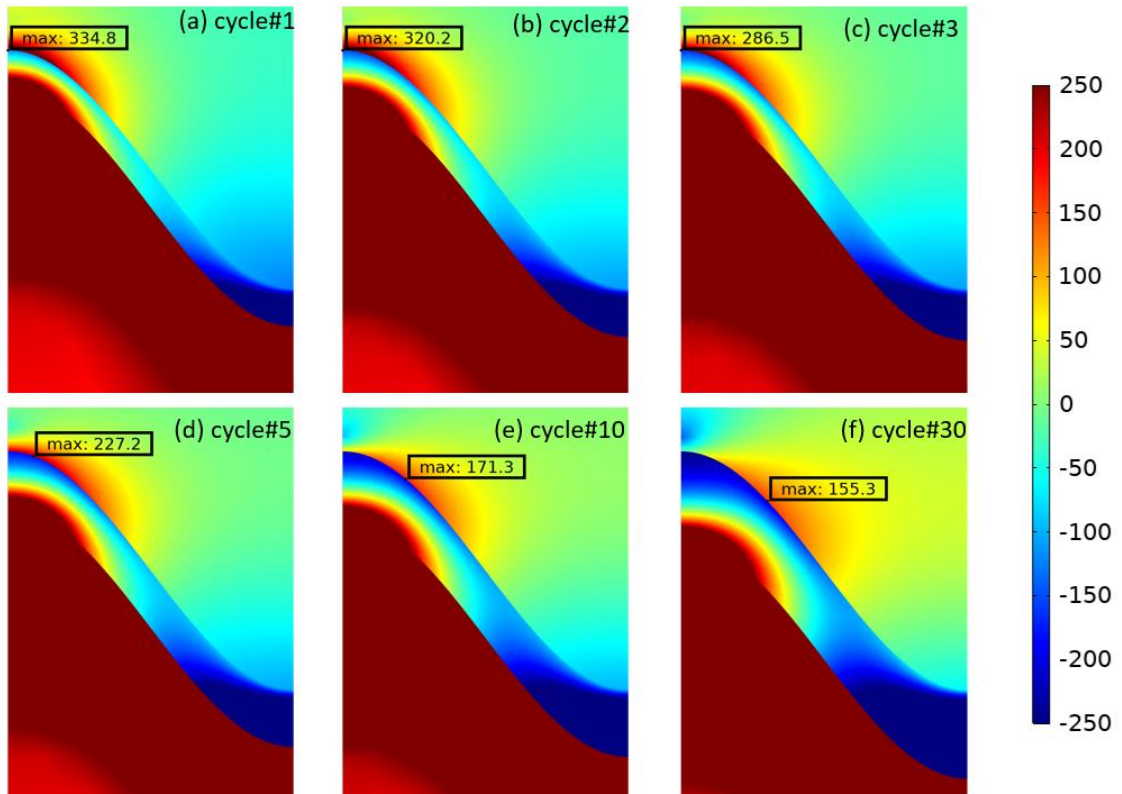


Figure 3-19. The first principal stress (σ_1) for case (II): 0.5 times TGO growth, at the interface at the end of cycles denotes the maximum stress at TC.

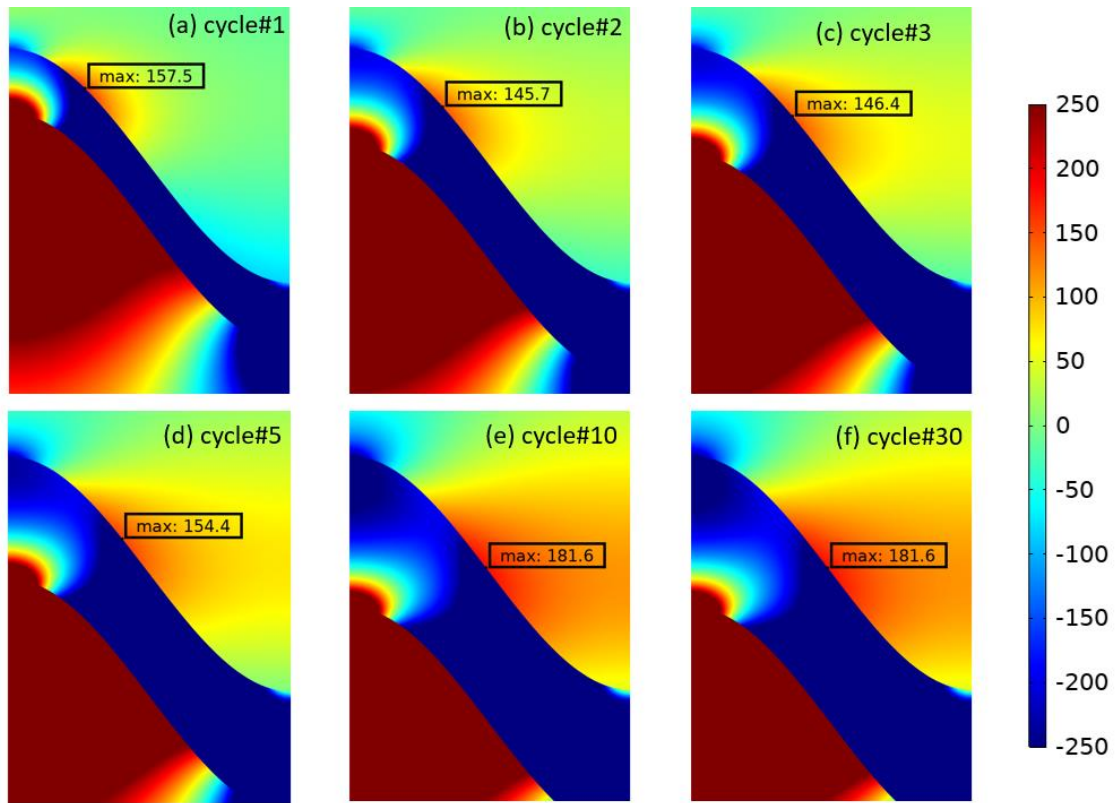


Figure 3-20. The radial stress distribution (σ_{22}) for the case (III): 1.5 times TGO growth, at the interface at the end of cycles denotes the maximum stress at TC.

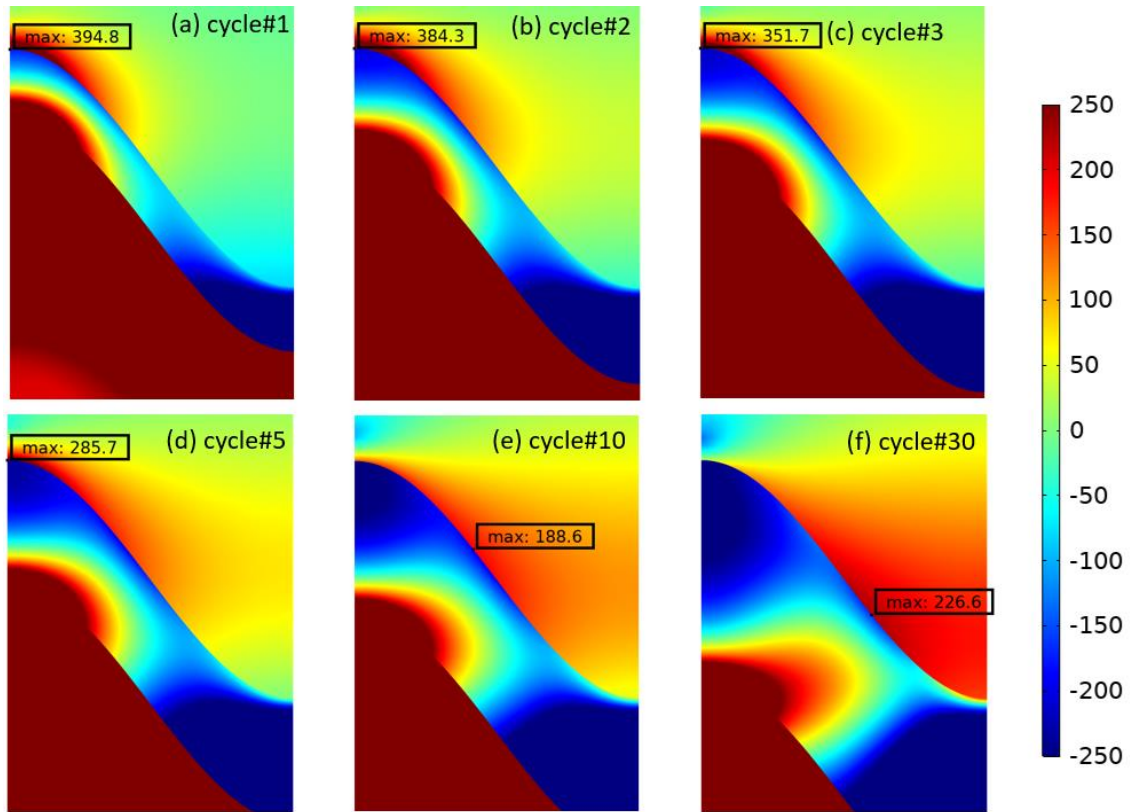


Figure 3-21. The first principal stress (σ_1) for the case (III): 1.5 times TGO growth, at the interface at the end of cycles denotes the maximum stress at TC.

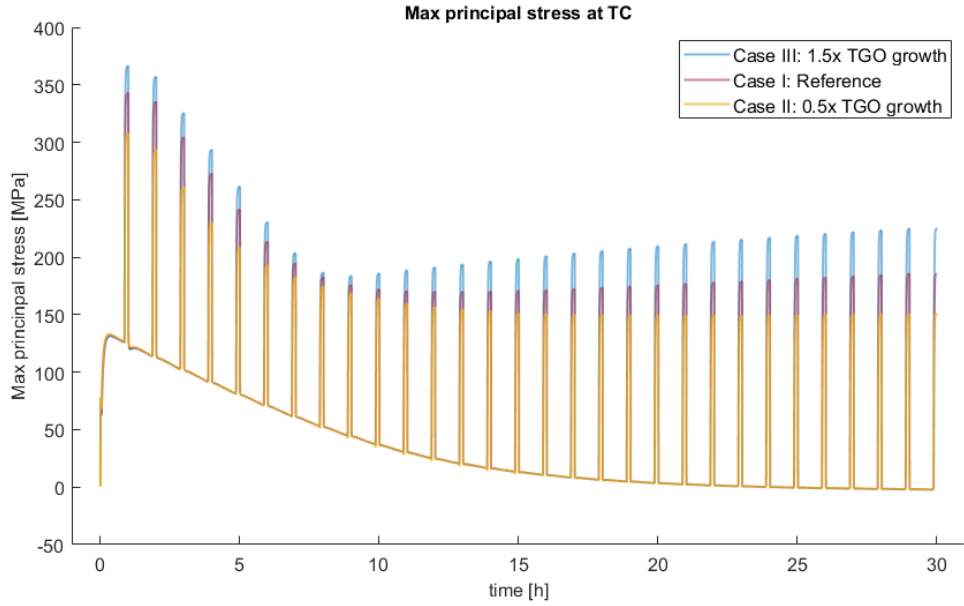


Figure 3-22. Max of first principal stress (σ_{1-max}) at TC with different TGO growth rates for case I, II, III

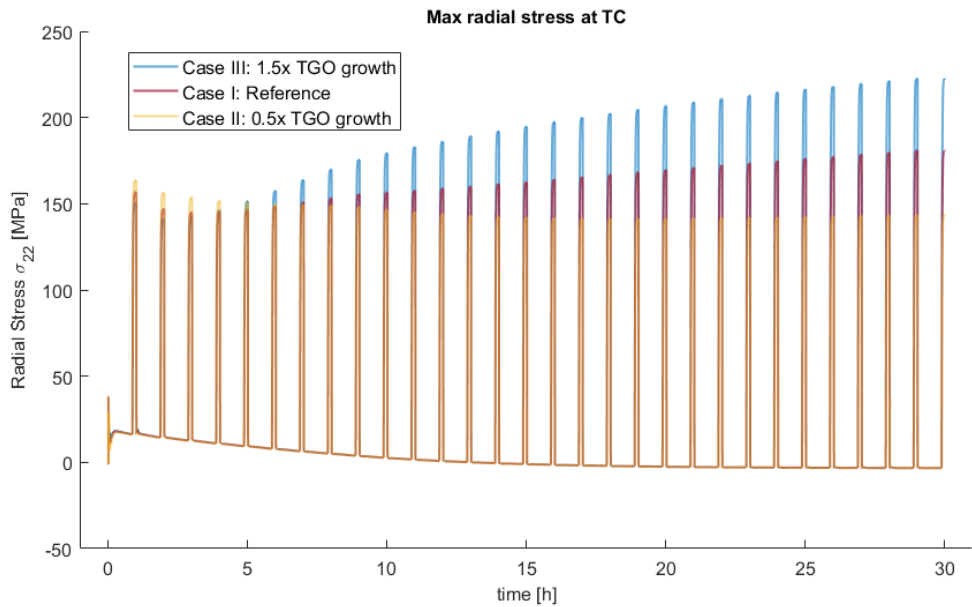


Figure 3-23. Max radial stress (σ_{22-max}) at TC with different TGO growth rates for case I, II, III.

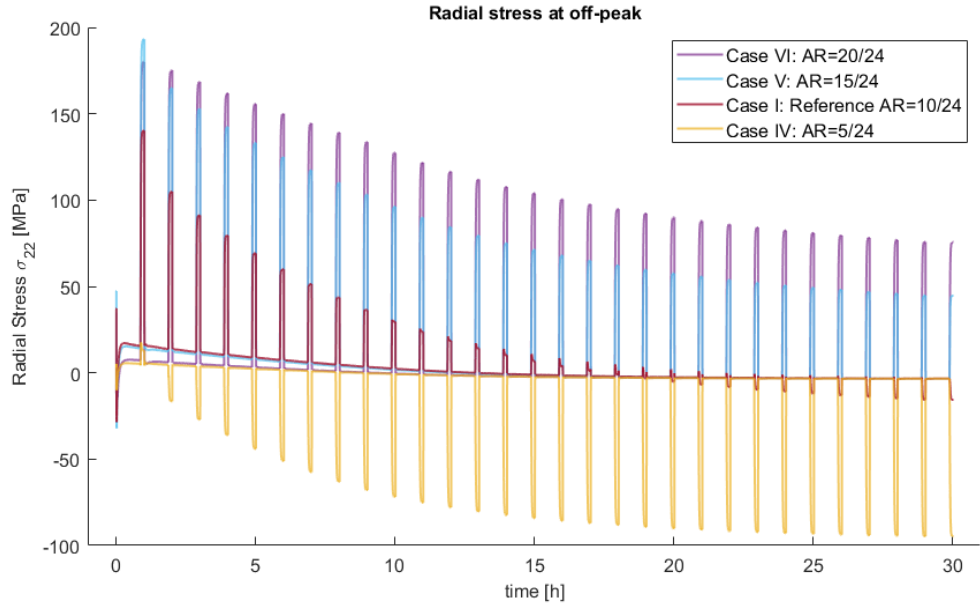


Figure 3-24. The radial stress (σ_{22}) at off-peak with different roughness aspect ratios for parametric study for case I, IV, V, VI.

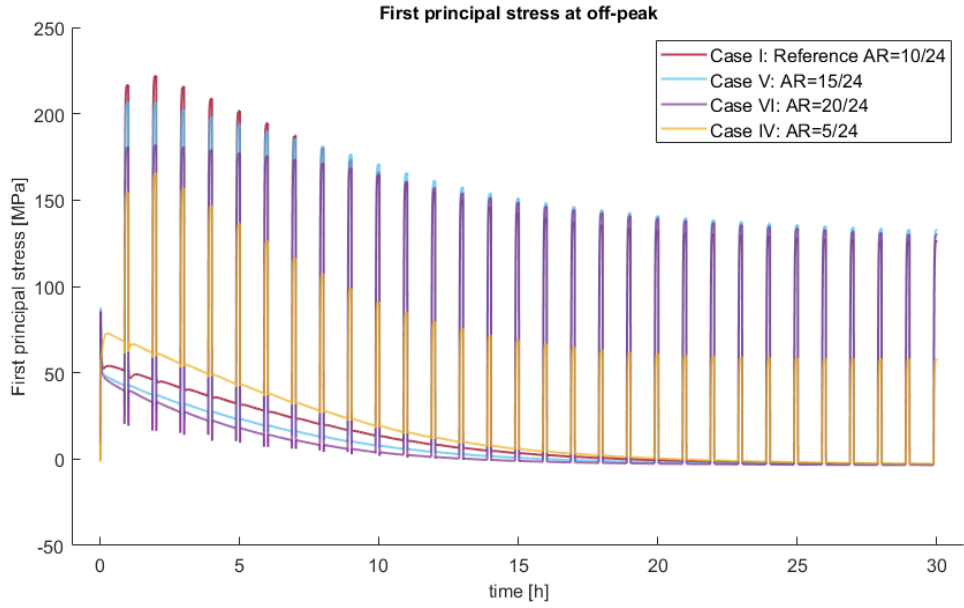


Figure 3-25. The first principal stress (σ_1) at off-peak with different roughness aspect ratios for parametric study of case I, IV, V, VI.

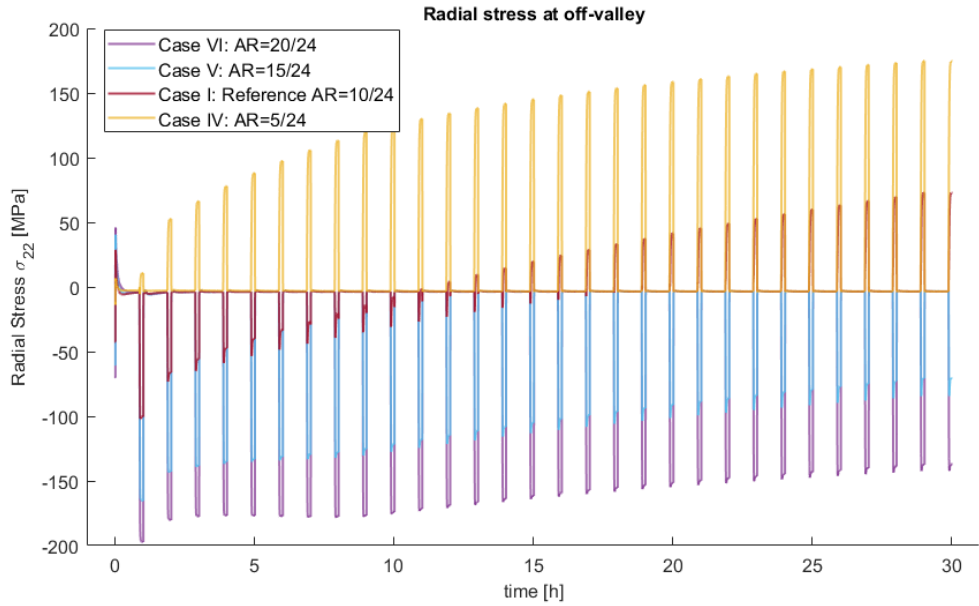


Figure 3-26. The radial stress (σ_{22}) at off-valley with different roughness aspect ratios for parametric study of case I, IV, V, VI.

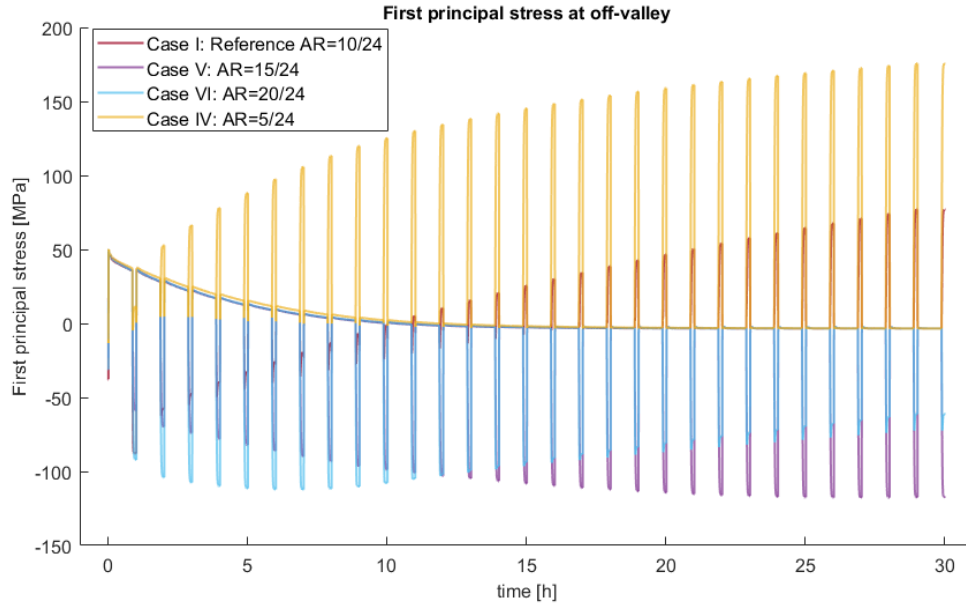


Figure 3-27. The first principal stress (σ_1) at off-valley with different roughness aspect ratios for parametric study of case I, IV, V, VI.

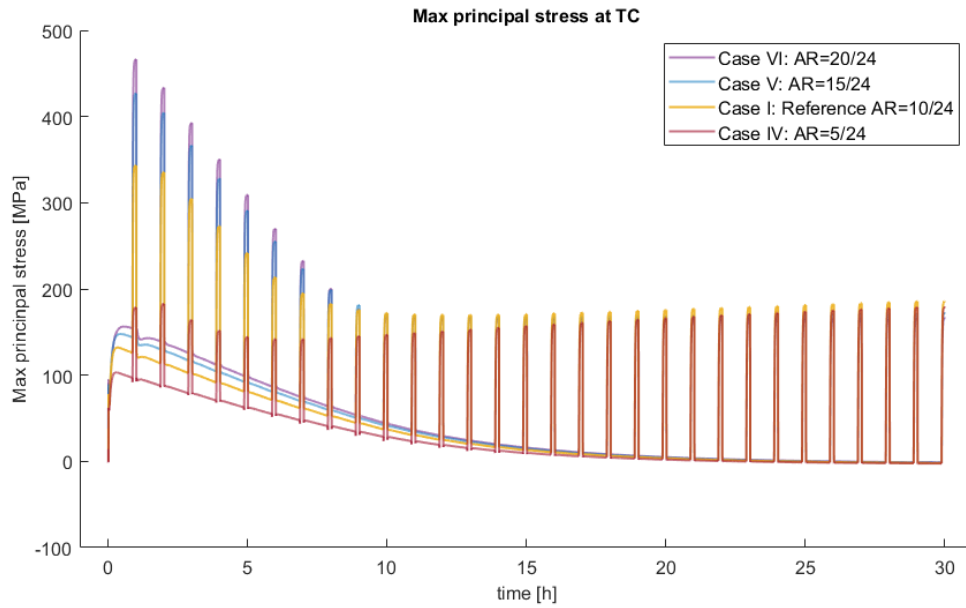


Figure 3-28. The max of first principal stress (σ_{1-max}) at the TC with different roughness aspect ratios for parametric study of case I, IV, V, VI.

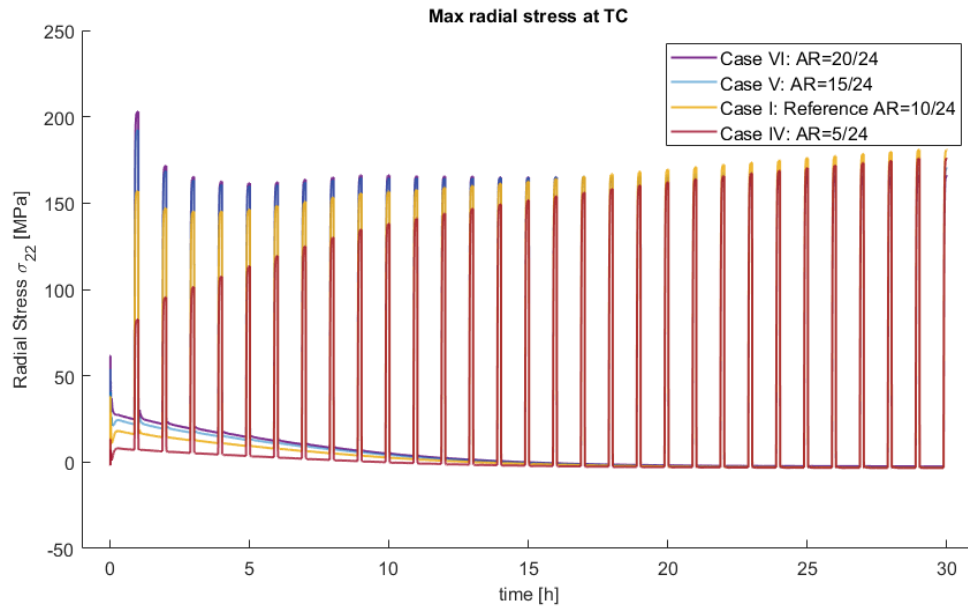


Figure 3-29. The max radial stress (σ_{22-max}) at the TC with different roughness aspect ratios for parametric study of case I, IV, V, VI.

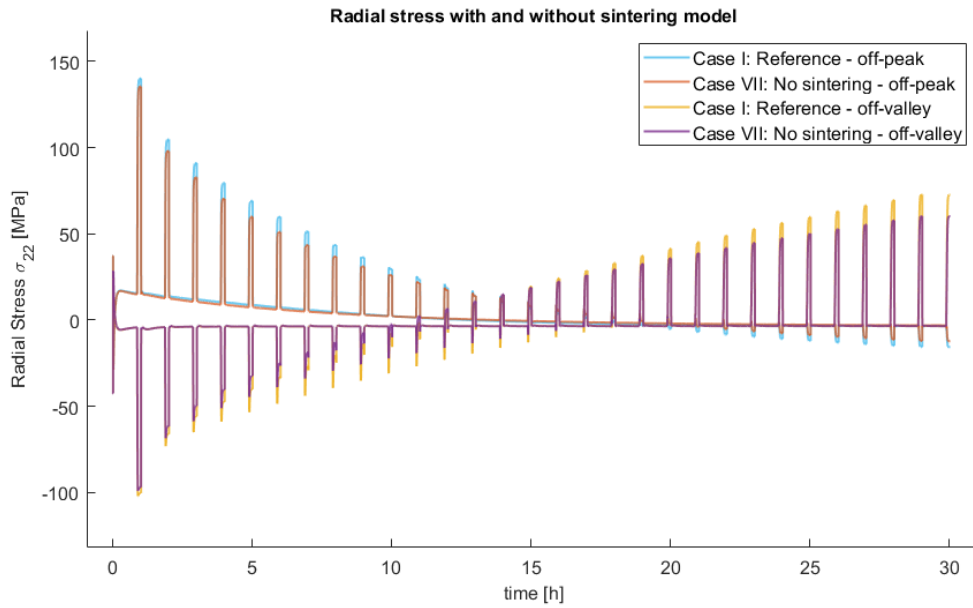


Figure 3-30. The radial stress (σ_{22}) at off-peak and off-valley for parametric study sintering model of case I, VII

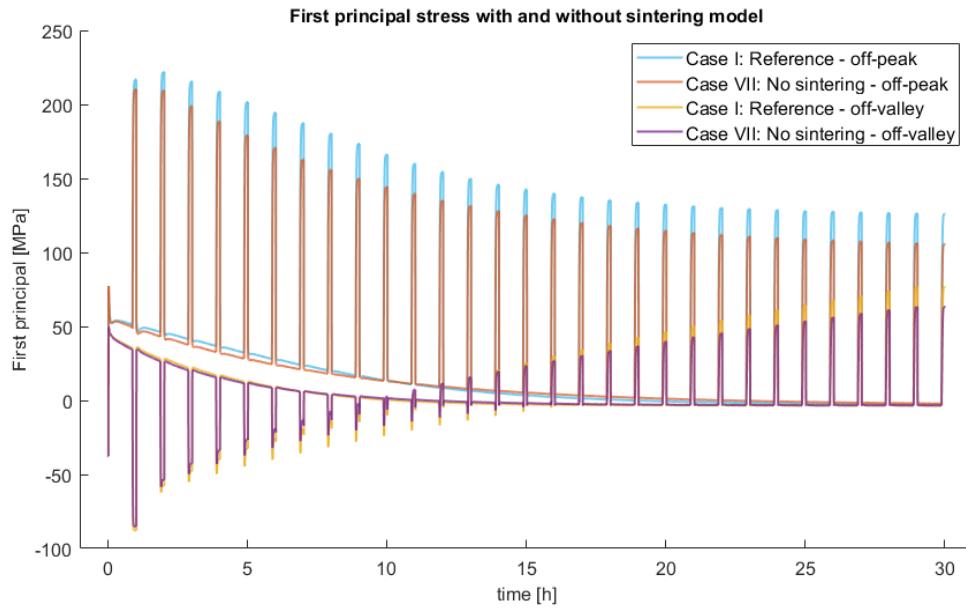


Figure 3-31. The first principal stress (σ_1) at off-peak and off-valley for parametric study of case I, VII

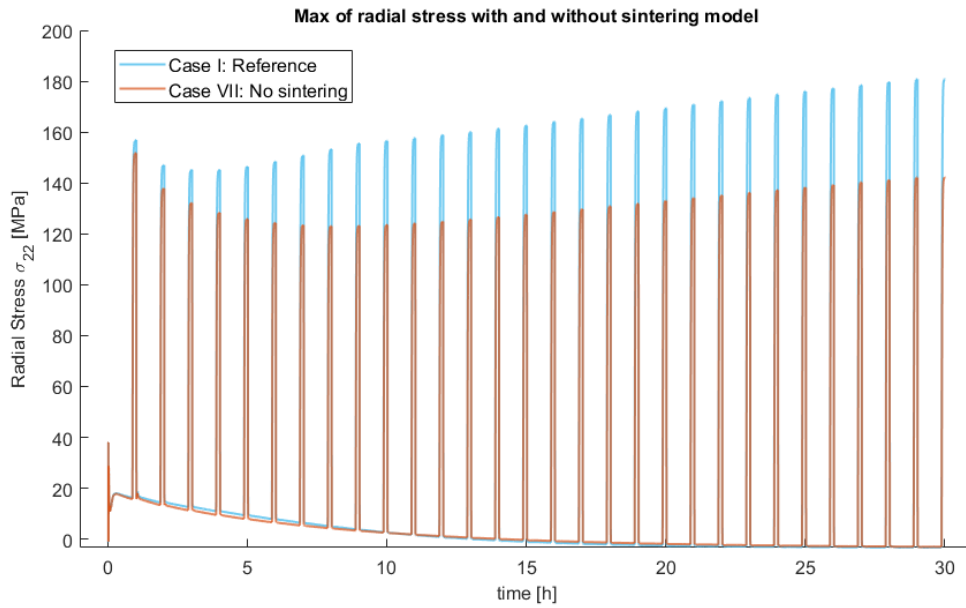


Figure 3-32. The maximum radial stress (σ_{22-max}) at TC for parametric study of case I and VII.

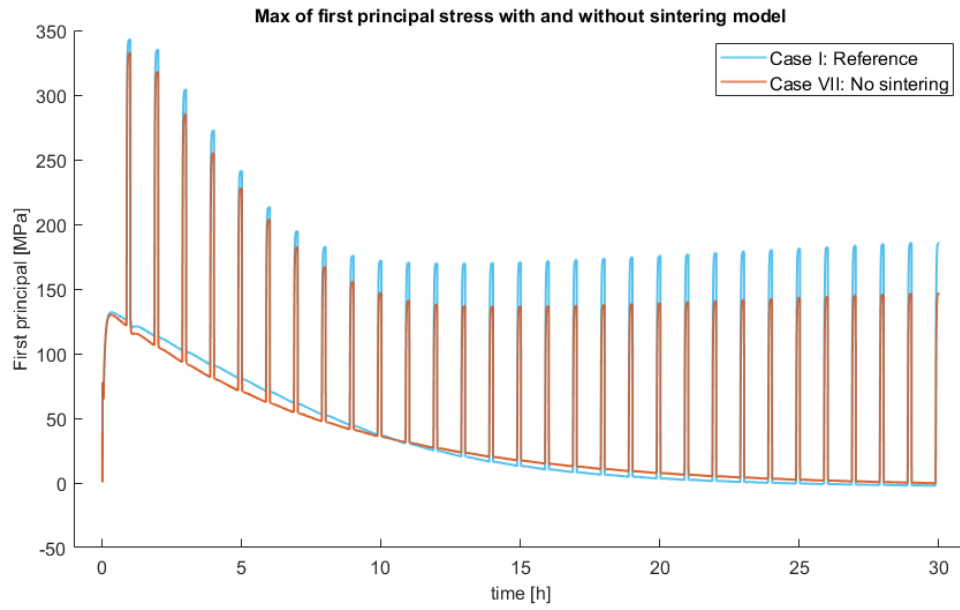


Figure 3-33. The maximum of first principal stress (σ_{1-max}) at TC for parametric study of case I and VII.

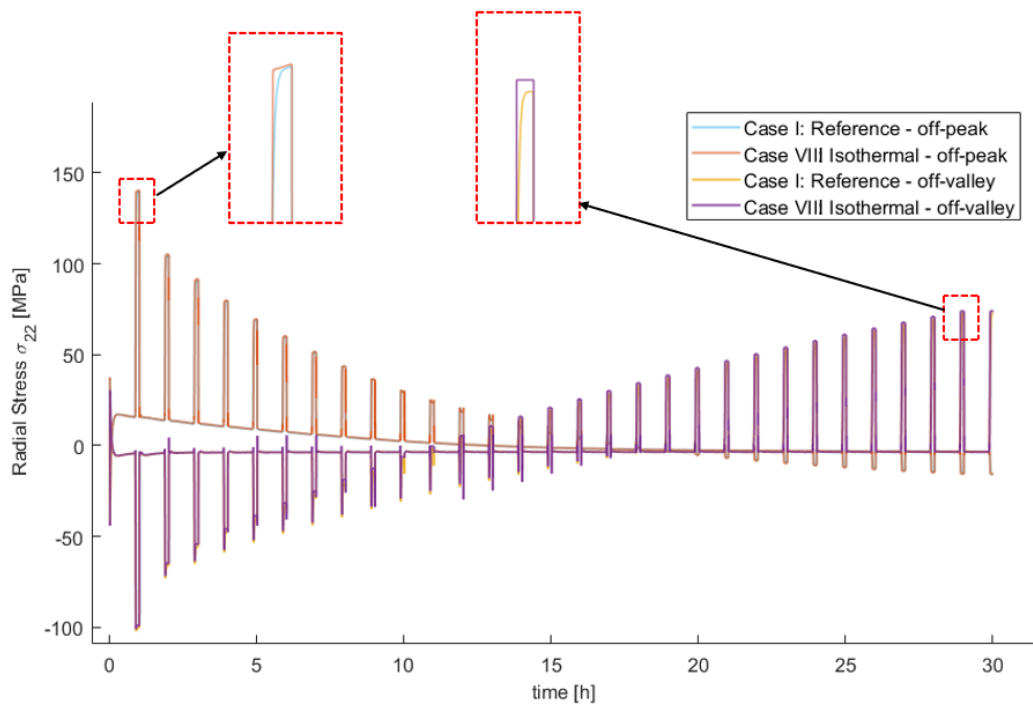


Figure 3-34. The radial stress (σ_{22}) at off-peak and off-valley for parametric study sintering model of case I, VIII

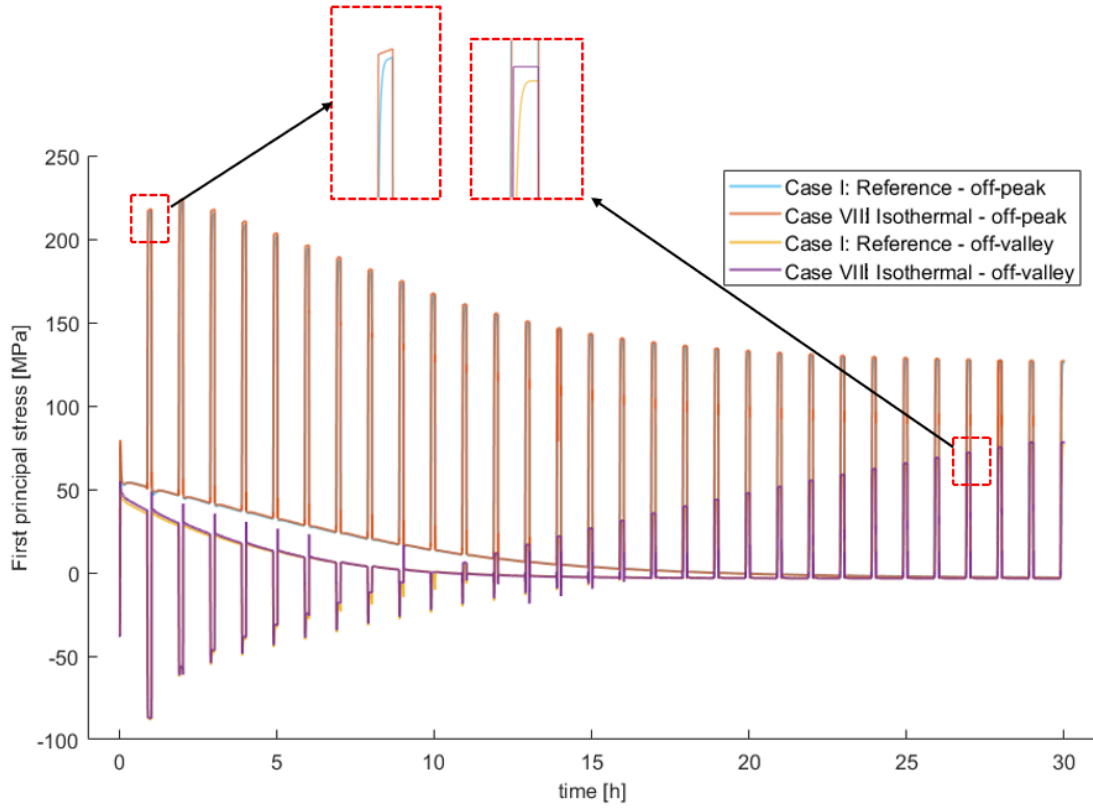


Figure 3-35. The first principal stress (σ_1) at off-peak and off-valley positions for parametric study sintering model of case I, VIII

4. Crack propagation study with Phase field damage model

This chapter studies the crack propagation estimation of APS TBCs using commercial software COMSOL Multiphysics vers. 5.6. This simulation aims to evaluate the crack propagation progress with different parameters including the interfacial roughness, TGO growing speed, thermal gradient, sintering model, and crack evolution.

The COMSOL Multiphysics software features the Multiphysics coupling and is capable of coupling the conventional solid state model and heat transfer model with the phase field damage model. The phase field damage is a built-in module in COMSOL vers. 5.6. The phase field damage model can simulate the crack propagation independent of the mesh, by applying a phase field variable, from 0 to 1, to determine how much the material is damaged. If the material is damaged in an iteration, in the next iteration, the damaged elements in the crack are simulated as degraded material. This method benefits from modeling the crack without modeling the discontinuity and is a trending method for damage estimation.

The verification example, finite element model geometry, phase field model definitions, boundary conditions, material properties, mesh designs, and parametric study plan are outlined below, followed by the results with discussions. The detail explanation about the iteration of phase field model was previously presented in Chapter 2.

4.1. Verification Example

The notched plate with a hole is simulated in COMSOL Multiphysics to examine the capability of the model to simulate the crack propagation. The simulation setup follows the testing setup in [100]. The geometry of the test specimen is given in Figure 4-1 (a). The material of the specimen is cement mortar with $E = 6 \text{ GPa}$, $\nu = 0.22$, and $G_c = 2280 \text{ J/m}^2$. The displacement load is applied to the upper circular pin and held fixed at the lower pin. For the phase field damage solver, the length scale is set as $l_{int} = 0.25 \text{ mm}$. The mesh near the crack path (known in the test) is refined with a maximum element size of $h_{elem} = 0.25 \text{ mm}$. The range of displacement input is from 0 to 2 mm.

The computation results with displacement input of 2 mm are shown in Figure 4-1 (b). The calculated path has a good agreement with the experimentally observed crack path. The load-displacement curve of the notched plate fracture simulation is shown in Figure 4-2. The curve linearly increases as the crack propagates. Once the plate is fully damaged at the left of the hole, the load drops quickly. The load increases again as the crack continues to grow at the right of the hole. The calculated peak load is at 0.63 kN matches the experimental peak load at 0.6 kN in [100]. Next the phase field model is used to simulate the crack propagation in TBC.

4.2. FEM model setup, geometry, and boundary condition

In this FEM simulation, the geometry used is the same as the previous Chapter 3. Additionally, the cracks are inserted followed by the cracks in the SEM images. Figure 4-3 is an SEM image of the APS-TBC testing specimen, showing that horizontal cracks are distributed around the TC/TGO interface. At least two cracks are observed at the off-peak, two at the mid-level, and one crack above the roughness. With this model, a crack

with a length of $0.5\mu\text{m}$ is implemented at the off-peak of the roughness, see Figure 4-4, to observe the crack propagating behavior under different conditions. Results will be discussed as follows. The crack tip near the interface side is rounded to concave corners to avoid the stress concentration at the sharp corner.

4.3. Material properties and mesh designs

The material properties used in this chapter are the same as Chapter 3, please refer to section 3.3

The mesh design for this chapter is an extension of the geometry in Chapter 3. Since the initial crack is implemented, a refinement is necessary near the crack to ensure the convergence of the phase field model. The width of the initial crack is set as $0.06\mu\text{m}$ with a square shape crack tip. The square crack tip design follows the examples of notched concrete beam with three-point bending test and 2D notches square plates subject to shear load in [78], [101]. The internal length scale l_{int} is set as $0.06\mu\text{m}$ as well to ensure the diffusion zone is large enough to avoid discontinuity issues. The maximum mesh element size at the potential crack path is set as $h_{elem} = l_{int}/2 = 0.03\mu\text{m}$ to ensure the precision of topology, as suggested by Zhou et al. [78].

Two mesh refinement designs are shown in Figure 4-5 and a convergence test is performed in 4.5.1 to check if the phase field topology is independent of the mesh and check the fineness of the mesh.

4.4. Parametric study plan

To better validate the phase field crack estimation result, a set of parametric studies is necessary. Due to the time cost of phase field damage simulation, the

parametric study in this section is not as much as in Chapter 3. The reference case (IX) uses the same geometry as the reference case (I) in Chapter 3, but a horizontal crack is implemented near the off-peak position. The case (X, XI) will change the roughness's aspect ratio to $AR=15/24$ and $5/24$ to study the off-peak crack propagation behavior and compare the stress distribution result in Chapter 3. The case (XII) will implement the crack to the mid-level of the roughness to discover the crack propagation and make a comparison with stress results. Detail configuration of the parametric study please refer to Table 4-2. The TGO growth, thermal gradient, and sintering model are not noted but they are implemented in all cases.

4.5. Results

4.5.1. Convergence test

The convergence test for the phase field crack propagation zone was performed at the end of the first thermal cycle. Figure 4-5 shows the mesh refinement with different orientations of elements, where (a) follows the crack growth direction and (b) follows the initial crack direction (in horizontal). The maximum size of the two meshes is the same. The result at the end of cycle# 1 for two mesh configurations is shown in Figure 4-6. The result for mesh (b) shows that the crack path is crossing the mesh in diagonal direction, instead of propagating following the mesh orientations. Also, the result for mesh (b) has almost the same length and direction as mesh (a), although in some areas with coarser mesh elements may widen the total damage zone. It proves the mesh design with either mesh (a) or (b) works on the phase field model.

For the mesh element size in another area, it is not further refined since it is proved converged in section 3.6.1.

4.5.2. Crack propagation at the crack near TC off-peak

In Chapter 3, the FEM analysis concluded that tensile stress is distributed near the off-peak region. In this section, the crack growth behavior of a horizontal crack at the off-peak position will be investigated. The results for the crack propagation are present in two parts: the phase field crack topology and the damaged first principal stress distribution during the crack propagation. In terms of the damaged first principal stress, it is defined as the first principal stress multiplying the phase field variable d , to precisely describe the stress state at the damaged nodes.

Figure 4-7 demonstrates the process of phase field crack propagation from cycle#1 to #7 for case IX. At cycle# 1- 3700s, the crack grows towards the top right direction for about $0.58\mu\text{m}$. In the stress plots, Figure 4-8 shows the stress at the crack tip moves as the crack propagates. At cycle# 2 -7300s, the crack length continually grows to $1.48\mu\text{m}$. The stress plots read that the first principal stress at the peak is reduced, and it is caused by the growth of TGO according to the results from Chapter 3. The growth of TGO moves the location of maximum first principal stress down along the interface like case I in Chapter 3, but it is not obvious in the stress plot due to the presence of crack discontinuity, and the crack propagation at cycle 2 relaxed the stress center. At cycle# 3, the crack grows to $1.97\mu\text{m}$ then the crack stops growing at cycle# 4-7. In the stress plots, the stress magnitude reduces rapidly at the peak and the crack tip. Also, the location of maximum stress moves to the mid-level of the roughness as shown in Figure 4-8 (f-i). Based on the results, it appears that the crack will stop propagating due to the stress magnitude at the crack tip gradually reducing with thermal cycles.

4.5.3. Parametric study of roughness ratio

In section 3.6.4, the parametric study of case I, IV, V, and VI showed that as AR increases, the first principal stress is less affected by the TGO growth. Therefore, for case V, the first principal stress at off-peak is about 200MPa at cycle 1, and 150 MPa at cycle# 30. Compared to the reference case I, the stress level is slightly lower at the first 6 cycles, but similar in the rest. It is fair to assume that the crack at off-peak in case X may propagate slower than the reference case.

Figure 4-9 and Figure 4-10 show the phase field and first principal stress contour during the crack propagation process for case X with $AR=15/24$. The crack path propagates in the top right direction, like in the reference case, but it doesn't go up as much as in the reference case. At the end of cycle#1, the length is $0.6\mu\text{m}$. At cycle#2 and 3, the length grows to 1.46 and $1.85\mu\text{m}$, then it stops propagating until cycle#30. Spotting the stress distribution plot, the stress concentration zone moves with the crack tip. After cycle#3, the principal stress center gradually moves to the mid-level of the roughness until cycle#30, and the stress at the crack tip is relaxed at the end of cycle#30. The result matches the assumption according to the stress analysis in case V.

The phase field crack propagation and damaged first principal stress results for case XI are shown in Figure 4-11 and Figure 4-12. The crack path did not propagate at cycle# 1. Then it propagates at top right direction in cycle# 2 and 3 at a short distance and larger angle about the initial crack orientation. The crack length at $0.20\mu\text{m}$ then stops propagating in the remaining cycles. It can be explained with the first principal stress plots. At cycle #1, the stress center is at the peak position, which is unable to propagate the crack, while at cycle #2 and 3, the location of maximum first principal stress moves to

the crack position, and it propagates a short distance. Afterwards, due to the continue movement of crack center, the stress level at the crack tip is reduced and unable to further propagate the crack. These results match the assumption in case IV.

4.5.4. Parametric study on initial crack position

In case XII the crack was relocated to the mid-level of the rumpling, and it will be compared to the results in reference case IX. The crack phase field and damaged first principal stress results for case XII are shown in Figure 4-13. In the crack phase field, the legend is from 0 to 0.2 means the initial crack has never propagated (fully damage at phase field =1) but it is partially damaged at the crack tip. As the stress plots display, the stress center for this case gradually moves from the peak position to the valley, but the maximum stress level is reduced as it moves to the valley. Therefore, it is unable to propagate the crack. This result agrees with the assumption in Figure 3-22, that the maximum first principal stress reduces from 350 MPa in cycle# 1 to 150 MPa in cycle# 10, making the crack unable to propagate. Even though the stress level increases in the latter stage with sintering, it is unable to propagate the crack at the mid-level.

4.6. Discussions

The results of the crack propagation in phase field model are unable to validated by experiments at this moment. However, it can be partially validated by the stress contour plots results with those in Chapter 3. For Figure 4-8 the maximum first principal stress σ_1 initially located near the peak position. As cycle increased, maximum σ_1 is decreased and gradually moved away the peak position to the crack. Even though only 7 cycles are simulated, the stress distribution and stress level decrease can be observed, and it matches the predictions in the stress analyses (see Figure 3-13). The stress level is

decreased more than the model without crack, but it is consistent because the crack propagation consumes energy, and it reduces the stress level in the TC. The Figure 4-10 with full thermal cycle is better explained it. The maximum σ_1 moves farther to the mid-level from cycle#5 to cycle#30. And also, the σ_1 at crack tip is reduced in the later cycles then the crack stops propagate, and this matches the estimation in Chapter 3. In Chapter 3 the parametric study with different AR (case I,IV,V,VI) results showed the maximum σ_1 and σ_{22} varies with AR. The higher AR, maximum stress is higher at early stage. At later stage, the maximum σ_1 and σ_{22} becomes similar (see Figure 3-28 and Figure 3-29). The equivalent parametric study in Chapter 4 (case IX,X,XI), showed that the final crack length for case X (AR=15/24) is much longer than case XI (AR=5/24) (see Figure 4-10 and Figure 4-12). These behaviors are consistent the parametric case study in Chapter 3: σ_1 is higher with high AR.

A similar simulation using XFEM method was conducted by Jiang et al. [63]. A preliminary stress analyses were simulated and the results are consistent with our research. Similar to this research, a horizontal crack was implemented at the off-peak position and the crack propagation criteria is the principal stress. The results showed the cracks only propagates in the 1st cycle during the dwell and cool-down period and stops propagates. The final length is about 20 μm in a sinusoidal interface with 80 μm . The length is longer than my model (which is $\sim 2 \mu m$ in 24 μm wavelength), but it is consistent because the critical stress for Jiang et al. model is lower and the aspect ratio is much smaller.

The crack has two ends, one end is at the TC/TGO interface. Currently the phase field model is only simulate the crack propagation in the TC, but the stress concentration

at the interface end is potential to propagate, either into the TGO and BC or delaminate along the TC/TGO interface, is worth to study in the future.

4.7. Summary

In this chapter, the local crack propagation behavior during the thermal cycle is successfully simulated with the phase field method and its behavior at some other conditions like different roughness AR and crack location. In the reference case, the crack at the off-peak position grows to the top right direction in the first 2 or 3 cycles. Then the crack stops propagating because the location of maximum principal stress is moved away. With different aspect ratio AR , the final crack length and the propagation direction are varied. But at all cases the crack grows fastest at cycle#2 and 3 because the maximum stress at TC is very close to the crack. The crack is unable to continue moving to the right end in the model due to the stress magnitude decrease with TGO growth. Therefore, it can be assumed that the local cracks initiated at off-peak position are unable to damage the whole layer of coating. When relocating the crack to the mid-level of the roughness, the crack did not propagate during the 30 hours thermal cycles, which is reasonable when considering the maximum of principal stress is reducing as TGO thickness increases, but you still can observe the stress accumulated at the crack tip at cycle# 30, that has the potential of propagating when criterion changes.

The purpose of this part is not only to simulate the crack in these scenarios and also proves the feasibility of using the phase field damage model to simulate the crack propagation at TC. More scenarios like different geometry, multiple cracks interaction, and different crack orientations can use this method to estimate the failure or lifespan of the coating in further studies.

Table 4-1. Phase field damage model properties [60]

Phase field damage parameters	Signs	Values
Critical fracture stress	σ_c	300 MPa
Post-peak slope	ξ	0.2
Internal length scale	l_{int}	0.06 μm
Viscous regularization	τ	1s

Table 4-2. Parametric study configurations and case number

Case	#	Crack location	Aspect ratio
Reference	IX	Off-peak	10/24
Roughness AR 15/24	X	Off-peak	15/24
Roughness AR 5/24	XI	Off-peak	5/24
Mid-level crack	XII	Mid-level	10/24

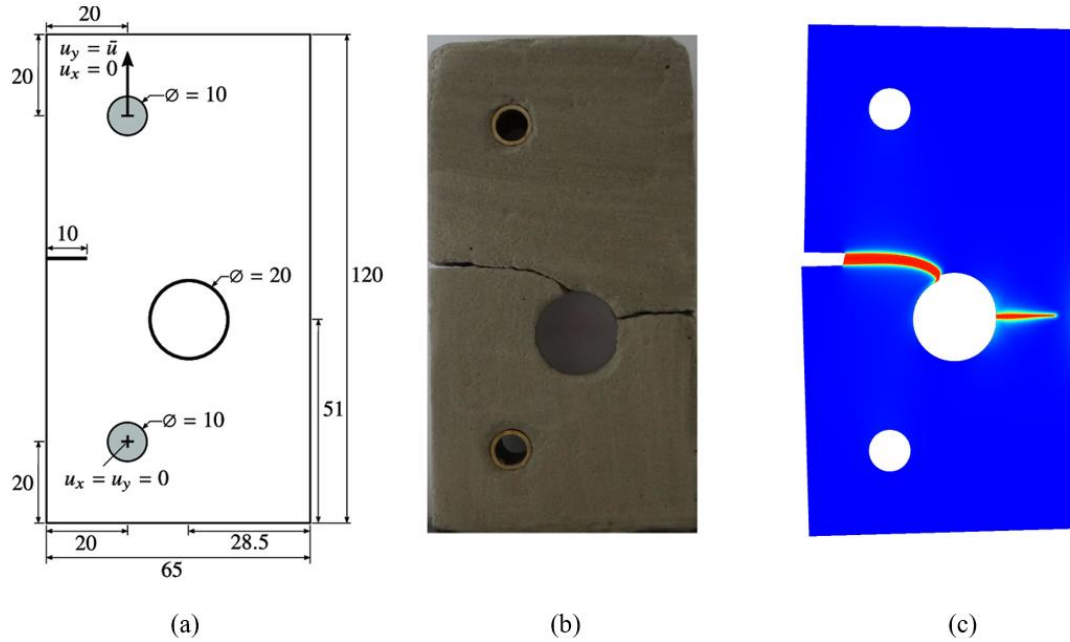


Figure 4-1. (a) The dimensions of the notched plate with a hole specimen, in [mm] [102] (b) The fractured notched plate with a hole specimen tested in [100] and (c) the crack path calculated with phase field damage model with displacement input of 2mm. (Copyright permission, Springer Nature)

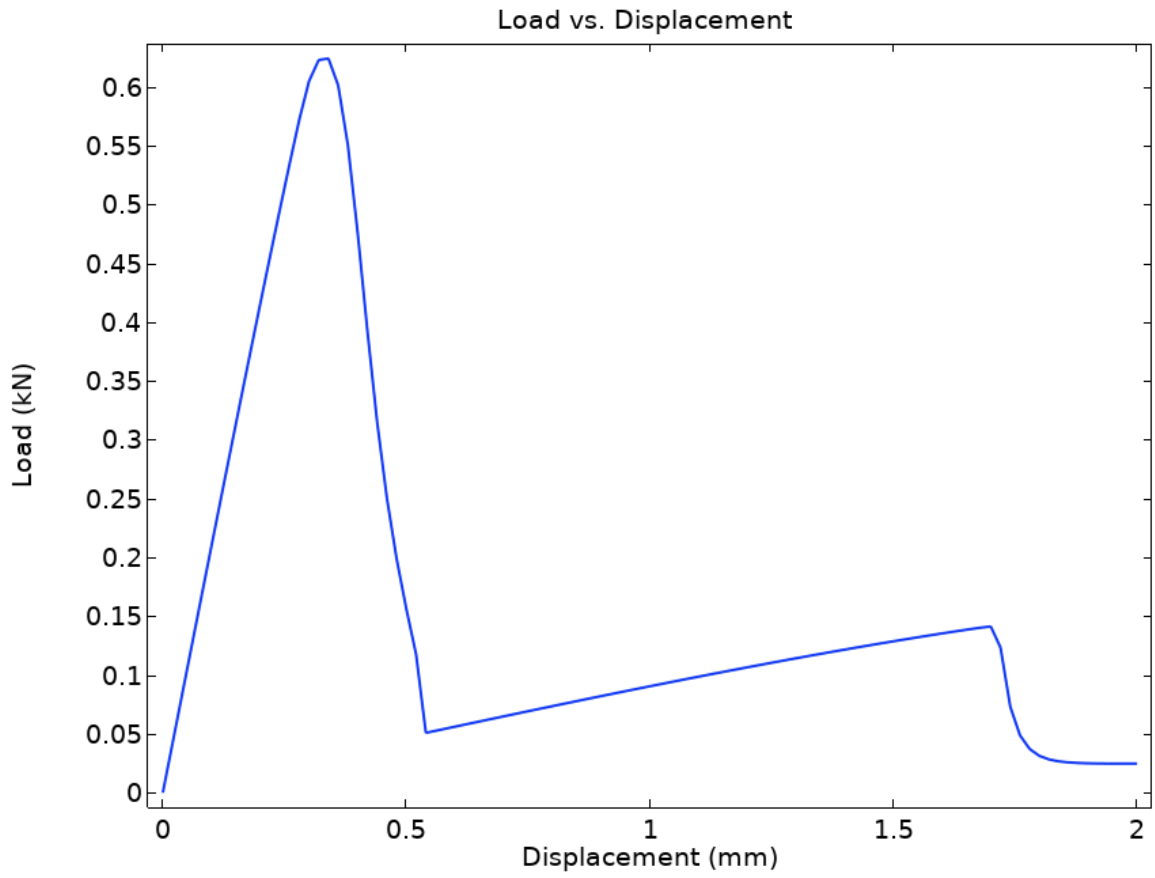


Figure 4-2. The load vs displacement of during the simulation of crack propagation.

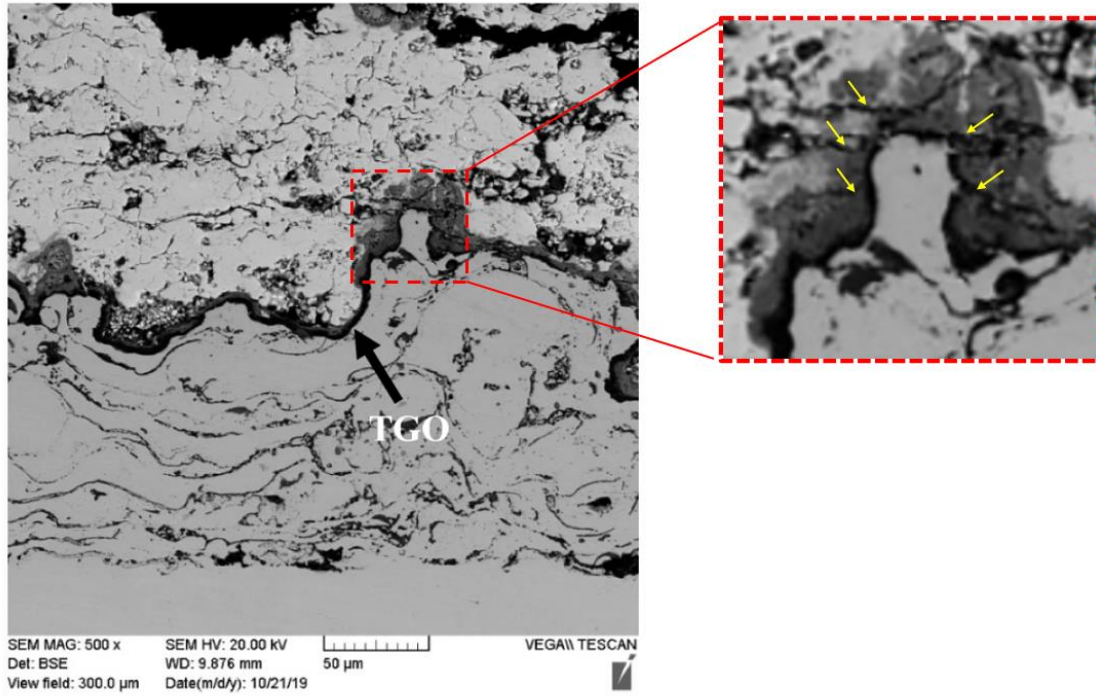


Figure 4-3. SEM image of oxidized APS-TBC specimen with denotes of microcracks near the interface [103]. (Copyright permission, Springer Nature)

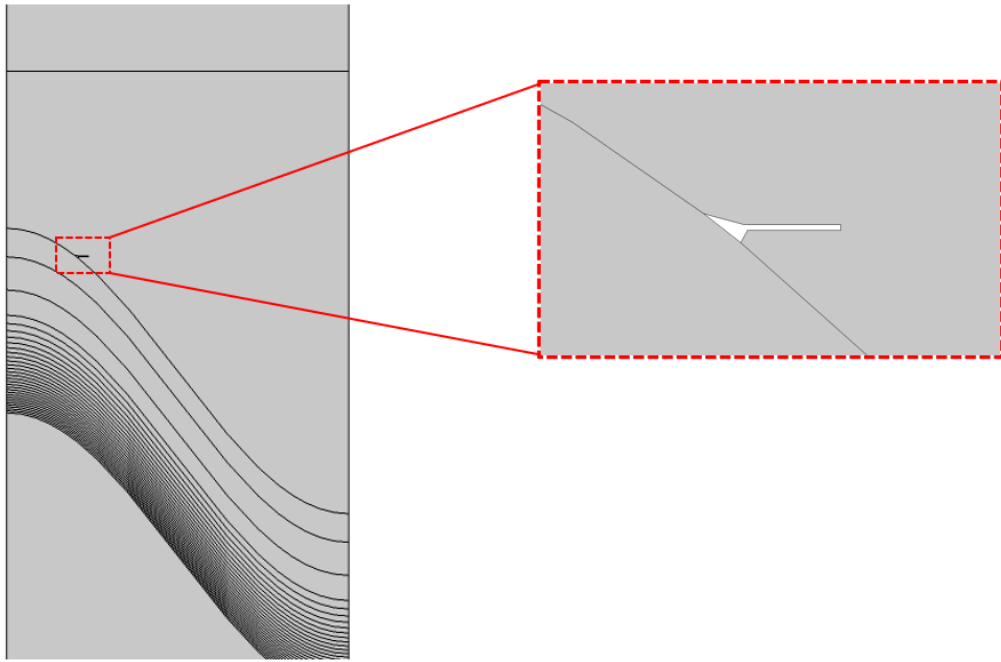


Figure 4-4. The geometry model used in the FEM analysis with implemented crack located at the off-peak of the roughness.

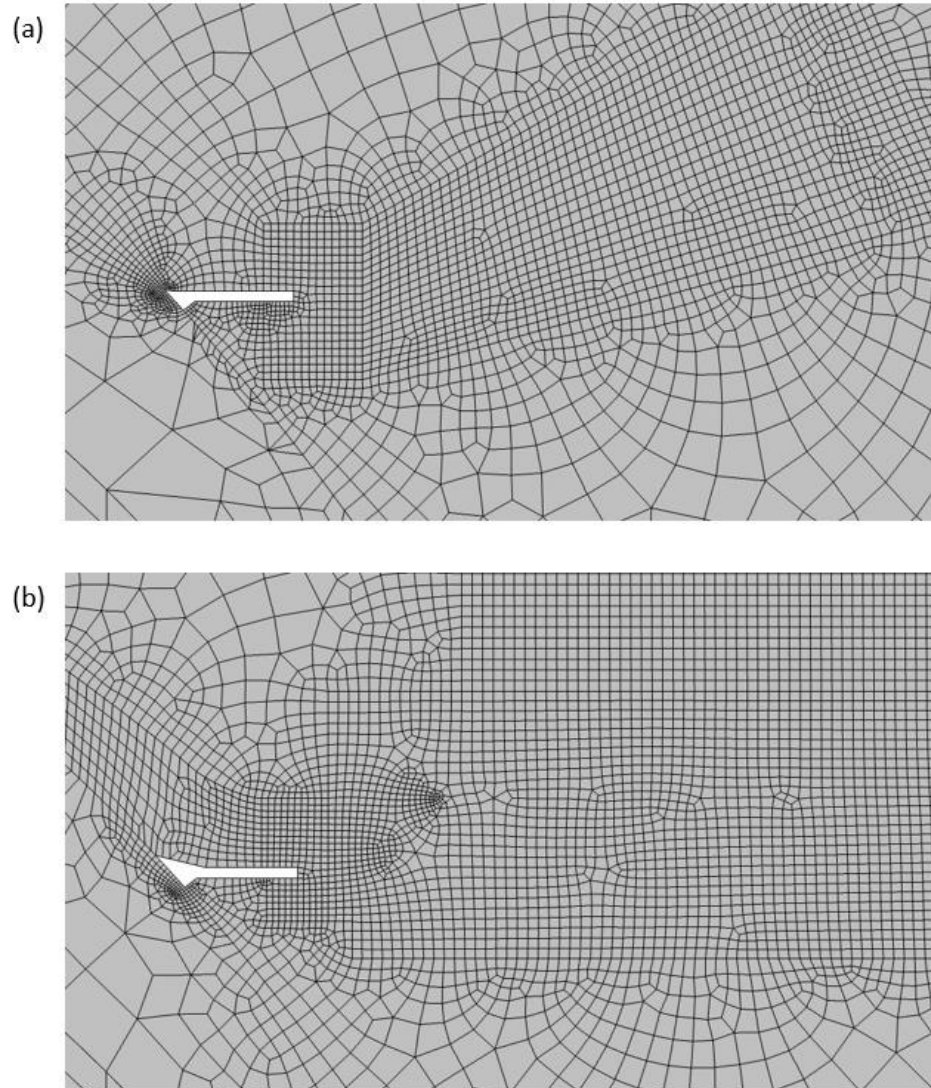


Figure 4-5. The mesh refinement near the crack with two orientations (a) follow the crack growth; (b) follows the initial crack direction. Both meshes have the maximum element size of $0.03\mu\text{m}$ at the crack propagation zone.

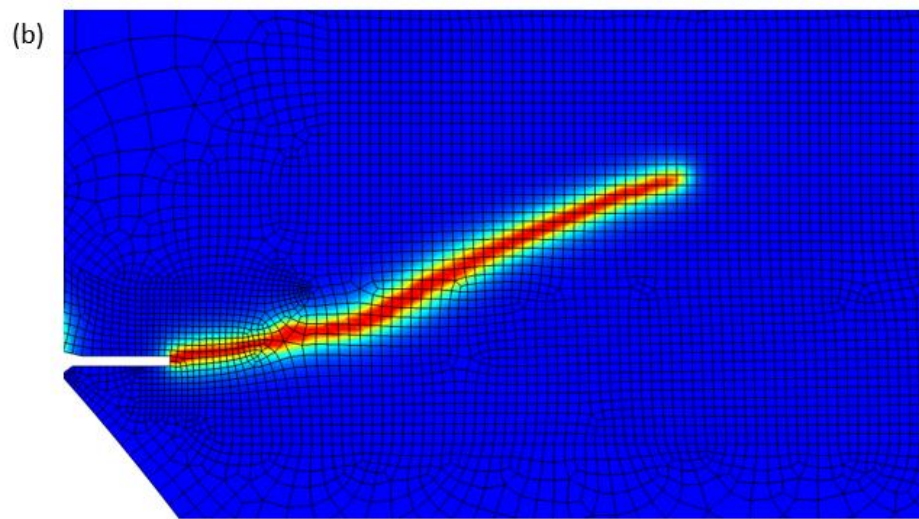
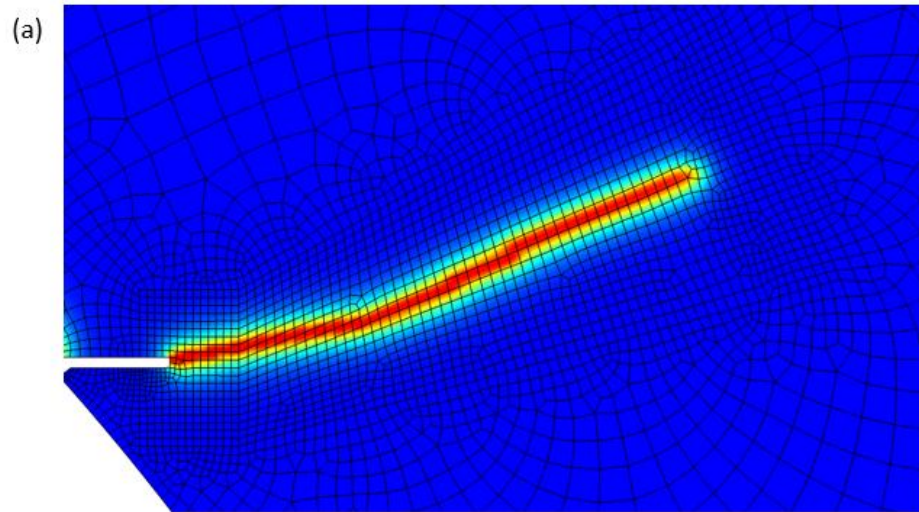


Figure 4-6. The phase field damage zone at 3600s (almost the end of cycle 1) for mesh (a) and (b)

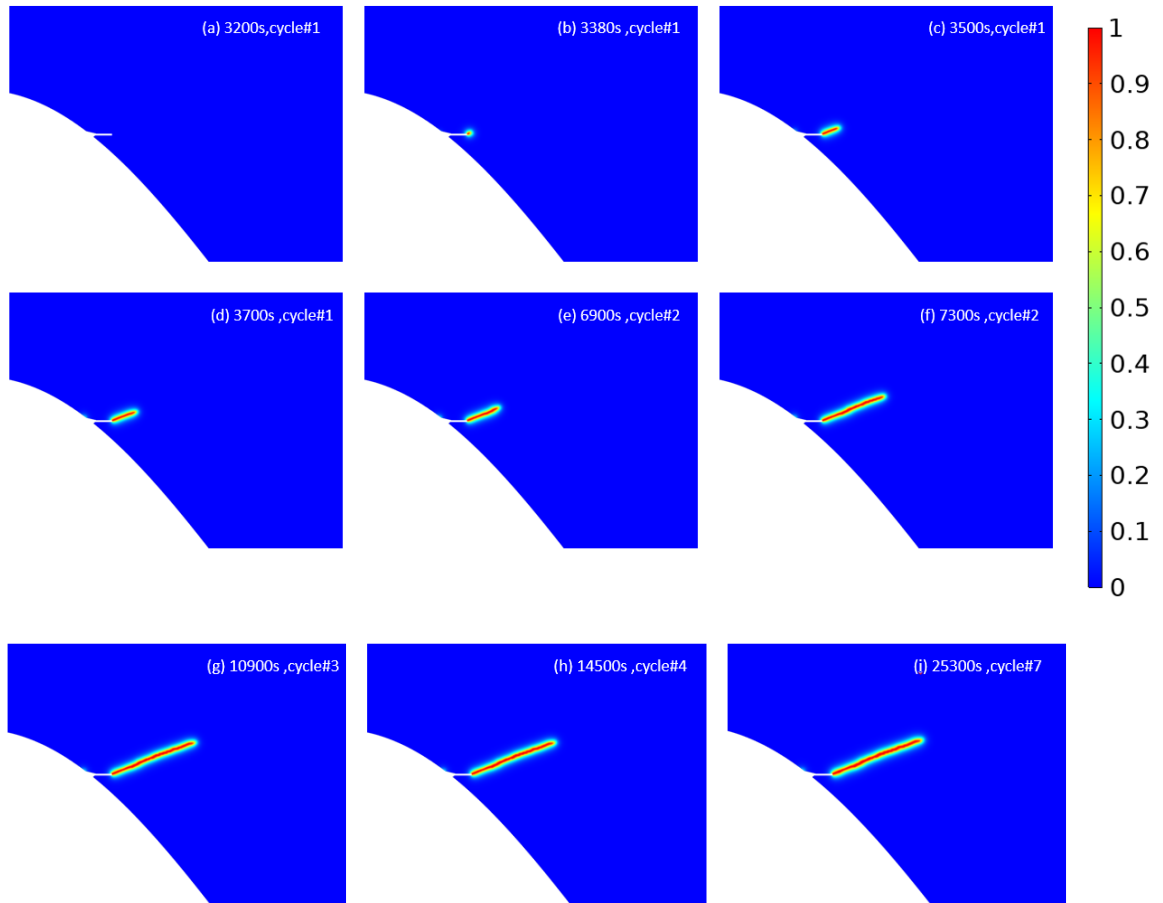


Figure 4-7. Surface plots of the crack phase field from cycle#1 with initial crack, to cycle#7 for reference case IX

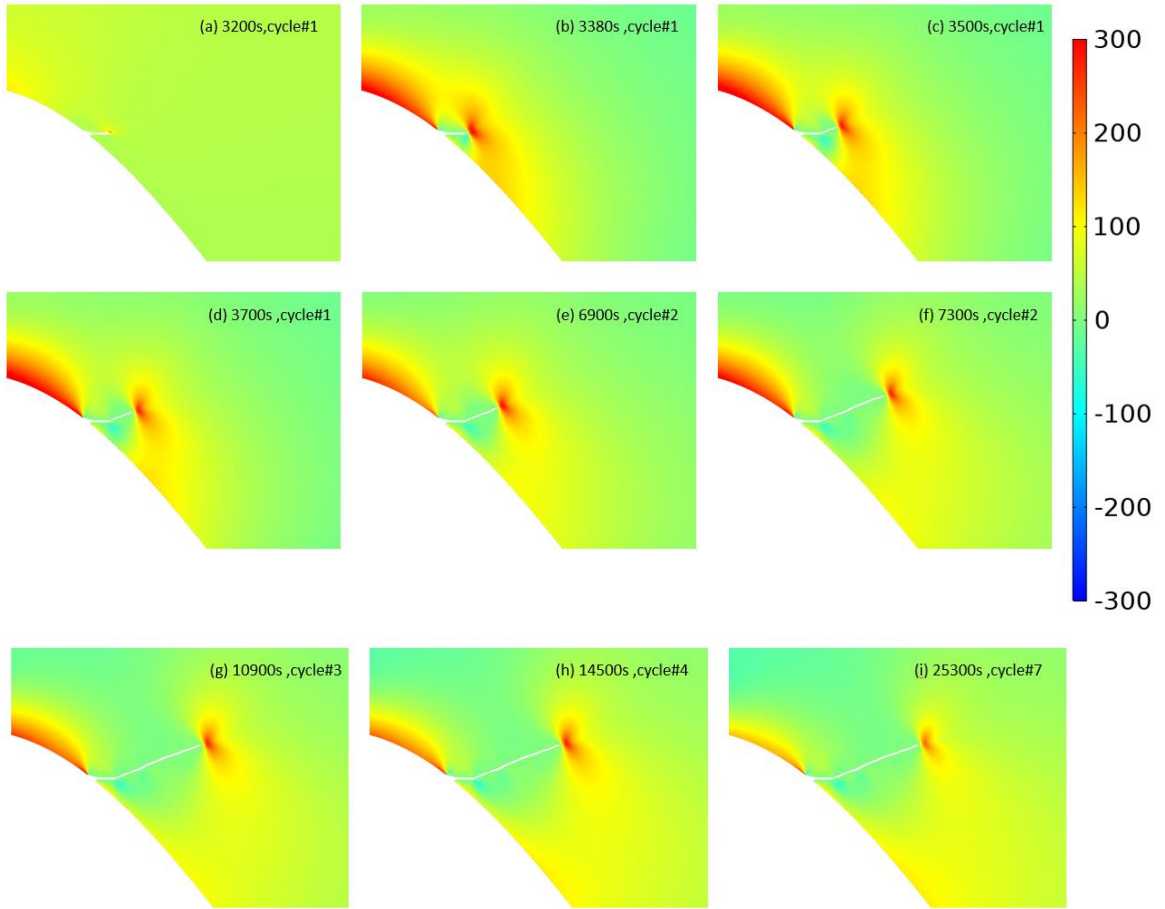


Figure 4-8. Surface plots of the damaged first principal stress distribution from cycle#1 with initial crack, to cycle#7 for reference case IX.

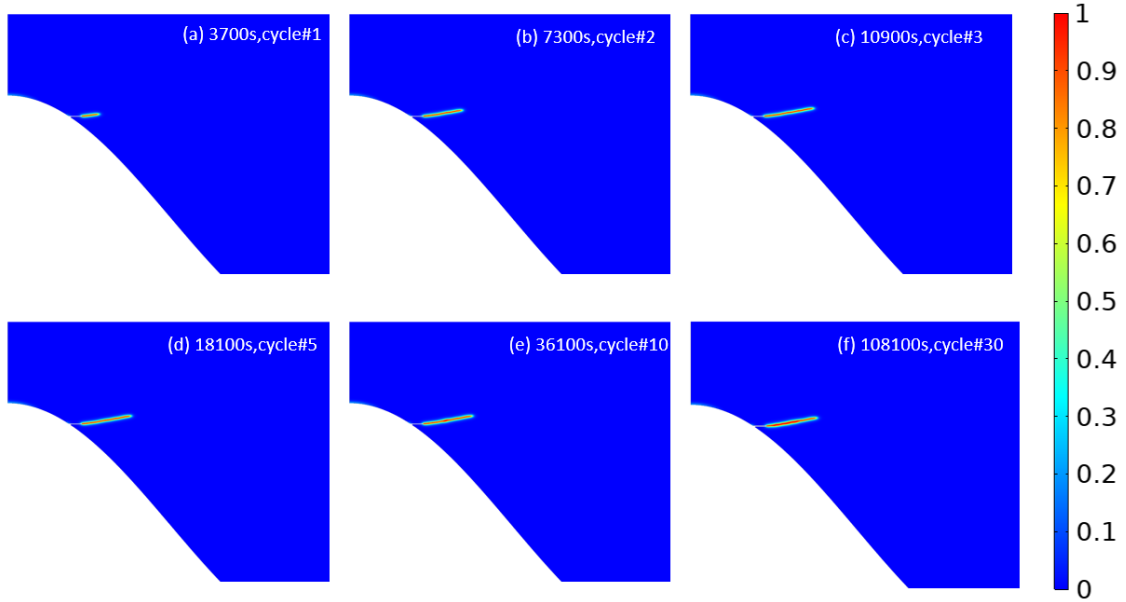


Figure 4-9. Surface plots of the crack phase field from cycle#1 to cycle#30 for case X with AR=15/24.

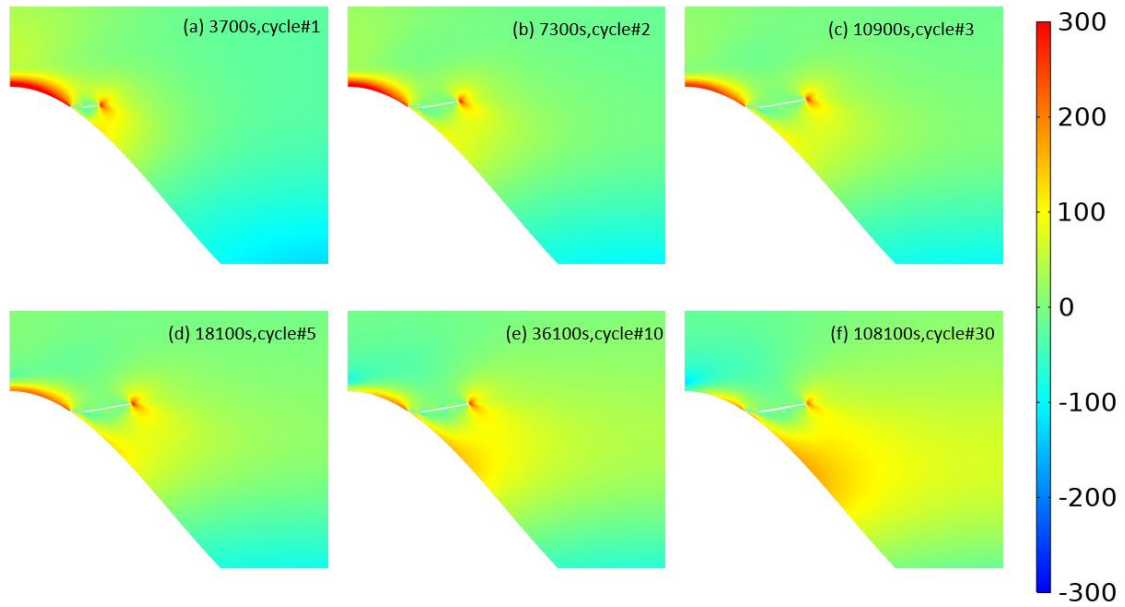


Figure 4-10. Surface plots of the damaged first principal stress distribution from cycle#1 to cycle#30 for case X with AR=15/24.

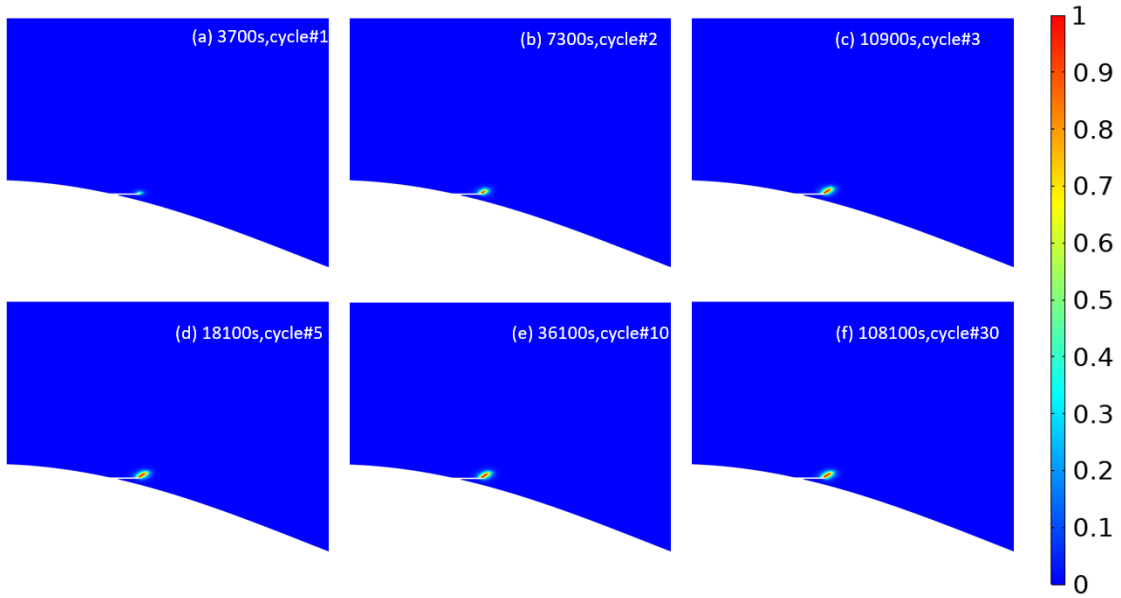


Figure 4-11. Surface plots of the crack phase field from cycle#1 to cycle#30 for case XI with $AR=5/24$.

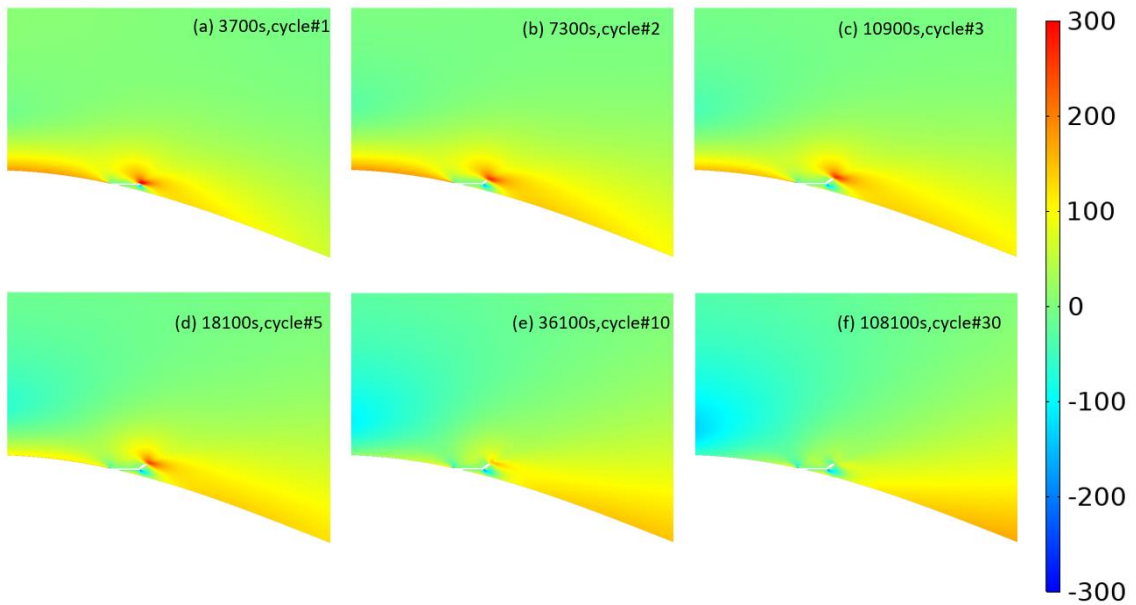


Figure 4-12. Surface plots of the damaged first principal stress distribution from cycle#1 to cycle#30 for case XI with $AR=5/24$.

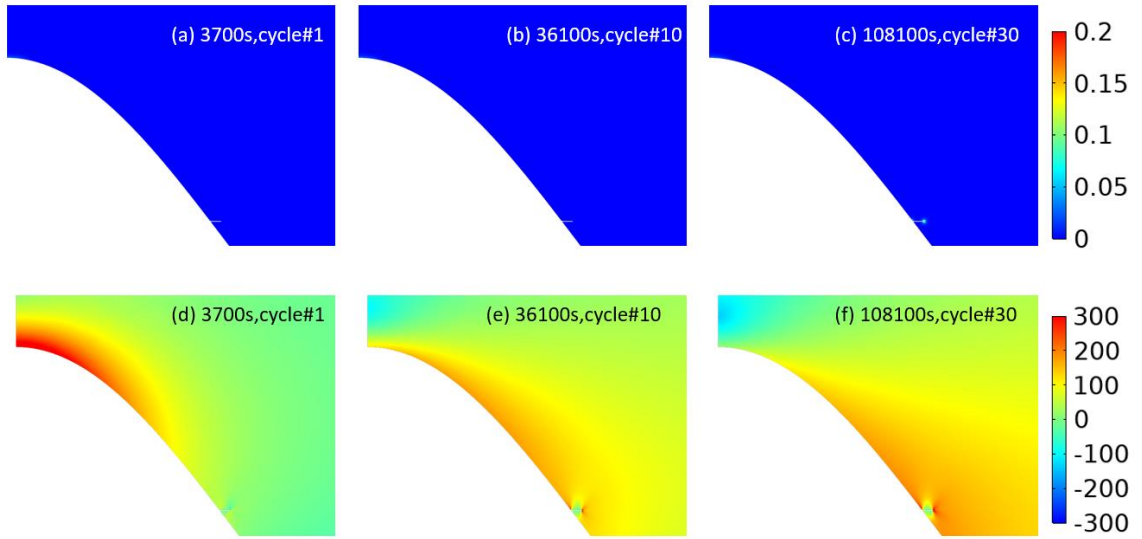


Figure 4-13. Surface plots of the crack phase field and the damaged first principal stress distribution from cycle#1 to cycle#30 for case XII with cracks at mid-level.

5. Conclusions and Future works

5.1. Conclusions

In this study, the FEM simulation of the TBC system is carefully built up with the consideration of TC sintering, BC oxidation, creep relaxation, heat transfer through the thickness, and multiple geometries at the interface between TC and TGO. The stress distribution and time evolution near the TC/TGO interface were studied and a crack was inserted into the TC to study the crack propagation via the phase field damage model.

In Chapter 3, the TBC system model is simulated at 1050°C for 30×1 hour thermal cycles to observe the stress distribution at TC and the time evolution. The case with reference geometry and material features indicates that the first principal stress is concentrated at the peak position at cycle# 1 and moves to the mid-level at cycle# 30. The stress level decreases as the TGO thickness increase, since the more rigid oxide shares the load. However, after the halfway of thermal cycles, the stress level increases again due to the densification of the material caused by sintering. The parametric studies investigate the effects with different TGO growth rate, roughness shape aspect ratio, TC sintering and conventional isothermal model. The results show that TGO thickness is the main factor affecting the stress concentration center. With higher aspect ratio, the stress center is less affected by the TGO thickness, but the stress level at the early cycles is increased due to the additional thermal mismatch. The sintering model does affect the stress level at the latter thermal cycles. At cycle#30, the stress level can increase about 25%. But it is unable to affect the stress center since that is controlled by the TGO thickness. The result gap between the thermal gradient and heat transfer model is very small, but it can be further investigated when the sintering model at TC can be affected

by the thermal gradient. With the stress distribution results, the risky region of crack propagation and the failure of the TC can be estimated, also the results can validate the phase field crack propagation results.

In Chapter 4, the phase field damage is implemented to simulate the crack propagation under different criterion. In the reference case, the crack near the off-peak position propagates at the early thermal cycles and stop propagating as the stress center moves to the valley. The stress distribution results match the results in Chapter 3, proves the feasibility using the phase field damage model to estimate the crack growth during the thermal cycles. The method can be further implemented in other geometry with different crack location, orientations, or number of cracks to estimate the crack propagation and life estimation.

5.2. Future work

In this research, there are several factors that have not be studied in the current research and expecting to improve in the future, including

- a) The TGO growth model can be replaced by the chemical control oxidation phase field model for better precision.
- b) The thermal gradient does not make effects on our results. If the sintering model can control its pace by the coating's depth could make difference.
- c) Tests should be performed to further validate the simulation results.
- d) The rising star phase field damage model needs further validation applied to our thermal load case. According to the literature, the phase field model is validated with the displacement load test case. For example: single-edge-notched plate tensile and shear test, Kathoff experiment, and so on.

- e) Further tuning of the damage parameter and solver configuration is necessary. During trial and error, the damaged mesh elements may collapse during the cool-down and cause unexpected local stress that branches the crack for no reason.

However, this Multiphysics model is still very powerful tool to study the crack propagation in TBC. More scenarios can be simulated with our model, like

- a) Multiple crack interactions.
- b) Different crack orientations.
- c) A more detail geometry extracted from the SEM images.

References:

- [1] N. P. Padture, M. Gell, and E. H. Jordan, “Thermal barrier coatings for gas-turbine engine applications,” *Science (1979)*, vol. 296, no. 5566, pp. 280–284, 2002, doi: 10.1126/science.1068609.
- [2] X. Q. Cao, R. Vassen, and D. Stoeber, “Ceramic materials for thermal barrier coatings,” *J Eur Ceram Soc*, vol. 24, no. 1, pp. 1–10, 2004, doi: 10.1016/S0955-2219(03)00129-8.
- [3] J.-C. Han, “Recent Studies in Turbine Blade Cooling,” *The International Journal of Rotating Machinery*, vol. 10, no. 6, pp. 443–457, 2004, doi: 10.1080/10236210490503978.
- [4] B. Gleeson, “Thermal barrier coatings for aeroengine applications,” *J Propuls Power*, vol. 22, no. 2, pp. 375–383, 2006, doi: 10.2514/1.20734.
- [5] D. R. Clarke and C. G. Levi, “Materials Design for the Next Generation Thermal Barrier Coatings,” *Annu Rev Mater Res*, vol. 33, no. 1, pp. 383–417, 2003, doi: 10.1146/annurev.matsci.33.011403.113718.
- [6] M. Bäker and P. Seiler, “A Guide to Finite Element Simulations of Thermal Barrier Coatings,” *Journal of Thermal Spray Technology*, vol. 26, no. 6, pp. 1146–1160, 2017, doi: 10.1007/s11666-017-0592-z.
- [7] J. R. Nicholls, “Advances in Coating Design for High-Performance Gas Turbines,” *MRS Bull*, vol. 28, no. 9, pp. 659–670, Sep. 2003, doi: 10.1557/mrs2003.194.

- [8] H. Xu and J. Wu, “New materials, technologies and processes in thermal barrier coatings,” in *Thermal Barrier Coatings*, Elsevier, 2011, pp. 317–328. doi: 10.1533/9780857090829.3.317.
- [9] M. Peters, C. Leyens, U. Schulz, and W. A. Kaysser, “EB-PVD thermal barrier coatings for aeroengines and gas turbines,” *Adv Eng Mater*, vol. 3, no. 4, pp. 193–204, 2001, doi: 10.1002/1527-2648(200104)3:4<193::AID-ADEM193>3.0.CO;2-U.
- [10] B. Bernard *et al.*, “Thermal insulation properties of YSZ coatings: Suspension Plasma Spraying (SPS) versus Electron Beam Physical Vapor Deposition (EB-PVD) and Atmospheric Plasma Spraying (APS),” *Surf Coat Technol*, vol. 318, pp. 122–128, 2017, doi: 10.1016/j.surfcoat.2016.06.010.
- [11] I. O. Golosnoy, A. Cipitria, and T. W. Clyne, “Heat transfer through plasma-sprayed thermal barrier coatings in gas turbines: A review of recent work,” *Journal of Thermal Spray Technology*, vol. 18, no. 5–6, pp. 809–821, Dec. 2009, doi: 10.1007/s11666-009-9337-y.
- [12] C. G. Levi, “Emerging materials and processes for thermal barrier systems,” *Curr Opin Solid State Mater Sci*, vol. 8, no. 1, pp. 77–91, 2004, doi: 10.1016/j.cossms.2004.03.009.
- [13] B. Lv, X. Fan, D. Li, and T. J. Wang, “Towards enhanced sintering resistance: Air-plasma-sprayed thermal barrier coating system with porosity gradient,” *J Eur Ceram Soc*, vol. 38, no. 4, pp. 1946–1956, Apr. 2018, doi: 10.1016/j.jeurceramsoc.2017.12.008.

- [14] T. Sadowski and P. Golewski, *Loadings in Thermal Barrier Coatings of Jet Engine Turbine Blades*, vol. 39, no. 2. Singapore: Springer Singapore, 2016. doi: 10.1007/978-981-10-0919-8.
- [15] E. Bakan and R. Vaßen, “Ceramic Top Coats of Plasma-Sprayed Thermal Barrier Coatings: Materials, Processes, and Properties,” *Journal of Thermal Spray Technology*, vol. 26, no. 6, pp. 992–1010, 2017, doi: 10.1007/s11666-017-0597-7.
- [16] M. Bäker, J. Rösler, and G. Heinze, “A parametric study of the stress state of thermal barrier coatings Part II: Cooling stresses,” *Acta Mater*, vol. 53, no. 2, pp. 469–476, 2005, doi: 10.1016/j.actamat.2004.10.004.
- [17] J. Song, H. Qi, S. Li, X. Yang, D. Shi, and C. Fei, “A diffusion-coupled cohesive element model for cracking analysis of thermal barrier coatings,” *Eng Fract Mech*, vol. 246, no. July 2020, p. 107625, 2021, doi: 10.1016/j.engfracmech.2021.107625.
- [18] F. Wu, E. H. Jordan, X. Ma, and M. Gell, “Thermally grown oxide growth behavior and spallation lives of solution precursor plasma spray thermal barrier coatings,” *Surf Coat Technol*, vol. 202, no. 9, pp. 1628–1635, 2008, doi: 10.1016/j.surfcoat.2007.07.055.
- [19] V. K. Tolpygo, D. R. Clarke, and K. S. Murphy, “Oxidation-induced failure of EB-PVD thermal barrier coatings,” *Surf Coat Technol*, vol. 146–147, pp. 124–131, 2001, doi: 10.1016/S0257-8972(01)01482-7.
- [20] H. Dong, G. J. Yang, C. X. Li, X. T. Luo, and C. J. Li, “Effect of TGO thickness on thermal cyclic lifetime and failure mode of plasma-sprayed TBC s,” *Journal of*

- the American Ceramic Society*, vol. 97, no. 4, pp. 1226–1232, 2014, doi: 10.1111/jace.12868.
- [21] M. S. Sahith, G. Giridhara, and R. S. Kumar, “Development and analysis of thermal barrier coatings on gas turbine blades - A Review,” *Mater Today Proc*, vol. 5, no. 1, pp. 2746–2751, 2018, doi: 10.1016/j.matpr.2018.01.060.
- [22] P. Fauchais, “Understanding plasma spraying,” *J Phys D Appl Phys*, vol. 37, no. 9, pp. R86–R108, May 2004, doi: 10.1088/0022-3727/37/9/R02.
- [23] R. G. Wellman and J. R. Nicholls, “Erosion, corrosion and erosion-corrosion of EB PVD thermal barrier coatings,” *Tribol Int*, vol. 41, no. 7, pp. 657–662, 2008, doi: 10.1016/j.triboint.2007.10.004.
- [24] X. Chen, “Calcium-magnesium-alumina-silicate (CMAS) delamination mechanisms in EB-PVD thermal barrier coatings,” *Surf Coat Technol*, vol. 200, no. 11, pp. 3418–3427, 2006, doi: 10.1016/j.surfcoat.2004.12.029.
- [25] B. S. Vasile, A. C. Birca, V. A. Surdu, I. A. Neacsu, and A. I. Nicoară, “Ceramic composite materials obtained by electron-beam physical vapor deposition used as thermal barriers in the aerospace industry,” *Nanomaterials*, vol. 10, no. 2, 2020, doi: 10.3390/nano10020370.
- [26] R. Vaßen, H. Kaßner, G. Mauer, and D. Stöver, “Suspension Plasma Spraying: Process Characteristics and Applications,” *Journal of Thermal Spray Technology*, vol. 19, no. 1–2, pp. 219–225, Jan. 2010, doi: 10.1007/s11666-009-9451-x.

- [27] B. Xiao, X. Huang, T. Robertson, Z. Tang, and R. Kearsey, "Sintering resistance of suspension plasma sprayed 7YSZ TBC under isothermal and cyclic oxidation," *J Eur Ceram Soc*, vol. 40, no. 5, pp. 2030–2041, 2020, doi: 10.1016/j.jeurceramsoc.2019.12.046.
- [28] B. Rajasekaran, G. Mauer, and R. Vaßen, "Enhanced characteristics of HVOF-sprayed MCrAlY bond coats for TBC applications," *Journal of Thermal Spray Technology*, vol. 20, no. 6, pp. 1209–1216, 2011, doi: 10.1007/s11666-011-9668-3.
- [29] J. Rösler, M. Bäker, and M. Volgmann, "Stress state and failure mechanisms of thermal barrier coatings: Role of creep in thermally grown oxide," *Acta Mater*, vol. 49, no. 18, pp. 3659–3670, 2001, doi: 10.1016/S1359-6454(01)00283-X.
- [30] R. Darolia, *Thermal barrier coatings technology: Critical review, progress update, remaining challenges and prospects*, vol. 58, no. 6. 2013. doi: 10.1179/1743280413Y.0000000019.
- [31] M. Ranjbar-Far, J. Absi, G. Mariaux, and F. Dubois, "Simulation of the effect of material properties and interface roughness on the stress distribution in thermal barrier coatings using finite element method," *Mater Des*, vol. 31, no. 2, pp. 772–781, 2010, doi: 10.1016/j.matdes.2009.08.005.
- [32] H. F. Chen *et al.*, "Recent progress in thermal/environmental barrier coatings and their corrosion resistance," *Rare Metals*, vol. 39, no. 5, pp. 498–512, 2020, doi: 10.1007/s12598-019-01307-1.

- [33] J. Aktaa, K. Sfar, and D. Munz, "Assessment of TBC systems failure mechanisms using a fracture mechanics approach," *Acta Mater*, vol. 53, no. 16, pp. 4399–4413, 2005, doi: 10.1016/j.actamat.2005.06.003.
- [34] D. R. Mumm and G. A. Evans, "Mechanisms controlling the performance and durability of thermal barrier coatings," *Key Eng Mater*, vol. 197, pp. 199–230, 2001, doi: 10.4028/www.scientific.net/kem.197.199.
- [35] R. A. Miller, "Thermal barrier coatings for aircraft engines: History and directions," *Journal of Thermal Spray Technology*, vol. 6, no. 1, pp. 35–42, 1997, doi: 10.1007/BF02646310.
- [36] A. Moteb and K. Chen, "Modelling and evaluating thermal conductivity of porous thermal barrier coatings at elevated temperatures," *Ceram Int*, vol. 46, no. 14, pp. 21939–21957, 2020, doi: 10.1016/j.ceramint.2020.04.228.
- [37] R. S. Ghai, K. Chen, and N. Baddour, "Modelling thermal conductivity of porous thermal barrier coatings," *Coatings*, vol. 9, no. 2, 2019, doi: 10.3390/COATINGS9020101.
- [38] B. C. Zhang, K. Chen, N. Baddour, and P. C. Patnaik, "Failure and life evaluation of EB-PVD thermal barrier coatings using temperature-process-dependent model parameters," *Corros Sci*, vol. 156, pp. 1–9, 2019, doi: 10.1016/j.corsci.2019.04.020.
- [39] B. Zhang, K. Chen, N. Baddour, and P. C. Patnaik, "Life Prediction of Atmospheric Plasma-Sprayed Thermal Barrier Coatings Using Temperature-

- Dependent Model Parameters,” *Journal of Thermal Spray Technology*, vol. 26, no. 5, pp. 902–912, Jun. 2017, doi: 10.1007/s11666-017-0558-1.
- [40] B. Cheng *et al.*, “Sintering-induced delamination of thermal barrier coatings by gradient thermal cyclic test,” *Journal of the American Ceramic Society*, vol. 100, no. 5, pp. 1820–1830, 2017, doi: 10.1111/jace.14713.
- [41] A. Cipitria, I. O. Golosnoy, and T. W. Clyne, “A sintering model for plasma-sprayed zirconia TBCs. Part I: Free-standing coatings,” *Acta Mater*, vol. 57, no. 4, pp. 980–992, 2009, doi: 10.1016/j.actamat.2008.10.024.
- [42] S. R. Choi, D. Zhu, and R. A. Miller, “Effect of sintering on mechanical properties of plasma-sprayed zirconia-based thermal barrier coatings,” *Journal of the American Ceramic Society*, vol. 88, no. 10, pp. 2859–2867, 2005, doi: 10.1111/j.1551-2916.2005.00504.x.
- [43] Y. H. Sohn, J. H. Kim, E. H. Jordan, and M. Gell, “Thermal cycling of EB-PVD/MCrAlY thermal barrier coatings: I. Microstructural development and spallation mechanisms,” *Surf Coat Technol*, vol. 146–147, pp. 70–78, 2001, doi: 10.1016/S0257-8972(01)01478-5.
- [44] A. Rabiei and A. G. Evans, “Failure mechanisms associated with the thermally grown oxide in plasma-sprayed thermal barrier coatings,” *Acta Mater*, vol. 48, no. 15, pp. 3963–3976, 2000, doi: 10.1016/S1359-6454(00)00171-3.
- [45] J. Rösler, M. Bäker, and K. Aufzug, “A parametric study of the stress state of thermal barrier coatings part I: Creep relaxation,” *Acta Mater*, vol. 52, no. 16, pp. 4809–4817, 2004, doi: 10.1016/j.actamat.2004.06.046.

- [46] S. Kyaw, A. Jones, and T. Hyde, "Predicting failure within TBC system: Finite element simulation of stress within TBC system as affected by sintering of APS TBC, geometry of substrate and creep of TGO," *Eng Fail Anal*, vol. 27, pp. 150–164, 2013, doi: 10.1016/j.engfailanal.2012.07.005.
- [47] B. Lv, H. Xie, R. Xu, X. Fan, W. Zhang, and T. J. Wang, "Effects of sintering and mixed oxide growth on the interface cracking of air-plasma-sprayed thermal barrier coating system at high temperature," *Appl Surf Sci*, vol. 360, pp. 461–469, 2016, doi: 10.1016/j.apsusc.2015.10.037.
- [48] A. Cipitria, I. O. Golosnoy, and T. W. Clyne, "Sintering kinetics of plasma-sprayed zirconia TBCs," *Journal of Thermal Spray Technology*, vol. 16, no. 5–6, pp. 809–815, 2007, doi: 10.1007/s11666-007-9080-1.
- [49] A. Cipitria, I. O. Golosnoy, and T. W. Clyne, "A sintering model for plasma-sprayed zirconia thermal barrier coatings. Part II: Coatings bonded to a rigid substrate," *Acta Mater*, vol. 57, no. 4, pp. 993–1003, 2009, doi: 10.1016/j.actamat.2008.10.058.
- [50] R. G. Hutchinson, N. A. Fleck, and A. C. F. Cocks, "A sintering model for thermal barrier coatings," *Acta Mater*, vol. 54, no. 5, pp. 1297–1306, 2006, doi: 10.1016/j.actamat.2005.10.056.
- [51] S. Kumar and A. C. F. Cocks, "Sintering and mud cracking in EB-PVD thermal barrier coatings," *J Mech Phys Solids*, vol. 60, no. 4, pp. 723–749, 2012, doi: 10.1016/j.jmps.2011.12.004.

- [52] S. Kumar and A. C. F. Cocks, “Computational modelling of constrained sintering in EB-PVD thermal barrier coatings,” *Model Simul Mat Sci Eng*, vol. 21, no. 6, 2013, doi: 10.1088/0965-0393/21/6/065008.
- [53] A. C. F. Cocks and N. A. Fleck, “Constrained sintering of an air-plasma-sprayed thermal barrier coating,” *Acta Mater*, vol. 58, no. 12, pp. 4233–4244, 2010, doi: 10.1016/j.actamat.2010.04.015.
- [54] B. Lv *et al.*, “A constitutive model for the sintering of suspension plasma-sprayed thermal barrier coating with vertical cracks,” *Journal of the American Ceramic Society*, vol. 102, no. 10, pp. 6202–6212, 2019, doi: 10.1111/jace.16491.
- [55] M. Gasik and B. Zhang, “A constitutive model and FE simulation for the sintering process of powder compacts,” *Comput Mater Sci*, vol. 18, no. 1, pp. 93–101, 2000, doi: 10.1016/s0927-0256(00)00090-2.
- [56] A. Cocks, N. Fleck, and S. Lampenscherf, “A brick model for asperity sintering and creep of APS TBCs,” *J Mech Phys Solids*, vol. 63, no. 1, pp. 412–431, 2014, doi: 10.1016/j.jmps.2013.08.016.
- [57] H. Y. Qi and X. G. Yang, “Life prediction of thermal barrier coatings,” in *Thermal Barrier Coatings*, Elsevier, 2011, pp. 294–316. doi: 10.1533/9780857090829.3.294.
- [58] E. P. Busso, J. Lin, S. Sakurai, and M. Nakayama, “A mechanistic study of oxidation-induced degradation in a plasma-sprayed thermal barrier coating system. Part I: Model formulation,” *Acta Mater*, vol. 49, no. 9, pp. 1515–1528, 2001, doi: 10.1016/S1359-6454(01)00060-X.

- [59] F. Sait, E. Gurses, and O. Aslan, “Modeling and simulation of coupled phase transformation and stress evolution in thermal barrier coatings,” *Int J Plast*, vol. 134, no. May, p. 102790, 2020, doi: 10.1016/j.ijplas.2020.102790.
- [60] Q. Q. Zhou, L. Yang, C. Luo, F. W. Chen, Y. C. Zhou, and Y. G. Wei, “Thermal barrier coatings failure mechanism during the interfacial oxidation process under the interaction between interface by cohesive zone model and brittle fracture by phase-field,” *Int J Solids Struct*, vol. 214–215, pp. 18–34, 2021, doi: 10.1016/j.ijsolstr.2020.12.020.
- [61] D. Pan, M. W. Chen, P. K. Wright, and K. J. Hemker, “Evolution of a diffusion aluminide bond coat for thermal barrier coatings during thermal cycling,” *Acta Mater*, vol. 51, no. 8, pp. 2205–2217, 2003, doi: 10.1016/S1359-6454(03)00014-4.
- [62] A. Abdelgawad and K. Al-Athel, “Effect of TGO thickness, pores, and creep on the developed residual stresses in thermal barrier coatings under cyclic loading using SEM image-based finite element model,” *Ceram Int*, vol. 47, no. 14, pp. 20064–20076, 2021, doi: 10.1016/j.ceramint.2021.03.336.
- [63] J. Jiang, W. Wang, X. Zhao, Y. Liu, Z. Cao, and P. Xiao, “Numerical analyses of the residual stress and top coat cracking behavior in thermal barrier coatings under cyclic thermal loading,” *Eng Fract Mech*, vol. 196, no. September 2017, pp. 191–205, 2018, doi: 10.1016/j.engfracmech.2018.04.031.
- [64] M. Bialas, “Finite element analysis of stress distribution in thermal barrier coatings,” *Surf Coat Technol*, vol. 202, no. 24, pp. 6002–6010, 2008, doi: 10.1016/j.surfcoat.2008.06.178.

- [65] COMSOL, *Structural Mechanics Module User's Guide Version 5.6*. 2020.
- [66] J. G. Thakare, C. Pandey, M. M. Mahapatra, and R. S. Mulik, "Thermal Barrier Coatings—A State of the Art Review," *Metals and Materials International*, vol. 27, no. 7, pp. 1947–1968, 2021, doi: 10.1007/s12540-020-00705-w.
- [67] A. M. Freborg, B. L. Ferguson, W. J. Brindley, and G. J. Petrus, "Modeling oxidation induced stresses in thermal barrier coatings," *Materials Science and Engineering A*, vol. 245, no. 2, pp. 182–190, 1998, doi: 10.1016/S0921-5093(97)00849-6.
- [68] J. Song, S. Li, X. Yang, H. Qi, and D. Shi, "Numerical investigation on the cracking behaviors of thermal barrier coating system under different thermal cycle loading waveforms," *Surf Coat Technol*, vol. 349, no. May, pp. 166–176, 2018, doi: 10.1016/j.surfcoat.2018.05.049.
- [69] G. J. Petrus and B. L. Ferguson, "A software tool to design thermal barrier coatings: A technical note," *Journal of Thermal Spray Technology*, vol. 6, no. 1, pp. 29–34, 1997, doi: 10.1007/BF02646309.
- [70] S. T. Kyaw, I. A. Jones, and T. H. Hyde, "Simulation of failure of air plasma sprayed thermal barrier coating due to interfacial and bulk cracks using surface-based cohesive interaction and extended finite element method," *Journal of Strain Analysis for Engineering Design*, vol. 51, no. 2, pp. 132–143, 2016, doi: 10.1177/0309324715615746.
- [71] M. Gupta, K. Skogsberg, and P. Nylén, "Influence of topcoat-bondcoat interface roughness on stresses and lifetime in thermal barrier coatings," *Journal of Thermal*

- Spray Technology*, vol. 23, no. 1–2, pp. 170–181, 2014, doi: 10.1007/s11666-013-0022-9.
- [72] L. Wang *et al.*, “Modeling of thermal properties and failure of thermal barrier coatings with the use of finite element methods: A review,” *J Eur Ceram Soc*, vol. 36, no. 6, pp. 1313–1331, 2016, doi: 10.1016/j.jeurceramsoc.2015.12.038.
- [73] X. Fan, R. Xu, and T. J. Wang, “Interfacial delamination of double-ceramic-layer thermal barrier coating system,” *Ceram Int*, vol. 40, no. 9 PART A, pp. 13793–13802, 2014, doi: 10.1016/j.ceramint.2014.05.095.
- [74] K. Al-Athel, K. Loeffel, H. Liu, and L. Anand, “Modeling decohesion of a top-coat from a thermally-growing oxide in a thermal barrier coating,” *Surf Coat Technol*, vol. 222, pp. 68–78, 2013, doi: 10.1016/j.surfcoat.2013.02.005.
- [75] A. Jafari, P. Broumand, M. Vahab, and N. Khalili, “An eXtended Finite Element Method implementation in COMSOL Multiphysics: Solid Mechanics,” *Finite Elements in Analysis and Design*, vol. 202, no. July 2021, p. 103707, 2022, doi: 10.1016/j.finel.2021.103707.
- [76] S. Zhou, X. Zhuang, and T. Rabczuk, “A phase-field modeling approach of fracture propagation in poroelastic media,” *Eng Geol*, vol. 240, pp. 189–203, 2018, doi: 10.1016/j.enggeo.2018.04.008.
- [77] C. Miehe, M. Hofacker, and F. Welschinger, “A phase field model for rate-independent crack propagation: Robust algorithmic implementation based on operator splits,” *Comput Methods Appl Mech Eng*, vol. 199, no. 45–48, pp. 2765–2778, 2010, doi: 10.1016/j.cma.2010.04.011.

- [78] S. Zhou, T. Rabczuk, and X. Zhuang, “Phase field modeling of quasi-static and dynamic crack propagation: COMSOL implementation and case studies,” *Advances in Engineering Software*, vol. 122, no. March, pp. 31–49, 2018, doi: 10.1016/j.advengsoft.2018.03.012.
- [79] C. Miehe, L. M. Schänzel, and H. Ulmer, “Phase field modeling of fracture in multi-physics problems. Part I. Balance of crack surface and failure criteria for brittle crack propagation in thermo-elastic solids,” *Comput Methods Appl Mech Eng*, vol. 294, pp. 449–485, 2015, doi: 10.1016/j.cma.2014.11.016.
- [80] X. Zhang, A. C. F. Cocks, Y. Okajima, K. Takeno, and T. Torigoe, “An image-based model for the sintering of air plasma sprayed thermal barrier coatings,” *Acta Mater*, vol. 206, p. 116649, 2021, doi: 10.1016/j.actamat.2021.116649.
- [81] P. Fauchais, M. Vardelle, and A. Vardelle, “Reliability of plasma-sprayed coatings: Monitoring the plasma spray process and improving the quality of coatings,” *J Phys D Appl Phys*, vol. 46, no. 22, 2013, doi: 10.1088/0022-3727/46/22/224016.
- [82] N. Ali *et al.*, “Deposition of stainless steel thin films: An electron beam physical vapour deposition approach,” *Materials*, vol. 12, no. 4, pp. 1–16, 2019, doi: 10.3390/ma12040571.
- [83] S. Mahade *et al.*, “Understanding the effect of material composition and microstructural design on the erosion behavior of plasma sprayed thermal barrier coatings,” *Appl Surf Sci*, vol. 488, pp. 170–184, 2019, doi: 10.1016/j.apsusc.2019.05.245.

- [84] H. Samadi and T. W. Coyle, “Modeling the build-up of internal stresses in multilayer thick thermal barrier coatings,” *Journal of Thermal Spray Technology*, vol. 18, no. 5–6, pp. 996–1003, 2009, doi: 10.1007/s11666-009-9396-0.
- [85] M. Shinozaki and T. W. Clyne, “A methodology, based on sintering-induced stiffening, for prediction of the spallation lifetime of plasma-sprayed coatings,” *Acta Mater*, vol. 61, no. 2, pp. 579–588, 2013, doi: 10.1016/j.actamat.2012.09.079.
- [86] F. J. Cunha, “Heat Transfer Analysis - Introduction,” *The Gas Turbine Handbook*, no. 860, 2006.
- [87] COMSOL, *Heat Transfer Module User’s Guide Version 5.6*. 2020.
- [88] Z. Wang, P. T. Ireland, S. T. Kohler, and J. W. Chew, “Heat transfer measurements to a gas turbine cooling passage with inclined ribs,” *ASME 1996 International Gas Turbine and Aeroengine Congress and Exhibition, GT 1996*, vol. 4, no. January, 1996, doi: 10.1115/96-GT-542.
- [89] Meherwan P. Boyce, *Gas Turbine Engineering Handbook*. Elsevier, 2012. doi: 10.1016/C2009-0-64242-2.
- [90] F. Irgens, *Continuum Mechanics*, 1st ed. Berlin: Springer, 2008.
- [91] M. Caliez, J. L. Chaboche, F. Feyel, and S. Kruch, “Numerical simulation of EBPVD thermal barrier coatings spallation,” *Acta Mater*, vol. 51, no. 4, pp. 1133–1141, 2003, doi: 10.1016/S1359-6454(02)00518-9.
- [92] R. Vaßen, F. Traeger, and D. Stöver, “Correlation between spraying conditions and microcrack density and their influence on thermal cycling life of thermal

- barrier coatings,” *Journal of Thermal Spray Technology*, vol. 13, no. 3, pp. 396–404, 2004, doi: 10.1361/10599630420443.
- [93] E. James, F. Shackelford, and W. Alexander, *Materials Science and Engineering Handbook*. 2001.
- [94] R. BRANDT, L. PAWLOWSKI, G. NEUER, and P. FAUCHAIS, “Specific heat and thermal conductivity of plasma sprayed yttria-stabilized zirconia and NiAl, NiCr, NiCrAl, NiCrAlY, NiCoCrAlY coatings,” *High Temperatures. High Pressures (Print)*, vol. 18, no. 1, pp. 65–77, 1986.
- [95] J. B. Wahl and K. Harris, “Improved 3 rd Generation Single Crystal Superalloy CMSX-4® Plus (SLS)-a study of evolutionary alloy development,” *Note*, no. Table I, 1984, [Online]. Available: <https://cannonmuskegon.com/wp-content/uploads/2018/08/Improved-3rd-Generation-Single-Crystal-Superalloy-CMSX-4®-Plus-SLS.pdf>
- [96] C. Borri, A. Lavacchi, A. Fossati, I. Perissi, and U. Bardi, “Finite Element Analysis of Thermal Fatigue in Thermal Barrier Coatings (TBC),” *Uk.Comsol.Com*, 2009, [Online]. Available: <https://www.uk.comsol.com/papers/6570/download/Borri.pdf>
<https://www.comsol.it/paper/download/44874/Borri.pdf>
- [97] L. Hu, C. A. Wang, Z. Hu, S. Lu, C. Sun, and Y. Huang, “Porous yttria-stabilized zirconia ceramics with ultra-low thermal conductivity. Part II: Temperature dependence of thermophysical properties,” *J Mater Sci*, vol. 46, no. 3, pp. 623–628, 2011, doi: 10.1007/s10853-010-4783-y.

- [98] Matweb, “MatWeb Material Property Data,” *Matweb LLC*.
<https://www.matweb.com/services/services.aspx> (accessed Jun. 03, 2022).
- [99] M. Z. Zhu and S. Gu, “Study of Volcanic Ash Impact onto Turbine Blades in Jet Engines,” 2017. [Online]. Available:
<https://openresearch.surrey.ac.uk/esploro/outputs/doctoral/Study-of-volcanic-ash-impact-onto-turbine-blades-in-jet-engines/99516847702346>
- [100] M. Ambati, T. Gerasimov, and L. de Lorenzis, “A review on phase-field models of brittle fracture and a new fast hybrid formulation,” *Comput Mech*, vol. 55, no. 2, pp. 383–405, 2015, doi: 10.1007/s00466-014-1109-y.
- [101] J. Y. Wu and Y. Huang, “Comprehensive implementations of phase-field damage models in Abaqus,” *Theoretical and Applied Fracture Mechanics*, vol. 106, no. December 2019, p. 102440, 2020, doi: 10.1016/j.tafmec.2019.102440.
- [102] J. M. Sargado, E. Keilegavlen, I. Berre, and J. M. Nordbotten, “A combined finite element–finite volume framework for phase-field fracture,” *Comput Methods Appl Mech Eng*, vol. 373, p. 113474, 2021, doi: 10.1016/j.cma.2020.113474.
- [103] S. K. Essa, K. Chen, R. Liu, X. Wu, and M. X. Yao, “Failure Mechanisms of APS-YSZ-CoNiCrAlY Thermal Barrier Coating Under Isothermal Oxidation and Solid Particle Erosion,” *Journal of Thermal Spray Technology*, vol. 30, no. 1–2, pp. 424–441, 2021, doi: 10.1007/s11666-020-01124-4.